



universität  
wien

# DISSERTATION

## Quantitative functional optical imaging of the human skin using multi-spectral imaging

angestrebter akademischer Grad

Doktor der Naturwissenschaften (Dr. rer.nat.)

Verfasserin / Verfasser: Mag. Jana M. Kainerstorfer  
Matrikel-Nummer: 0205595  
Dissertationsgebiet (lt. Studienblatt): A 091 411 Dr.-Studium der Naturwissenschaften Physik  
Betreuerin / Betreuer: Ao. Prof. Dr. Christoph K. Hitztenberger

Wien, am 07. Oktober 2010

*The secret of life is to fall seven times  
and to get up eight times.*

*The Alchemist  
Paulo Coelho*

*for my family*

The work presented in this thesis has been conducted at the National Institutes of Health, Bethesda, MD, USA as part of the Individual Graduate Partnership Program. The work was supervised by Amir Gandjbakhche at the Section on Analytical and Functional Biophotonics / Program on Pediatric Imaging and Tissue Sciences at the *Eunice Kennedy Shriver* National Institute of Child Health and Human Development.

## Abstract

Light tissue interactions can be described by the physical principles of absorption and scattering. Based on those parameters, different tissue types and analytes can be distinguished. Extracting blood volume and oxygenation is of particular interest in clinical routines for tumor diagnostics and treatment follow up, since they are parameters of angiogenic processes. The quantification of those analytes in tissue can be done by physical modeling of light tissue interaction. The physical model used here is the random walk theory.

However, for quantification and clinical usefulness, one has to account for multiple challenges. First, one must consider the effect of topology of the sample on measured physical parameters. Second, diffusion of light inside the tissue is dependent on the structure of the sample imaged. Thus, the structural conformation has to be taken into account. Third, clinical translation of imaging modalities is often hindered due to the complicated post-processing of data, not providing results in real-time.

In this thesis, two imaging modalities are being utilized, where the first one, diffuse multi-spectral imaging, is based on absorption contrast and spectral characteristics and the second one, Optical Coherence Tomography (OCT), is based on scattering changes within the tissue. Multi-spectral imaging can provide spatial distributions of blood volume and blood oxygenation and OCT yields 3D structural images with micrometer resolution.

In order to address the challenges mentioned above, a curvature correction algorithm for taking the topology into account was developed. Without taking curvature of the object into account, reconstruction of optical properties is not accurate. The method developed removes this artifact and recovers the underlying data, without the necessity of measuring the object's shape. The next step was to recover blood volume and oxygenation values in real time. Principal Component Analysis (PCA) on multi spectral images is introduced and it is shown that PCA can extract those parameters in real time, at least qualitatively. In order to convert those qualitative results into quantitative ones, the anatomical structures need to be accounted for. It is shown, in simulation and in vivo data, that blood volume can reliably be reconstructed, regardless of the underlying structure, whereas blood oxygenation is highly dependent on it. For in vivo validation, OCT was used for measuring the epidermal thickness, which was used as prior information for the PCA based reconstruction, using multi spectral data, and quantification of blood volume and oxygenation was achieved in real time.

The work described in this thesis led to four journal articles. Those articles build the cornerstone of the thesis and are reproduced in chapters 4, 6, 8, and 9.

## Kurzfassung

Wechselwirkungen zwischen Licht und Gewebe können mittels Absorption und Streuung beschrieben werden. Basierend auf diesen Parametern können verschiedene Gewebetypen und Analyte unterschieden werden. Besonders interessante Parameter für klinische Untersuchungen von Tumoren sind Blutvolumen und Sauerstoffgehalt im Blut, da sie bei der Angiogenese eine wichtige Rolle spielen. Eine Quantifizierung dieser Parameter kann mit physikalischen Modellen erreicht werden, die Licht – Haut Wechselwirkungen beschreiben. Das in dieser Arbeit verwendete Modell basiert auf der random walk Theorie.

Um quantitative Ergebnisse sowie eine klinische Umsetzung zu erreichen, müssen jedoch etliche Hürden überwunden werden. Erstens muss die Topologie des Objektes berücksichtigt werden, sowie deren Einfluss auf die Rekonstruktion physikalischer Parameter. Zweitens muss beachtet werden, dass die Diffusion von Licht im Objekt von dessen Struktur abhängt, weshalb die anatomische Struktur des Objekts bekannt sein muss. Drittens ist es für eine klinische Anwendung entscheidend, die Resultate in Echtzeit zu ermitteln.

Für die vorliegende Arbeit werden zwei bildgebende Verfahren verwendet: multi-spektrales Imaging und optische Kohärenztomografie (optical coherence tomography, OCT). Der Kontrast beim multi-spektralen Imaging basiert auf Absorption, der Kontrast bei der OCT auf Streuung von Licht. Blutvolumen und Sauerstoffgehalt können mit multi-spektralen Daten ermittelt werden; OCT liefert strukturelle Information mit Mikrometer-Auflösung.

Um die oben genannten Hürden zu überwinden, wurde ein Krümmungskorrektur-Algorithmus entwickelt, der die Topologie des Objektes extrahiert. Ohne diesen Schritt ist die Rekonstruktion der optischen Objekteigenschaften ungenau. Im nächsten Schritt wird die Principal Component Analysis (PCA) zur Bestimmung von Blutvolumen und Sauerstoffgehalt verwendet. Es wird gezeigt, dass PCA Blutvolumen und Sauerstoffgehalt zumindest qualitativ extrahieren kann. Weiters wird anhand von Simulationen und in vivo Daten gezeigt, dass quantitative Resultate mit PCA erzielt werden können, wenn die Struktur des Objekts bekannt ist. Für in vivo Messungen in der Haut wurde zunächst die Epidermisdicke mittels OCT Messung bestimmt; die gemessenen Werte wurden dann bei der PCA berücksichtigt. Mit dieser Kombination konnten Blutvolumen und Sauerstoffgehalt quantitativ in Echtzeit bestimmt werden.

Diese Arbeit hat zu vier Publikationen in wissenschaftlichen Fachzeitschriften geführt, die die Eckpfeiler dieser Dissertation bilden (siehe Kapitel 4, 6, 8 und 9).

# Contents

<b>INTRODUCTION .....</b>	<b>11</b>
1.1 Rationale .....	11
1.2 Medical Imaging <i>in vivo</i> .....	11
1.2.1 Non-optical techniques .....	11
1.2.2 Optical skin imaging.....	13
1.3 Research Objectives.....	17
1.4 Thesis outline.....	19
<b>BASICS AND PRINCIPLES .....</b>	<b>21</b>
2.1 Optical properties.....	21
2.1.1 Refractive index.....	21
2.1.2 Absorption .....	22
2.1.3 Scatter .....	23
2.1.4 Anisotropy .....	24
2.2 The human skin – structure and optical properties.....	27
2.2.1 Skin function and structure.....	27
2.2.2 Hemoglobin absorption.....	28
2.2.3 Melanin absorption .....	30
2.2.4 Water and lipid absorption.....	31
2.2.5 Scattering .....	31
2.3 Modeling Light Transport for multi-spectral imaging.....	33
2.3.1 Maxwell’s equations .....	33
2.3.2 Radiative Transport Equation.....	33
2.3.3 Standard Diffusion Approximation .....	34
2.3.4 Random Walk Theory.....	35
2.3.5 Two layered skin model.....	38
2.4 Optical Coherence Tomography – Basics and Principles.....	41

2.4.1 Interference of light .....	41
2.4.2 Time and Spectral Domain OCT .....	43
2.4.3 Data Analysis .....	46
<b>METHODOLOGY .....</b>	<b>49</b>
3.1 Multi spectral imaging .....	49
3.1.1 System setup.....	49
3.1.2 Polarization imaging .....	50
3.1.3 Light source and polarizer.....	51
3.1.4 Calibration.....	52
3.1.5 Reconstruction of blood volume and blood oxygenation.....	53
3.2 Optical Coherence Tomography imaging .....	55
3.2.1 System setup.....	55
3.2.2 Data flow .....	57
3.2.3 Post-processing.....	58
 <b>PAPER 1 – DIRECT CURVATURE CORRECTION FOR NON-CONTACT IMAGING MODALITIES – APPLIED TO MULTI-SPECTRAL IMAGING.....</b>	 <b>59</b>
4.1 Abstract .....	59
4.2 Introduction .....	60
4.3 Materials.....	63
4.3.1 Instrumentation.....	63
4.3.2 Reconstruction of blood volume and oxygenation.....	64
4.4 Methods.....	65
4.4.1 Curvature Correction.....	65
4.4.1.1 Known Parametric geometries .....	67
4.4.1.2 Generalized geometries .....	69
4.4.2 Numerical Simulation .....	70
4.4.3 Phantom Experiments .....	71
4.4.4 In Vivo Experiments .....	71

4.5 Results.....	72
4.5.1 Numerical Simulation .....	72
4.5.2 Phantom Experiments .....	76
4.5.3 <i>In Vivo</i> Experiments.....	80
4.6 Discussion.....	84
4.7 Conclusion .....	86
<b>INTERLUDE 1 – IMPORTANCE OF CURVATURE CORRECTION FOR PRINCIPAL COMPONENT ANALYSIS.....</b>	<b>89</b>
5.1 Introduction.....	89
5.2 Principal Component Analysis .....	89
5.3 PCA on raw images .....	90
5.4 PCA on curvature corrected images .....	91
<b>PAPER 2 – PRINCIPAL COMPONENT MODEL OF MULTI SPECTRAL DATA FOR NEAR REAL TIME SKIN CHROMOPHORE MAPPING.....</b>	<b>93</b>
6.1 Abstract.....	93
6.2 Introduction.....	93
6.3 Materials .....	95
6.3.1 Instrumentation .....	95
6.3.2 Occlusion experiments on healthy volunteers .....	96
6.4 Methods .....	96
6.4.1 Reconstruction of skin chromophores .....	96
6.4.2 Principal Component Analysis .....	97
6.5 Results.....	99
6.6 Discussion.....	106

6.7 Conclusion.....	108
---------------------	-----

**INTERLUDE 2 – RECONSTRUCTION-FREE IMAGING OF KAPOSI’S SARCOMA USING MULTI-SPECTRAL DATA .....111**

7.1 Abstract .....	111
--------------------	-----

7.2 Introduction .....	111
------------------------	-----

7.3 Materials and Methods .....	112
---------------------------------	-----

7.3.1 Kaposi’s Sarcoma Patients .....	112
---------------------------------------	-----

7.3.2 Instrumentation.....	113
----------------------------	-----

7.3.3 Reconstruction of skin chromophores.....	113
--	-----

7.3.4 Principal Component Analysis.....	114
---	-----

7.4 Results .....	114
-------------------	-----

7.5 Discussion and Conclusion .....	116
-------------------------------------	-----

**PAPER 3 – QUANTITATIVE PRINCIPAL COMPONENT MODEL FOR SKIN CHROMOPHORE MAPPING USING MULTI SPECTRAL IMAGES AND SPATIAL PRIORS .....119**

8.1 Abstract .....	119
--------------------	-----

8.2 Introduction .....	119
------------------------	-----

8.3 Materials and Methods .....	122
---------------------------------	-----

8.3.1 Multi-Spectral Instrument .....	122
---------------------------------------	-----

8.3.2 Analytical two-layered skin model .....	122
---	-----

8.3.3 Principal Component Analysis.....	123
---	-----

8.3.4 Numerical Phantoms .....	124
--------------------------------	-----

8.3.5 PCA on numerical phantoms.....	125
--------------------------------------	-----

8.3.6 PCA based reconstruction .....	125
--------------------------------------	-----

8.3.7 Thickness dependent error analysis.....	126
---	-----

8.4 Results .....	126
-------------------	-----

8.4.1 PCA applied to numerical phantoms.....	126
--	-----

8.4.2 PCA based reconstruction.....	127
8.4.2.1 PCA based reconstruction of blood volume based on eigenvector 1 .....	128
8.4.2.2 PCA based reconstruction of blood oxygenation based on eigenvector 2	129
8.4.3 Thickness dependent error analysis .....	131
8.4.3.1 Epidermal thickness dependent error in reconstruction.....	131
8.4.3.2 Epidermal thickness dependent error in PCA based reconstruction.....	132
8.5 Discussion.....	133
8.6 Conclusion .....	136
<b>PAPER 4 – IN VIVO VALIDATION OF PRINCIPAL COMPONENT MODELS WITH SPATIAL PRIORS FOR QUANTIFICATION OF MULTI SPECTRAL IMAGES .....</b>	<b>137</b>
9.1 Abstract.....	137
9.2 Introduction.....	137
9.3 Materials and Methods.....	139
9.3.1 Instrumentation .....	139
9.3.2 Skin model based and PCA based reconstruction .....	141
9.4 Results.....	142
9.5 Discussion.....	144
9.6 Conclusion .....	146
<b>CONCLUSION .....</b>	<b>147</b>
<b>BIBLIOGRAPHY .....</b>	<b>151</b>
<b>ACKNOWLEDGEMENTS .....</b>	<b>163</b>



# Chapter 1

## Introduction

### 1.1 Rationale

Non-invasive imaging of skin and other organs is often desired in clinical settings to determine malignancies such as tumors. Over the past centuries, the gold standard for examining the skin has been visual inspection and/or biopsy. The term "biopsy" was introduced into medical terminology in 1879 by Ernest Besnier [Zerbino, 1994] and involved the removal of cells or tissues for examination. Based on these two methods, the first one being subjective, the second one being invasive, the treatment course is being determined. To overcome the ambiguity of visual inspection and invasiveness of biopsy, several imaging modalities have been developed over the last century.

### 1.2 Medical Imaging *in vivo*

#### 1.2.1 Non-optical techniques

Computed Tomography (CT) uses X-rays to generate images, which are slices through the object under examination [Goldman, 2007]. Although different scanning geometries are possible, the principle is the same. An X-ray source is used with a linear detector array with the sample in between. A sheet of X-rays passes through the subject and is being attenuated by the constituents in the sample. Applying the Radon transform to the data, a 3D image of the sample can be acquired. A schematic of a CT system can be seen in figure 1.1.

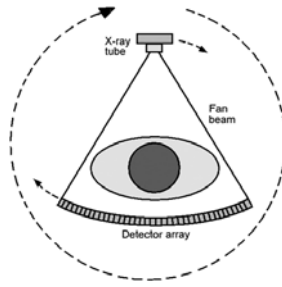


Figure 1.1 Principle of one type of CT. X-rays are shined onto the sample by a fan beam. Large array of detectors measure data across width of fan. Tube and detectors are rigidly linked and undergo single rotational motion. Image taken from [Goldman, 2007]

Positron Emission Tomography (PET) requires introduction of a positron emitting radio-isotope into the sample. The positrons emitted by the isotope quickly annihilate with an electron in the vicinity, resulting in two 0.511 MeV gamma rays. In order to conserve momentum, these photons travel in exactly opposite directions which then can be picked up by the detector array around the sample. The images generated thus represent the radionuclide distribution in the tissue. A schematic of a PET imaging system can be seen in figure 1.2.

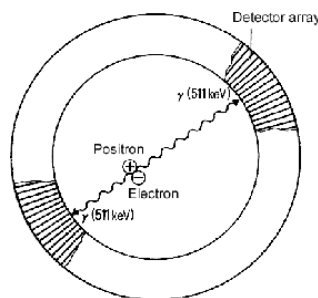


Figure 1.2 Principle of PET. Image taken from <http://www.cs.uni-magdeburg.de/~nroeber/english/intern/node15.html>

Ultrasound imaging uses an ultrasonic emitter of frequency ranging from 0.5MHz to 30MHz as a source. The underlying principle of ultrasound imaging is based on reflection of sound waves launched into the sample. The time delay between sending input and detection of the reflected signal localizes the reflector. The intensity of the reflected signal is proportional to the scattering, thus a tomographic image of the scatterer distribution can be generated.

Magnetic Resonance Imaging (MRI) is based on nuclear magnetization of atoms. Hence, a magnetic field is used to align the (usually) hydrogen atoms in water in the body. Radio frequency (RF) fields are used to systematically alter the alignment of

this magnetization, which causes the hydrogen nuclei to produce a rotating magnetic field. These field changes, or rather the relaxation of those fields, are detectable by the scanner and 3D structural images of high contrast can be produced.

The four imaging modalities named above have different resolution, penetration depth, and yield different information from each other. Figure 1.3 shows a comparison of the imaging modalities in terms of penetration depth and resolution.

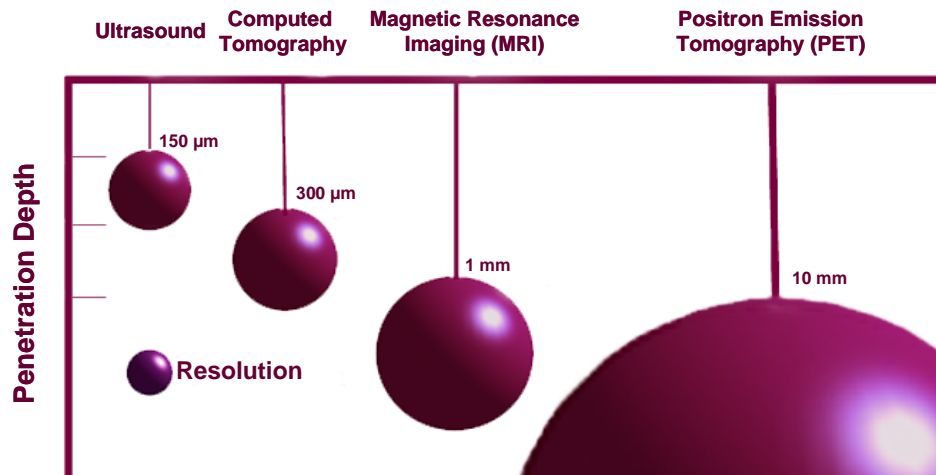


Figure 1.3 Resolution of commonly used medical imaging devices. Image altered from <http://obel.ee.uwa.edu.au/research/oct/intro/>

### 1.2.2 Optical skin imaging

Optical imaging uses light tissue interaction as a source of information. Dependent on the type of imaging modality used, different information about the underlying tissue can be extracted. The general principle is inherent to all modalities, though (figure 1.4). An optical source generates light ( $I_0$ ), which penetrates into the tissue, interacts with the sample constituents, and may re-emerge (a – c in figure 1.4) from the sample to be then measured by a detection unit. The possible interactions can be scattering, absorption (d), or fluorescence (e).

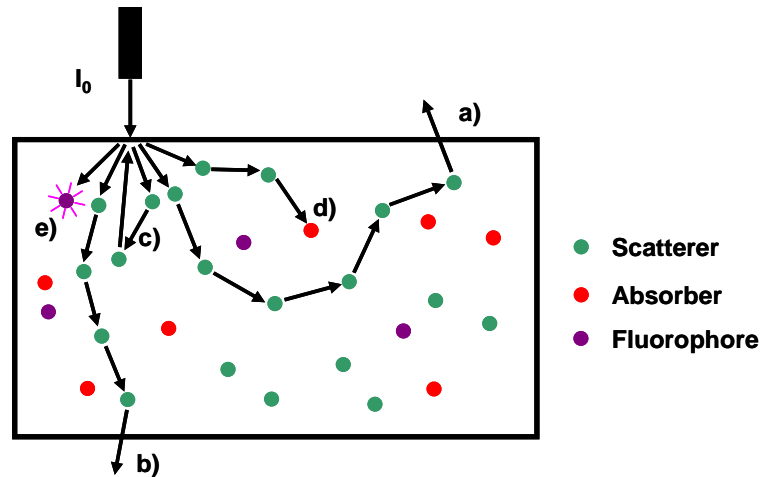


Figure 1.4 Principle of optical imaging. An optical source generates light ( $I_0$ ), which penetrates into the tissue and interacts with the sample constituents by either scattering (a and b), absorption (c), or fluorescence (d).

Based on different optical properties between tissue types, underlying structures and functions can be discriminated. Development of optical modalities for non-invasive skin imaging is, as is the case for most other imaging modalities, driven by the physiological question asked. Depending on the application and information desired, the system needs to have different characteristics. A system configured for one biological setting will be applicable to few others. The main parameters, which will be varying, are spatial resolution, temporal resolution, spectral resolution, as well as dynamic range. Figure 1.5 shows an overview of a few existing modalities and their corresponding resolution vs. penetration depth.

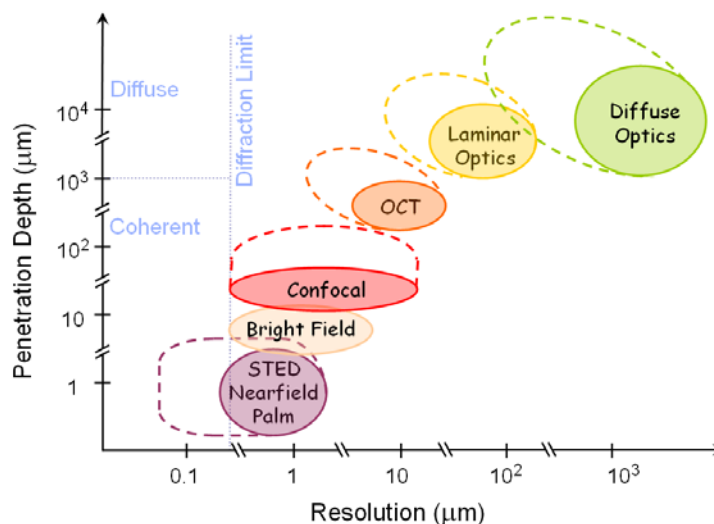


Figure 1.5 Resolution of several optical imaging modalities.

If the metabolic state of a large area of skin is the desired information, spectral resolution might be of high importance. If structural changes on cellular level are of

importance to be observed, a high spatial resolution is desired. Seldom, optical imaging systems combine two complimentary information of the same tissue.

Non-invasive *in vivo* optical imaging can be a powerful tool for skin cancer assessment. Because most skin cancers are located superficially, applying optical imaging methods is not as daunting a problem as imaging deeper cancers, such as breast cancer. The most common non-invasive imaging systems used on the skin include, but are not limited to, dermatoscopy, Laser Doppler Imaging (LDI), thermal imaging, multi-spectral imaging, and Optical Coherence Tomography (OCT).

Dermoscopy is a non-invasive diagnostic tool for the *in vivo* observation of pigmented skin lesions, allowing a better visualization of the surface. It has found its way to the clinic, but is the least quantitative imaging tool of the ones named above, as it heavily relies on the interpretation of the physician. The technique uses white light illumination as well as placing mineral oil, alcohol or even water on the skin lesion for index of refraction matching and subsequent inspection using a hand-held lens, a hand-held scope (also called dermatoscope), a stereomicroscope, a camera, or a digital imaging system. The magnifications of these various instruments range from 6x to 40x and even up to 100x. Such magnification permits the recognition of morphologic structures not visible by the naked eye. But this technique is not quantitative and ultimately relies on user based interpretation, making the subjectivity of the interpreter at risk of ambiguous results.

Laser Doppler Imaging (LDI) measures perfusion (flow) in the skin; typically in arbitrary units. A He-Ne laser is used for illumination and the backscattered and reflected light is collected by a detection unit. Blood flow can be calculated based on the Doppler shift introduced by moving blood cells. Typically, the sample is being scanned in x and y direction yielding to a 2D map of arbitrary blood perfusion units. Perfusion of the skin can be a useful indication of metabolism of underlying malignancies and angiogenesis. The limitations of this technique lie in the difficulties of obtaining quantitative flow measures, making intra and inter subject comparisons of flow difficult if not impossible, as well as not being able to obtain depth information.

Thermal imaging is based on infrared radiation of the human body, which emits maximally at around 10 $\mu$ m. Utilizing a 8 to 12 $\mu$ m camera, the range of human emission can be covered and a 2D image of surface temperature can be obtained. The surface temperature distribution depends on thermal properties (such as thermal conductivity, specific heat) of underlying tissue and subcutaneous vasculature. Higher temperatures

occur in the skin superficial veins that are involved in the active transport of blood. Thermal imaging of the skin is therefore an indirect way of imaging underlying vasculature. The primary limitation of this technique lies in the superficiality of the measurement.

Diffuse multi-spectral imaging systems and the measured quantities vary dependent on the application. For skin imaging, it is widely used for imaging hemoglobin. The inherent similarity of all systems is the measurement of several specific wavelength images (or point measurements). One principle of operation is using white light illumination together with narrow band-pass filters in front of the detection unit, measuring diffuse reflection from the skin, resulting in several specific wavelength images of the same area. Another way of performing the measurement is using specific wavelengths for illumination and tuning the wavelengths. The most dominant wavelength range being used for skin imaging is in the near-infrared (NIR) range. In this wavelength range, hemoglobin is the most dominant absorber and light being backscattered from the tissue will dominantly include information about this chromophore. The diagnostic potential of NIR was first identified by [Horecker, 1943 ], when the absorption characteristics of oxygenated and deoxygenated hemoglobin were found to be quite different at NIR wavelengths, making it possible to distinguish and assess each separately. Using the wavelength dependent intensity variation, reconstruction algorithms can be applied to extract tissue underlying properties. Typical parameters which can be extracted are absorption and scattering coefficient, using generalized reconstruction algorithms, as well as chromophore concentrations, using an analytical or numerical skin model. Details about each of them will be provided in chapter 2. Resulting hemoglobin maps can provide information of the metabolic state of the skin. The inherent limitations of such techniques lie in the resolution, depth discrimination, as well as computational expensiveness of reconstruction algorithms, which make real time assessment of those parameters difficult. The resolution is limited by the nature of diffuse imaging, so is the depth discrimination. The time consuming reconstruction is due to the complexity of the algorithms used for quantification, preventing assessment of information in real time.

Optical Coherence Tomography (OCT) is the only technique of the ones named above, which yields high resolution structural images of the skin. The techniques used above use absorption of light as the contrast mechanism, whereas OCT uses scattering of light for contrast. Based on interference of two partially coherent light beams, depth

can be discriminated with high depth (axial) resolution, typically in the order of a few micrometers. A light source with a Gaussian shaped broad band spectrum is being used for illumination and an interferometric setup is used, with a mirror in the reference arm, the tissue in the sample arm. In a spectral domain OCT setup, reflected light from the tissue is again combined with the reference arm signal and being measured in a spectrometer. Fourier transform of the spectrum yields a depth profile of the tissue. The sample is being raster scanned in x and y direction, resulting in a 3D structural image of the tissue.

Each of the techniques described can be used for gaining different information of the skin; may it be surface changes using dermoscopy, flow changes using LDI, temperature changes using thermal imaging, functional changes using multi-spectral imaging, or structural changes using OCT. Each technique can yield different information, but might not be conclusive when used alone.

Multi-spectral imaging has great potential for quantification of blood volume and blood oxygenation, thus providing functional / metabolic information, but lacks structural information. OCT provides structural information, but does not provide metabolic information. In order to eventually replace the invasive gold standard of biopsy for skin evaluation, both types of information are essential.

Here we are combining those two modalities for skin imaging. The two modalities used are diffuse multi-spectral imaging and Optical Coherence Tomography for assessing the metabolic state of the skin as well as underlying structures. Challenges in transitioning these techniques into clinical routines involve quantification of blood volume and oxygenation as well as assessment of those in real time. Those obstacles led to the following research objectives.

### **1.3 Research Objectives**

- How can the curvature artifact in multi-spectral images be removed?

When imaging diffuse reflection of a large area of skin (several centimeters squared) in a non contact fashion, the shape of the body part can be seen in the intensity distribution. When using reconstruction algorithms, the shape of the object is usually assumed to be flat. If this is not the case, quantification of skin chromophores is difficult.

We have developed a curvature correction algorithm, which removes this artifact without adding any additional measurements to the procedure. The method has been described in the following publication:

J. M. Kainerstorfer, F. Amyot, M. Ehler, M. Hassan, S. G. Demos, V. Chernomordik, C. K. Hitzenberger, A. H. Gandjbakhche, and J. D. Riley, "Direct Curvature Correction for Non-Contact Imaging Modalities – Applied to Multi-Spectral Imaging," *Journal of Biomedical Optics* 15, 046013 (2010).

- Can blood volume and blood oxygenation values be obtained in real time?

Reconstruction of blood volume and blood oxygenation requires post-processing of the multi-spectral data and results can typically not be obtained in real time if the image size is large. For transitioning this technique into the clinic, a real-time algorithm is desired. A model independent method was developed, which uses Principal Component Analysis (PCA) as a basis. We have shown that the PCA results qualitatively correspond to blood volume and oxygenation, making PCA a promising method for analysis. This method has led to the following publication:

J. M. Kainerstorfer, M. Ehler, F. Amyot, M. Hassan, S. G. Demos, V. Chernomordik, C. K. Hitzenberger, A. H. Gandjbakhche, and J. D. Riley, "Principal Component Model of Multi Spectral Data for Near Real Time Skin Chromophore Mapping," *Journal of Biomedical Optics* 15, 046007 (2010).

- Is structural information needed for quantification of blood volume and oxygenation?

When using an analytical model for reconstruction, the underlying tissue structures are often assumed to be known. For reconstruction of blood volume and oxygenation, we have been using a two-layered analytical skin model, with the first layer being the epidermis, the second layer being the dermis. In order to convert the PCA results into actual blood volume and oxygenation values, we performed simulations using the two layered model. We thus developed a PCA based reconstruction, which yield quantitative information. We found that this PCA based reconstruction only performs reliably, if the epidermal thickness is known. This novel PCA based reconstruction has led to the following publication, submitted to *Biomedical Optics Express*:

J. M. Kainerstorfer, J. D. Riley, M. Ehler, L. Najafizadeh, F. Amyot, M. Hassan, R. Pursley, S. G. Demos, V. Chernomordik, M. Pircher, C. K. Hitzenberger, and

A. H. Gandjbakhche, "Quantitative principal component model of multi spectral data for skin chromophore mapping using spatial priors," *Biomedical Optics Express* (submitted).

Since this algorithm has been developed based on simulations, in vivo validation had to be performed. Diffuse multi-spectral imaging in combination with OCT was performed. OCT was used for epidermal thickness extraction, which was used as prior information for the PCA based reconstruction. This in vivo validation led to the following publication:

J. M. Kainerstorfer, J. D. Riley, M. Ehler, L. Najafizadeh, F. Amyot, M. Hassan, R. Pursley, S. G. Demos, V. Chernomordik, M. Pircher, C. K. Hitzenberger, and A. H. Gandjbakhche, "In vivo validation of quantitative principal component models for multi spectral imaging using spatial priors," *Biomedical Optics Express* (submitted).

## **1.4 Thesis outline**

The four publications mentioned above build the cornerstone of this thesis, which is structured in the following way: Chapter 2 contains a concise overview of optical properties in the skin, as well as the basics and principles of reconstruction algorithms for multi-spectral imaging, and the fundamentals of Optical Coherence Tomography. Chapter 3 describes the imaging modalities used in more detail than in the publications. The publication on the curvature correction algorithm is presented in chapter 4. Chapter 5 describes the importance of curvature correction for Principal Component Analysis, which is the basis for the publication presented in chapter 6. Chapter 7 describes PCA applied to Kaposi's sarcoma imaging and the importance of quantification for clinical measurements on the skin, which leads to chapter 8 and 9, which introduce a PCA based reconstruction algorithm in simulation and for in vivo measurements. The conclusion is the final chapter 10.



## Chapter 2

### Basics and Principles

#### 2.1 Optical properties<sup>1</sup>

Optical properties of tissue can be described in terms of:

- Refractive index
- Absorption
- Scattering
- Anisotropy

All of these parameters are also dependent on the wavelength of the light probing the tissue. Additional optical characteristics of tissues include their fluorescence and inelastic scatter properties. Below, the basic principles of the optical tissue properties are described.

##### 2.1.1 Refractive index

The refractive index describes the effect that a medium has on the speed of light passing through it. If a plane electromagnetic wave falls onto a plane boundary between two homogeneous media, the sine of the angle  $\theta_1$  between the normal to the incident wave and the normal to the surface bears a constant ratio to the sine of the angle  $\theta_2$  between the normal of the refracted wave and the surface normal. This constant ratio is equal to the ratio of the velocities of light ( $v_i$ ) in the two media. This law is called Snell's law and can be written as:

$$\frac{\sin \theta_1}{\sin \theta_2} = \frac{v_1}{v_2} \quad (2.1)$$

---

<sup>1</sup> The following subchapters are essentially given by Born, M. & Wolf, E. (1999) *Principles of Optics, 7th ed.*, Cambridge University Press, Cambridge.

The absolute refractive index of a medium is given by  $n=c/v$ , where  $c$  is the speed of light in vacuum. For refraction from the first into the second medium it can be written:

$$n_1 \sin \theta_1 = n_2 \sin \theta_2 \quad (2.2)$$

Refraction at the interface between two materials with different refractive indices can be seen in figure 2.1.

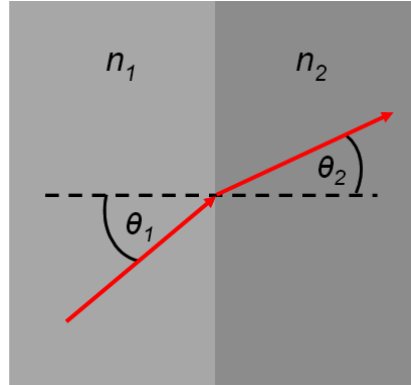


Figure 2.1 Refractive index changes between two media is described by Snell's law.

### 2.1.2 Absorption

If light propagates in a medium with the real refractive index  $n$  being constant, the variation of the space dependent parts of the monochromatic field of frequency  $\omega$  along each ray in the beam is given by the formula [Born & Wolf, 1999]:

$$E_1 = E_0 e^{ik_0 n d}, \quad H_1 = H_0 e^{ik_0 n d} \quad (2.3)$$

where  $k_0=\omega/c$  is the free-space wave number and  $d$  is the distance between two points on the ray.  $E_1$  and  $E_0$  ( $H_1$  and  $H_0$ ) are the space dependent parts of the electric (magnetic) fields at points  $P_1$  and  $P_0$ , respectively.

If the medium is weakly absorbing, the real refractive index  $n$  can be replaced by a complex one, which takes absorption into account.

$$\hat{n} = n(1 + i\kappa) \quad (2.4)$$

where  $\kappa$  is a real constant and called the attenuation index of the medium [Born & Wolf, 1999]. The intensity of the field can be written as the absolute value of the Poynting vector:

$$I = \frac{c}{8\pi} \left| R(E \times H^*) \right| \quad (2.5)$$

where  $R$  denotes the real part. Replacing  $n$  with  $\hat{n} = n(1 + i\kappa)$ , it yields

$$I_1 = I_0 e^{-2k_0 n \kappa d} = I_0 e^{-\mu_a d} \quad (2.6)$$

where  $\mu_a = 2k_0 n \kappa$  is the absorption coefficient of the medium. This intensity law is called Beer's law and holds if a medium is non-scattering and illuminated with light of intensity  $I_0$ . An illustration is given in figure 2.2, where  $d$  is the thickness of the sample illuminated. The absorption coefficient represents the inverse of the length of a photon traveling before being absorbed.

A medium absorption, characterized by  $\mu_a$ , originates from a number of absorbing substances (chromophores) mixed together. The individual extinction coefficients of each chromophore represent their absorption at a particular concentration. The absorption coefficient of a mixture of chromophores can be expressed as the sum of the products of the concentration of each chromophore  $c_n$  times its extinction coefficient  $\varepsilon_n$ .

$$\mu_a(\lambda) = \sum_n \varepsilon_n(\lambda) c_n \quad (2.7)$$

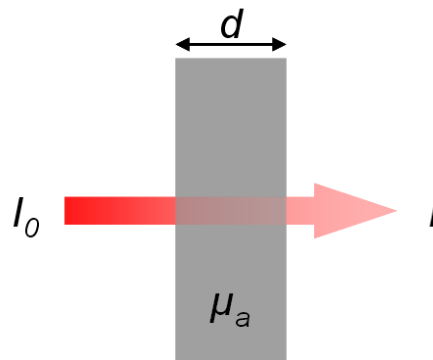


Figure 2.2 Schematic of absorption of light in a slab of thickness  $d$ .  $I_0$  is the emission intensity,  $I$  is the detected intensity.

### 2.1.3 Scatter

The scattering cross section,  $\sigma_s$ , is defined as the area,  $A_s$ , of an index matched, perfectly absorbing disc necessary to produce the measured reduction of light, where the cross section can be written as:

$$\sigma_s = Q_s \cdot A_s \quad (2.8)$$

with  $Q_s$  being the scattering efficiency, defined as the ratio of the scattering cross section to the projected area of the particle on the detector. The scattering

properties of a medium are described by its scattering coefficient  $\mu_s$ . The scattering coefficient is the product of the number density of scattering particles,  $N_s$ , and the scattering cross section of the particles.

$$\mu_s = N_s \cdot \sigma_s \quad (2.9)$$

Therefore  $\mu_s$  represents the inverse of the length before a photon is being scattered. Compared to the non-scattering case above, if a medium is scattering the paths taken by the photons traversing it are no longer direct. This has two effects, which can also be seen in figure 2.3:

- Emerging photons can no longer be measured, unless the detector can collect over all angles and at all points on the surface of the medium.
- Photons will have travelled varying distances through the scattering media.

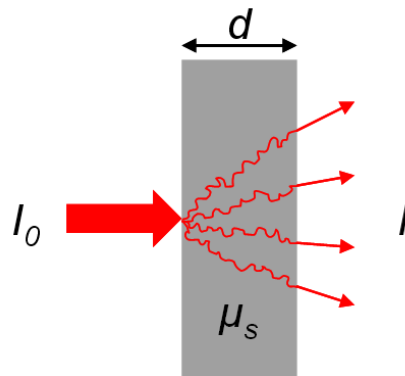


Figure 2.3 Schematic of scattering of light in a slab of thickness  $d$ .  $I_0$  is the emission intensity,  $I$  is the detected intensity.

If the medium is non-absorbing Beer's Law can be used again and we can write the detected intensity,  $I$ , as following:

$$I_1 = I_0 e^{-\mu_s d} \quad (2.11)$$

If the medium is also absorbing the total attenuation of photons travelling in a specific direction can be written as:

$$I = I_0 e^{-\mu_t d} \quad (2.12)$$

where  $\mu_t = \mu_a + \mu_s$ , is the transport coefficient. Light propagation through more complex scattering media than shown in figure 2.3, can be described with both analytical and numerical models, described in more detail in subchapter 2.3.

#### 2.1.4 Anisotropy

The scattering properties of bulk media are often described in terms of the reduced scattering coefficient  $\mu'_s$ . When light scatters off a particular scatterer, the light generally emerges in a preferential direction, with deflection angle  $\theta$ , relative to its incident angle. The scattering coefficient of a material is a function of the number of scatterers. The scattering phase function,  $\rho(r, \hat{\Omega}' \rightarrow \hat{\Omega})$ , which describes the amount of light scattered from one direction  $\hat{\Omega}'$  into another direction  $\hat{\Omega}$ , can be seen in figure 2.4.

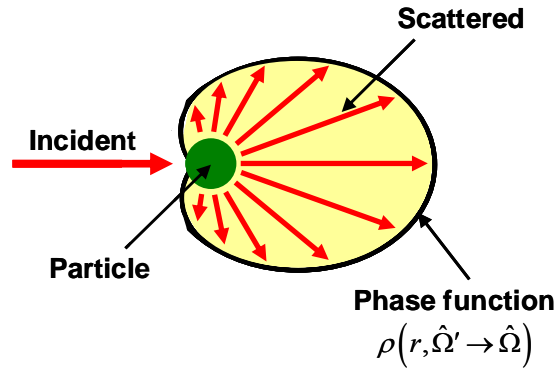


Figure 2.4 Scattering phase function. The incident light beam is scattered by a particle and the phase function describes the amount of light being scattered from one direction into another.

The anisotropy of the scattering is given by the mean cosine of the deflection angle  $\theta$  or the Landé  $g$ -factor  $g$  and allows us to simplify directional effects by using the reduced scattering coefficient  $\mu'_s$  given by:

$$\mu'_s = \mu_s (1 - g) \quad (2.13)$$

where  $g = \langle \cos(\theta) \rangle$ . The purpose of the reduced scattering coefficient  $\mu'_s$  is to describe the diffusion of photons in a random walk of step size  $1/\mu'_s$  [cm], where each step involves isotropic scattering. Such a description is equivalent to description of photon movement using many small steps  $1/\mu_s$  that each involve only a partial deflection angle  $\theta$  if there are many scattering events before an absorption event, i.e.,  $\mu_a \ll \mu_s$ . The following figure 2.5 shows the equivalence of taking 10 smaller steps of "mean free path"  $mfp = 1/\mu_s$  with anisotropic deflection angles  $\theta$  and one big step with a "reduced mean free path"  $mfp' = 1/\mu'_s$ .

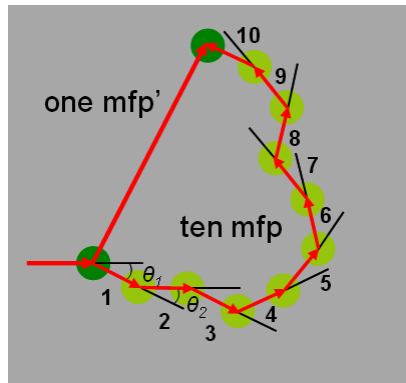


Figure 2.5 Comparison between  $\mu_s$  and  $\mu_s'$ . Ten smaller steps of "mean free path"  $\text{mfp} = 1/\mu_s$  with anisotropic deflection angles is equivalent to one big step with a "reduced mean free path"  $\text{mfp}' = 1/\mu_s'$ .

The scattering cosine depends on the size, shape and refractive index mismatches of the scatterers. If  $g = 0$  then the scatter is isotropic, and if  $g = 1$ , the scatter is entirely forward directed.

## **2.2 The human skin – structure and optical properties**

### **2.2.1 Skin function and structure**

Skin is the largest organ, which is a flexible tissue enclosing the body of vertebrate animals while providing vital protective and metabolic functions. Some of the functions of the skin include a barrier against invasion by outside organisms, protection of underlying tissues and organs from abrasion and other injuries, and shielding the body from the ultraviolet part in sunlight. It also waterproofs the body, preventing excessive loss or gain of bodily moisture. At the human / environment interface, heat is carried away from the body by conduction, convection, radiation, and evaporation and the body maintains a constant body temperature against a wide range of environmental conditions. This is possible because the body's numerous sweat glands excrete waste products along with salty moisture; the fat cells act as insulation against cold; and small blood vessels carry warm blood near the surface to be cooled if needed. The skin is lubricated by its own oil glands, which keep both the outside layer of the epidermis and the hair from drying to brittleness. The mechanism controlling thermal emission and dermal microcirculation, thus temperature control, is driven by the sympathetic nervous system. If a disease is affecting the local thermoregulatory system, changes in the sympathetic function and in the local metabolic rate may occur [Merla A, 2002 ]. The structure of skin, shown in Figure 2.6, contains two main layers of cells: a thin outer layer, the epidermis; and a thicker inner layer, the dermis. The dermis is bonded to a subcutaneous fat layer which may be several centimeters thick [Archambeau JO, 1995]. Optically, the human skin can be described in terms of two different absorbing and scattering layers on top of a nearly totally reflecting collagen layer in the dermis [Anderson & Parrish, 1981; Dawson, 1980; Wan et al., 1981].

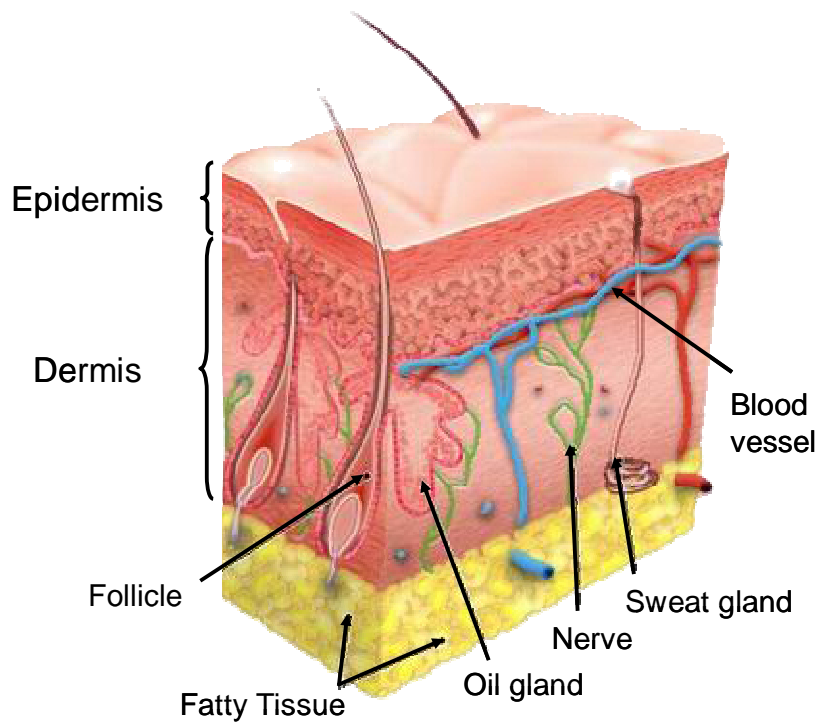


Figure 2.6 Skin structure. The epidermis is the first layer of the skin, followed by the much thicker dermis. Image adapted from [http://www.medical-look.com/Skin\\_diseases/](http://www.medical-look.com/Skin_diseases/)

Contrast in optical imaging is given by the bulk optical properties of the tissue imaged. The following subchapters focus on the absorbing and scattering tissue types in skin, specifically for imaging in the near infrared spectrum.

### 2.2.2 Hemoglobin absorption

The primary absorbing chromophore for light in the near-infrared spectrum in the skin is hemoglobin, which is found in the dermis [Anderson & Parrish, 1981]. It is the iron-containing oxygen-transport metalloprotein in the red blood cells and it makes up about 97% of the red blood cell's dry content. The most common form of hemoglobin found in adult's blood is hemoglobin A. The binding and release of oxygen is dependent on the present conditions. Under certain conditions, oxygen bound to hemoglobin is released into the blood's plasma and absorbed into the tissues. Each hemoglobin molecule has the capacity to carry four oxygen molecules. How much of that capacity is filled by oxygen at any time is called the oxygen saturation, which is the ratio of oxygenated hemoglobin over total hemoglobin, where total hemoglobin is the sum of oxygenated plus deoxygenated. The oxygenation of blood in tissues is related to

tissue blood supply and flow and the oxygen demand and usage of the tissue. Dependent on the amount of oxygen bound to the hemoglobin molecule, two forms can be distinguished – oxygenated hemoglobin (HbO<sub>2</sub>) and deoxygenated hemoglobin (Hb).

The oxygen saturation (SO<sub>2</sub>) can be written as:

$$SO_2 = \frac{[HbO_2]}{[HbO_2 + Hb]} \quad (2.14)$$

The absorption coefficients of oxygenated and deoxygenated hemoglobin differ from each other [Jobsis, 1977b] and can therefore be distinguished with optical methods. Since hemoglobin is the most dominant absorber in the near-infrared spectrum and HbO<sub>2</sub> and Hb can be distinguished, a variety of medical imaging technologies are based on hemoglobin as a natural contrast agent.

Absorption coefficient as defined in equation 2.7, is the product of extinction coefficient and concentration. The spectra for the absorption coefficients for 100% oxygenated hemoglobin,  $\mu_{oxy}$ , and 100% deoxygenated,  $\mu_{deoxy}$ , hemoglobin can be seen in figure 2.7 for the wavelength range between 650nm and 1050nm.

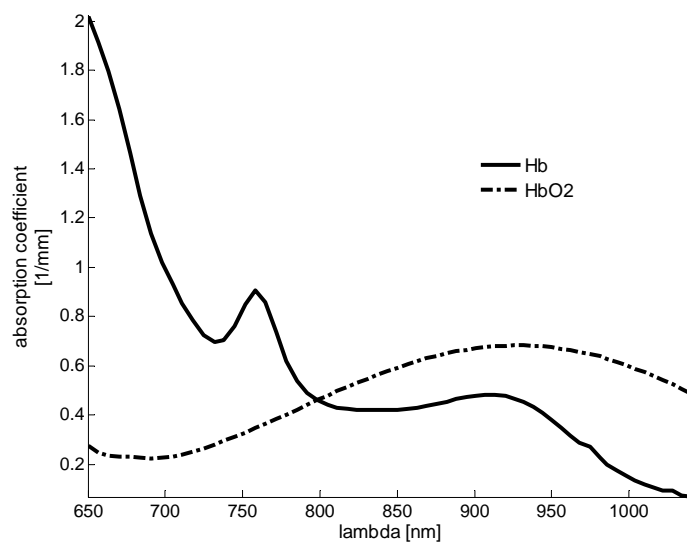


Figure 2.7 Hemoglobin absorption. Graphs are shown for 100% oxygenated hemoglobin and 100% deoxygenated hemoglobin. Spectra taken from [Jacques, 2001].

### 2.2.3 Melanin absorption

For healthy skin, the absorption of the epidermis is dominated by melanin. Melanin is a polymer built by condensation of tyrosine molecules and has a broad absorption spectrum exhibiting stronger absorption at shorter wavelengths. It is found in the melanosomes and is the color giving component of the skin. Therefore, melanin absorption depends on the amount of melanosomes per unit volume in the epidermis. According to [Jacques, 1998], it is estimated that 1.6% - 6.3% of the epidermis volume is occupied by melanosomes in light-skinned adults; in moderately pigmented adults 11% - 16%; and in darkly pigmented adults 18% - 43%.

Researchers have published different wavelength,  $\lambda$ , dependent equations on the absorption coefficient of melanin in the epidermis. Jacques published the following equation [Jacques, 1998] for the melanin absorption coefficient,  $\mu_{mel}$  [mm<sup>-1</sup>], which has been used in the context of this work:

$$\mu_{mel} = 6.6 \cdot 10^{11} \cdot \lambda^{-3.33} \quad (2.15)$$

The absorption coefficient for 100% melanin over the near-infrared wavelength range can be seen in figure 2.8.

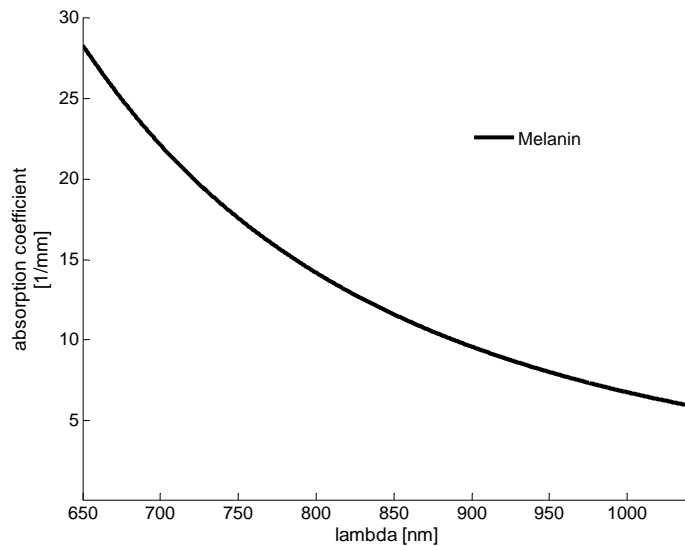


Figure 2.8 Melanin absorption. Graph is shown for 100% melanin. Spectrum taken from [Jacques, 2001].

## 2.2.4 Water and lipid absorption

Because oxy-Hb and deoxy-Hb have quite different optical properties in the visible and near-infrared light range, the concentration of these molecules can be measured using optical methods. Most biological tissues are relatively transparent to light in the near infrared range between 700-900 nm, largely because water, a major component of most tissues, absorbs very little at these wavelengths (Figure 2.9a for 100% water). Also the absorption of fat, which is found in much deeper layers, namely the hypodermis, in the wavelength range below 900nm is low (figure 2.9b for 100% fat, [van Veen et al., 2004]). Because of the low absorption of water and fat, the spectral range named above is often referred to as ‘optical window’ [Jobsis, 1977a; Jobsis, 1977b]. Note that the scales in figure 2.9a and 2.9b are not the same and that water absorption is lower than the absorption of fat.

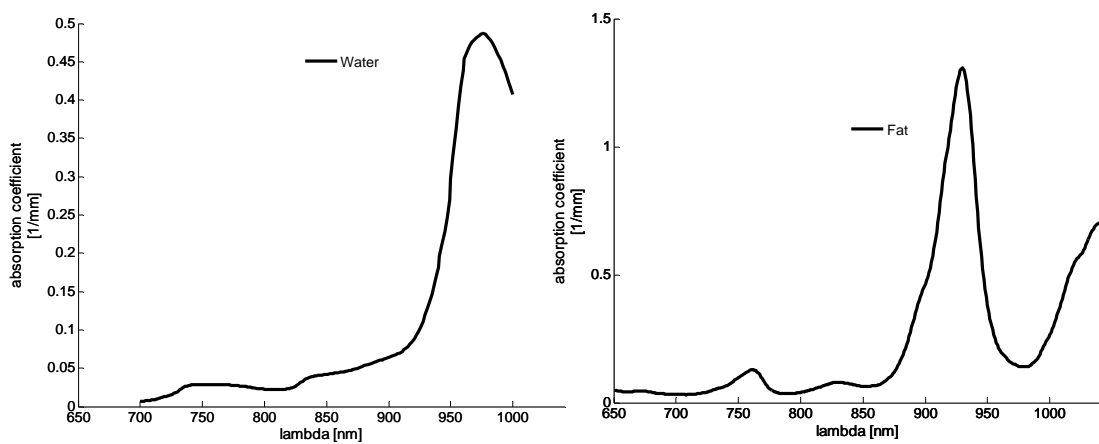


Figure 2.9 Water (a) and fat (b) absorption. Graphs are shown for 100% water and 100% fat. Spectra taken from [Jacques, 2001].

## 2.2.5 Scattering

The scattering coefficient of the epidermis,  $\mu_{s,epi}$ , and the scattering coefficient of the dermis,  $\mu_{s,derm}$ , are very similar [Jacques, 1998] and can be approximated to be the same. Moreover, the thinness of the epidermis makes the details of  $\mu_{s,epi}$  of minor importance for visible and near-infrared applications involving photon diffusion. The anisotropy,  $g$ , of skin tissue typically ranges between 0.7 - 0.95 for skin tissue, and varies with wavelength. However, for the case of photon diffusion, which involves many scattering events, the reduced scattering coefficient,  $\mu'_{s,epi}$ , is of more importance. Here we are referring to  $\mu'_{s,epi} = \mu'_{s,derm} = \mu'_s$ .

The reduced scattering of skin can be described as a combination of Mie scattering and Rayleigh scattering. Mie scattering is due to the large cylindrical dermal collagen fibers, Rayleigh scattering by the small-scale structure associated with the collagen fibers and other cellular structures. It was found [Jacques, 1998] that the contribution of Mie scattering can be written as:

$$\mu'_{s\_Mie} = 2 \cdot 10^4 \cdot \lambda^{-1.5} \quad (2.16)$$

The wavelength dependence of Rayleigh scattering is well known ( $\lambda^{-4}$ ). Its contribution to skin scattering was found to be:

$$\mu'_{s\_Rayleigh} = 2 \cdot 10^{11} \cdot \lambda^{-4} \quad (2.17)$$

The total reduced scattering coefficient of skin can thus be written as:

$$\mu'_s = \mu'_{s\_Mie} + \mu'_{s\_Rayleigh} \quad (2.18)$$

The unit for  $\mu'_s$  is [1/mm] and for the wavelength  $\lambda$  [nm]. The wavelength dependence of the Mie and Rayleigh scattering component, as well as the total reduced scattering coefficient can be seen in figure 2.10.

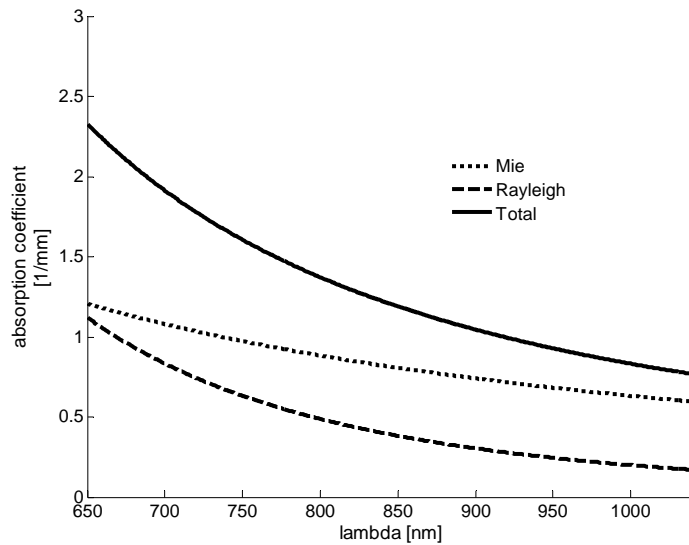


Figure 2.10 Scattering coefficients in the skin. The scattering in the skin can be estimated as a combination of Mie scattering (dotted line) plus Rayleigh scattering (dashed line). The total scattering coefficient is shown in the solid line. Spectra taken from [Jacques, 2001].

## 2.3 Modeling Light Transport for multi-spectral imaging

### 2.3.1 Maxwell's equations

The most rigorous way to model light propagation is given by Maxwell's equations, which treats light as electromagnetic field, i.e. as combination of orthogonally oscillating electric and magnetic components, travelling through time and space. These two vectors, E and H, are the electric vector and the magnetic induction. Electromagnetic wave equations as solutions to Maxwell's equations in homogenous media are given by:

$$\nabla^2 \vec{E} - \frac{\epsilon\mu}{c^2} \frac{\partial^2 \vec{E}}{\partial t^2} = 0 \quad (2.19)$$

$$\nabla^2 \vec{H} - \frac{\epsilon\mu}{c^2} \frac{\partial^2 \vec{H}}{\partial t^2} = 0 \quad (2.20)$$

where  $\epsilon$  is the dielectric constant and  $\mu$  the magnetic permeability, and  $c$  the velocity of light in vacuum. Maxwell's equations can model all wave phenomena, including interference, diffraction, and polarization, on all spatial scales. Modeling light transport in tissue by Maxwell's equations is difficult, since  $\epsilon$  and  $\mu$  of tissue are often unknown and because it is computationally expensive. It has been applied only to small systems and microscopy problems.

### 2.3.2 Radiative Transport Equation

Photon Migration theories in a biomedical optics have been borrowed from other fields such as astrophysics, atmospheric science, and specifically from nuclear reactor engineering [Duderstadt & Hamilton, 1976; Case & Zweifel, 1967]. The common properties of these physical media and biological tissues are their characterization by elements of randomness in both space and time. Because of many difficulties surrounding the development of a theory based on a detailed picture of the microscopic processes involved in the interaction of light and matter, investigations are often based on statistical theories. These can take a variety of forms, ranging from quite detailed multiple-scattering theories [Case & Zweifel, 1967] to transport theory [Ishimaru, 1978]. An approximation of Maxwell's equations for modeling light propagation is the Radiative Transport Equation (RTE), which treats light as the transport of particles

(photons) and uses the optical properties described above, rather than dielectric constant. This approximation is valid if each particle lies in the far-field of the other particle and if there is no correlation between particle positions. This scalar model can not model interference and diffraction effects. Polarization effects can be handled by a transport equation for each Stokes vector component. Modeling with the RTE allows studying systems in the meso scale, compared to the micro scale of Maxwell's equations.

The RTE can be written as:

$$\begin{aligned} \frac{1}{v} \frac{\partial L(r, \hat{\Omega}, t)}{\partial t} + \hat{\Omega} \cdot \nabla L(r, \hat{\Omega}, t) = \\ -\mu_t L(r, \hat{\Omega}, t) + \mu_s \int_{4\pi} L(r, \hat{\Omega}', t) \rho(r, \hat{\Omega}' \rightarrow \hat{\Omega}) d\hat{\Omega}' + Q(r, \hat{\Omega}, t) \end{aligned} \quad (2.21)$$

where  $\mu_t$  is the transport coefficient defined as the sum of absorption plus scattering coefficient.  $\rho(r, \hat{\Omega}' \rightarrow \hat{\Omega})$  is the phase function, describing particles at position  $r$ , moving from the angle  $\hat{\Omega}'$  into angle  $\hat{\Omega}$ .  $Q(r, \hat{\Omega}, t)$  is the volumetric source in

[W/mm<sup>3</sup>].  $\frac{\partial L(r, \hat{\Omega}, t)}{\partial t}$  is the temporal change of radiance  $L(r, \hat{\Omega}, t)$ .

### 2.3.3 Standard Diffusion Approximation

The most widely used modeling of light tissue interaction is the time-dependent diffusion approximation to the radiative transport equation:

$$\nabla^2 \varphi(r, t) - 3\mu_a \mu_r \varphi(r, t) = \frac{3\mu_r}{v} \frac{\partial \varphi(r, t)}{\partial t} - 3\mu_r q_0(r, t) \quad (2.22)$$

where  $\varphi(r, t)$  is the fluence, with  $r$  and  $t$  the spatial and temporal variables, defined as the power incident on an infinitesimal volume element divided by its area.. The reduced transport coefficient is given by  $\mu_{tr} = \mu_a + \mu'_s$ ;  $q_0$  is the source term.

Note that the equation does not incorporate any angular dependence, therefore assuming isotropic scattering. However, for the use of the diffusion theory for anisotropic scattering, the diffusion coefficient is expressed in terms of the transport-corrected scattering coefficient. The diffusion coefficient,  $D$ , related to the absorption and scattering coefficients, can be defined as follows:

$$D = \frac{1}{3(\mu_a + \mu'_s)} = \frac{1}{3\mu_r} \quad (2.23)$$

The diffusion approximation was found to hold if the absorption coefficient is much smaller than the reduced scattering coefficient, hence if  $\mu_a/\mu'_s \ll 1$ . The gradient of fluence,  $J(r,t)$ , is the flux of photons, measured at the tissue surface by the detector:

$$J(r,t) = -D\nabla\phi(r,t) \quad (2.24)$$

For CW measurements, the time-dependence of the flux vanishes, and the source term can be seen as the power impinging in its area. The time dependent diffusion equation has been solved analytically for different types of measurements such as reflection and transmission mode assuming that the optical properties remain invariant through the tissue.

For imaging where the goal is to distinguish between structures in tissue, the diffusion coefficient and the absorption coefficient becomes spatial-dependent. For the cases that an abnormal region is embedded in otherwise homogeneous tissue, perturbation methods based on Born approximation or Rytov approximation have been used (see excellent review in [Arridge & Hebden, 1997]). However for the cases where the goal is to reconstruct the spectroscopic signatures of inclusions in the tissue, no analytical solution exists. For these cases inverse algorithms are devised to map the spatially varying optical properties. Numerical methods such as finite-element or finite difference methods have been used to reconstruct images of breast, brain, and muscle [Nioka et al., 1994; Fantini et al., 1998; Maris et al., 1994]. Furthermore, in those cases that structural heterogeneity exists, a priori information from other image modalities, such as MRI, can be used.

### 2.3.4 Random Walk Theory

Another theoretical framework used in tissue optics is the Random Walk Theory (RWT) on a lattice developed at the National Institutes of Health [Bonner et al., 1987; Gandjbakhche & Weiss, 1995b], which historically precedes the use of the diffusion approximation theory. It has been shown that RWT may be used to derive an analytical solution for the distribution of photon path-lengths in turbid media such as tissue [Bonner et al., 1987]. RWT models the diffusion-like motion of photons in turbid media

in a probabilistic manner. Using RWT, an expression may be derived for the probability of a photon arriving at any point and time given a specific starting point and time.

Tissue may be modeled as a 3D cubic lattice containing a finite inclusion, or region of interest. The medium has an absorbing boundary corresponding to the tissue surface, and the lattice spacing is proportional to the mean photon scattering distance,  $1/\mu'_s$ . The behavior of photons in the RWT model is described by three dimensionless parameters,  $\rho$ ,  $n$ ,  $\mu$ , which are respectively the radial distance, the number of steps, and the probability of absorption per lattice step. In the RWT model, photons may move to one of the six nearest neighboring lattice points, each with probability  $1/6$ . If the number of steps,  $n$ , taken by a photon traveling between two points on the lattice is known, then the length of the photon's path is also known. The idea of the lattice structure can be seen in figure 2.11.

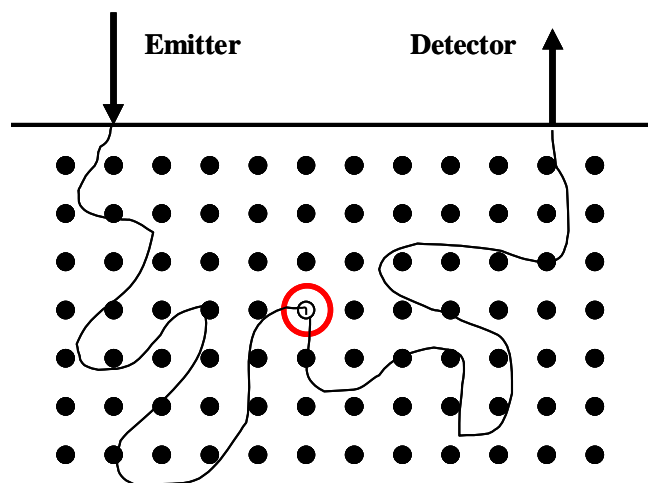


Figure 2.11 2D Random walk lattice showing representative photon paths from an emitter to a specific site and then to a detector.

RWT is useful in predicting the probability distribution of photon pathlengths over distances of at least five mean-photon scattering distances. The derivation of these probability distributions is described in review papers [Bonner et al., 1987; Gandjbakhche & Weiss, 1995b]. For simplicity in this derivation, the tissue-air interface is considered to be perfectly absorbing; a photon arriving at this interface is counted as arriving at a detector on the tissue surface. The derivation uses the Central Limit Theorem and a Gaussian distribution around lattice points to obtain a closed-form solution that is independent of the lattice structure.

The dimensionless RWT parameters,  $\rho$ ,  $n$ ,  $\mu$ , described above, may be transformed to actual parameters, in part, by using time,  $t$ , the speed of light in tissue,  $c$ , and distance traveled,  $r$ , as follows:

$$\rho \rightarrow \frac{r\mu'_s}{\sqrt{2}}; n \rightarrow \mu'_s ct; \mu \rightarrow \frac{\mu_a}{\mu'_s} \quad (2.25)$$

As stated previously, scattering in tissue is highly anisotropic. Therefore the appropriate scaling relationships that will allow the use of an isotropic scattering model such as RWT have to be found. Like diffusion theory, for RWT [Gandjbakhche et al., 1993a], it has been shown that one may use an isotropic scattering model with a corrected scattering coefficient,  $\mu'_s$ , and obtain equivalent results. The corrected scattering coefficient is smaller than the actual scattering that corresponds to a greater distance between isotropic scattering events than would occur with anisotropic scattering. RWT has been used to show how one would transition from the use of  $\mu_s$  to  $\mu'_s$  as the distance under consideration increases [Chernomordik et al., 1996].

As an example, for a homogeneous slab into which a photon has been inserted, the probability  $P$  of a photon arriving at a point  $\rho$  after  $n$  steps mode is [Gandjbakhche et al., 1993b]:

$$P(n, \rho) = \frac{\sqrt{3}}{2} \left[ \frac{1}{2\pi(n-2)} \right]^{3/2} e^{\frac{-3\rho^2}{2(n-2)}} \sum_{k=-\infty}^{\infty} \left[ e^{\frac{-3[(2k+1)L-2]^2}{2(n-2)}} - e^{\frac{-3[(2k+1)L]^2}{2(n-2)}} \right] e^{-n\mu} \quad (2.26)$$

where  $L$  is the thickness of the slab. The method of images has been used to take into account the two boundaries of the slab. Plotting this equation yields a photon arrival curve as shown in figure 2.12; Monte Carlo simulation data are overlaid.

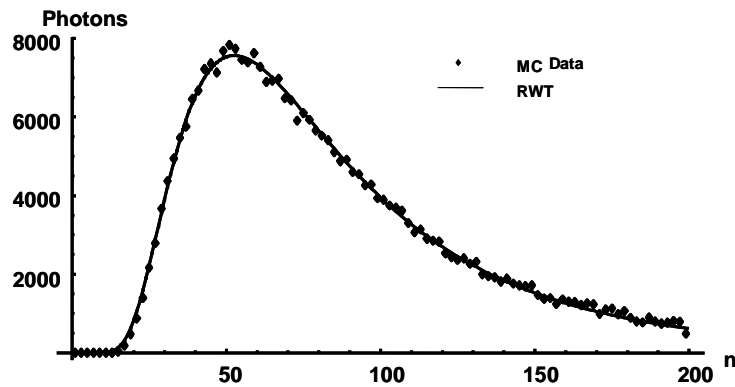


Figure 2.12 Random Walk Theory prediction and Monte Carlo simulation results for transillumination of a 15mm thick slab with scattering 1/mm and  $10^9$  photons.

For the transmittance of light for a finite slab, it can be written:

$$T_0(\mu) = \frac{e^{-2\mu}}{\sqrt{24\mu}} \left[ \frac{\cosh(\sqrt{24\mu}) - 1}{\sinh(L\sqrt{6\mu})} \right] \quad (2.27)$$

For a semi infinite medium ( $L \rightarrow \infty$ ), the transmittance goes to 0.

The Random Walk Theory has been used for modeling light transport in the skin and will be presented for the purpose of using multi-spectral imaging, thus for reflection mode, in the next subchapter in more detail.

### 2.3.5 Two layered skin model

For modeling near-infrared light interaction in the skin, multi-layered models, with as many layers as seven, can be used. An example of a three-layer model (epidermis, papillary upper dermis, and reticular dermis) was published by Zhang [Zhang et al., 2005]. Another example of three layers was published by Andersen et al. [Andersen & Bjerring, 1990a; Andersen & Bjerring, 1990b]. Five-layer skin models (epidermis, capillary blood plexus, dermis, deep blood plexus, and hypodermis) have also been used [Douven & Lucassen, 2000]. Sinichkin et al. used a five-layer model as well, which included the epidermis, papillary derma, upper vessel plexus, reticular derma, and deep vessel plexus [Sinichkin & Uts, 1996]. Kirillin et al. [Meglinski et al., 2008] used a six layered model. Two layered models have been used as well, where the first layer describes the epidermis, the second layer the dermis. One example of such is given by [Mantis & Zonios, 2009].

Here, a two layered model is being described, which has been used in the context of this work. The first layer in this model corresponds to the epidermis, the second layer to the dermis. Since optical properties and dimensions vary between those two, they have to be modeled separately.

The epidermis is the upper layer of the skin. It attenuates light dominantly by melanin absorption, as described in section 2.2.3. Blood vessels are located below the epidermis, thus do not contribute to the attenuation of light. Since the epidermal layer is thin, i.e.  $\sim 100\mu\text{m}$  for the forearm, which is less than 1 mean free scattering path, the attenuation of light in the epidermis can be described by melanin absorption using Beer's Law [Born & Wolf, 1999]:

$$A_e(\lambda) = e^{-\mu_e(\lambda) \cdot d} = e^{-\nu_{mel} \cdot \mu_{mel}(\lambda) \cdot d} \quad (2.28)$$

where  $A_e$  is the light attenuation by the epidermis,  $\mu_e$  is the absorption coefficient by the epidermis,  $d$  is the epidermal thickness. The epidermal absorption coefficient is the product of melanin concentration,  $v_{mel}$ , times the melanin absorption coefficient as described in section 2.2.3.

The dermis is the hemoglobin containing layer. As described in section 2.2.2, hemoglobin in blood is the dominant absorbing chromophore in the near-infrared wavelength range and thus its concentration is the main parameter to be taken into account for modeling the dermis. The influence of the dermis layer on light reflected from the skin can be estimated by random walk theory as described in the previous section. Analogous to equation 2.27, the diffuse reflectance from an infinite slab can be written [Gandjbakhche & Weiss, 1995a]:

$$R_0 = \frac{e^{-2\mu}}{\sqrt{24\mu}} \left[ 1 - e^{-\sqrt{24\mu}} + \frac{2 \left[ 1 - \cosh(\sqrt{24\mu}) \right]}{e^{(L\sqrt{24\mu})} - 1} \right] \quad (2.29)$$

where  $\mu$  is the ratio of absorption and scattering coefficient  $\mu = \mu_a / \mu'_s$ . For a semi infinite medium, the contribution of the *cosh* term disappears for  $L \rightarrow \infty$ , reducing the reflectance to the expression in equation 2.30. Equation 2.30, as a function of  $\mu$ , has been fitted by a power law plus constant. It was shown, that for reasonable values of optical parameters of tissues in the near-infrared spectral range ( $5 \times 10^{-4} < \mu < 0.1$ ), the reflectance in a semi-infinite medium can be approximated as follows:

$$R_0 \approx \frac{e^{-2\mu}}{\sqrt{24\mu}} \left( 1 - e^{-\sqrt{24\mu}} \right) \approx 1.06 - 1.45\mu^{0.35} \quad (2.30)$$

For modeling the dermis, equation 2.30 can be used with  $\mu_a = \mu_d$ , where  $\mu_d$  is the absorption coefficient from the dermis. The attenuation of light by the dermis,  $A_d$ , can thus be written as:

$$A_d = 1.06 - 1.45 \left( \frac{\mu_d}{\mu'_s} \right)^{0.35} \quad (2.31)$$

where the absorption coefficient of the dermis can be approximated as:

$$\mu_d = v_{db} \cdot \left[ (1 - v_{boxy}) \cdot \mu_{deoxy} + (v_{boxy}) \cdot \mu_{oxy} \right] \quad (2.32)$$

where  $v_{db}$  is the total hemoglobin concentration, which will be referred to as blood volume, which can be approximated as the sum of oxygenated and deoxygenated hemoglobin. The concentration of oxygenated hemoglobin is  $v_{boxy}$ , the concentration of deoxygenated hemoglobin thus is  $(1 - v_{boxy})$ .

Combining (2.28) and (2.31), the two layered skin model for diffuse reflection can be written as:

$$I(\lambda) = S \cdot A_e^2(\lambda) \cdot A_d(\lambda) \quad (2.33)$$

where  $S$  is a scaling factor, related to the illumination intensity,  $I(\lambda)$  the reflected intensity from the sample. The scaling factor will be explained in more detail in chapter 3. The attenuation of the epidermis is squared, since light has to pass the epidermal layer twice before being reemitted from the skin.

## 2.4 Optical Coherence Tomography – Basics and Principles

### 2.4.1 Interference of light

This subchapter is essentially based on the description of the theory of electromagnetic waves given by M. Born and E. Wolf [Born & Wolf, 1999] and Fercher [Fercher et al., 2003a]. Going back to the wave description of light, Maxwell's equations can be used (2.19 and 2.20). The Fourier Transform (FT) of the electric field  $E(t)$ , can be written:

$$\hat{E}(\nu) = \int_{-\infty}^{\infty} E(t) e^{(2\pi i \nu t)} dt = FT\{E(t)\} \quad (2.34)$$

which yields the analytical signal, described as:

$$V(t) = 2 \int_0^{\infty} \hat{E}(\nu) e^{(-2\pi i \nu t)} d\nu = A(t) e^{(i\Phi(t) - 2\pi i \bar{\nu} t)} \quad (2.35)$$

$A(t) e^{i\Phi(t)}$  is the complex envelope of  $V(t)$ ,  $A(t) = |V(t)|$  is the real envelope, and  $\bar{\nu}$  is the mean frequency of the power spectrum of  $V(t)$ . The instantaneous intensity is defined as:

$$I(t) = V^*(t) V(t) \quad (2.36)$$

The interference of two light beams can be described as in the Michelson interferometer shown in figure 2.13.

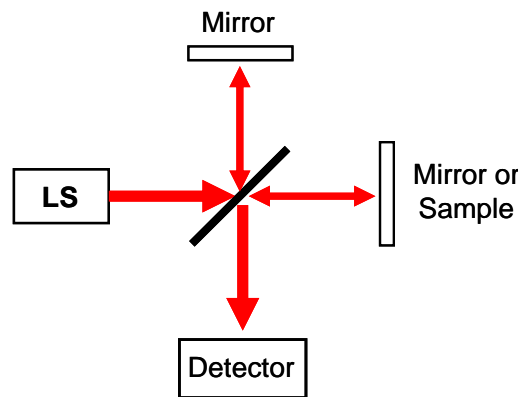


Figure 2.13 Schematic of a Michelson interferometer. Light from a light source (LS) is split in two parts, one going to the reference arm, the second part to the sample arm. At the interferometer exit, both parts are combined again and detected at the detector.

A beam emitted from a light source is split into two parts, each going to a mirror, where they are reflected and recombined again, to be detected by a detection unit. If the path length to mirrors 1 and 2 is not the same, the beams traveled different

distances (thus different times) compared to each other. For OCT setups, one path is called the reference arm (index R), the other the sample arm (index S), which for in vivo measurements is replaced by the sample imaged. The superposition of the two beams at the interferometer exit (index E) can be written as:

$$V_E(t; \Delta t) = V_S(t) + V_R(t + \Delta t) \quad (2.37)$$

where  $\Delta t$  is the time delay caused by the path length differences between the two beams. The averaged intensity at the interferometer exit is given by:

$$I = I_S + I_R + 2 \operatorname{Re}\{\Gamma_{SR}(\Delta t)\} \quad (2.38)$$

where  $I_S$  is the intensity of the sample arm,  $I_R$  of the reference arm,  $\Gamma_{SR}(\Delta t) = \langle \tilde{V}_S(t) \tilde{V}_R^*(t + \Delta t) \rangle$  is the cross correlation function with the angle brackets being the mean ensemble average,  $\tilde{V}_i$  the analytical signal for  $V_i$ . The complex degree of coherence is defined as the normalized cross correlation function:

$$\gamma_{SR}(\Delta t) = \frac{\Gamma_{SR}(\Delta t)}{\sqrt{I_S} \sqrt{I_R}} \quad (2.39)$$

The degree of coherence can be described for three different cases:

- $|\gamma_{SR}(\Delta t)| = 1$ : coherent light – interference is possible for all path length differences
- $|\gamma_{SR}(\Delta t)| = 0$ : incoherent light – no interference is possible
- $0 < |\gamma_{SR}(\Delta t)| < 1$ : partially (low) coherent light

For OCT, only the last case is being used. Interference between two beams is only possible when the time delay between two beams is less than the coherence time ( $\Delta t < t_c$ ). The coherence time is given by:

$$t_c \approx \frac{\lambda_0^2}{c \cdot \Delta\lambda} \quad (2.40)$$

where  $c$  is the speed of light,  $\Delta\lambda$  the bandwidth of the light source,  $\lambda_0$  the central wavelength. For a light source with a Gaussian shaped spectrum the corresponding coherence length can be written as:

$$l_c = \frac{4 \ln(2)}{\pi} \frac{\lambda_0^2}{\Delta\lambda} \quad (2.41)$$

where  $\Delta\lambda$  is the bandwidth of the spectrum at FWHM. Since interference is only possible within the coherence length, it defines the axial resolution in OCT.

## 2.4.2 Time and Spectral Domain OCT

Time domain OCT is historically preceding spectral domain OCT. Both have in common that the sample is being scanned in lateral direction (x-y). Since the backscattered light intensity is recorded as a function of time, the first method is called time domain (TD) OCT [Fercher et al., 1993; Huang et al., 1991a]. In the classical time domain OCT setup, based on a Michelson interferometer, the depth information (in z-direction) is being obtained by translating the reference mirror (see figure 2.13) to introduce path length differences. This depth scan is called axial (A) scan and the interference signal is recorded as a function of depth. For a sample having backscattering sites, which are located at positions  $z_i$ , corresponding to time delays  $\Delta t = (z_i - z_R) / c$ , and from which an intensity  $I_i$  is contributing to the interference signal, the detected A-scan signal at the interferometer exit is given by:

$$I(\Delta t) = I_R + \sum_i I_i + \sum_i \sqrt{I_R I_i} |\gamma_{Ri}(\Delta t)| \cos[\alpha_{Ri} - \delta_{Ri}(\Delta t)] \quad (2.42)$$

with  $i$  being the index for the  $i^{\text{th}}$  layer of the sample in depth,  $\alpha_{Ri}$  being the phase angle,  $\delta_{Ri}(\Delta t)$  being the path length difference dependent phase delay, which is given by  $\delta_{Ri}(\Delta t) = \bar{\omega}\Delta t$ . Scanning the sample imaged in axial and lateral direction (i.e. performing adjacent A-scans) yields a 2D image, which is referred to as B-scan.

Spectral Domain OCT was introduced in 1995, as alternative OCT detection scheme, which is not based on recording interference signals in the time domain but in the spectral (or Fourier) domain [Fercher et al., 1995a]. The spectrum of the interfering reference and backscattered sample light is obtained using a spectrometer. In contrast to the time domain setup, only the lateral scan has to be performed (reference mirror is not moving) A schematic of this spectrometer based setup can be seen in figure 2.14.

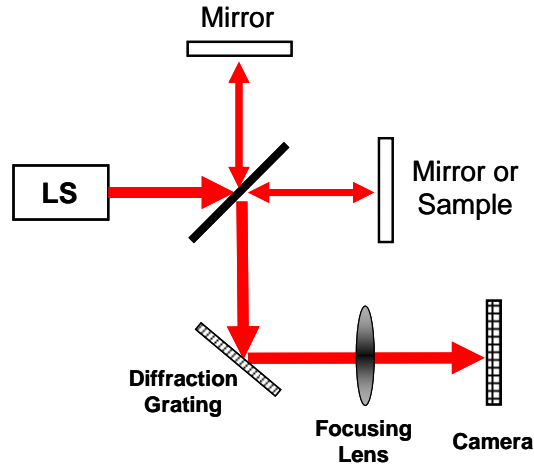


Figure 2.14 Spectral Domain OCT setup. The reference arm is fixed and light, after recombination at the interferometer exit, is detected by a spectrometer unit.

The spectral density can be represented using the cross-correlation  $\Gamma_{ij}(\Delta t) = \langle \tilde{V}_i(t + \Delta t) \tilde{V}_j^*(t) \rangle$ .

$$\Gamma_{ij}(\Delta t) = \langle \tilde{V}_i(t + \Delta t) \tilde{V}_j^*(t) \rangle = 4 \int_0^{\infty} G_{ij}(\omega) e^{-i\omega t} d\omega \quad (2.43)$$

where  $G_{ij}(\omega)$  denotes the cross-spectral density (mutual spectral density). Equivalently, one can write [Born 1999]:

$$\langle V_i(t + \Delta t) V_j(t) \rangle = \int_{-\infty}^{\infty} G_{ij}(\omega) e^{-i\omega t} d\omega \quad (2.44)$$

Equations above show that the spectral density and the real-valued coherence functions  $\langle V_i(t + \Delta t) V_j(t) \rangle$  form a Fourier transform pair.

When the notation  $S_i(\omega) = G_{ii}(\omega)$  is used for the spectral density, a spectral interference law can be derived by means of the Fourier transform:

$$S(\omega) = S_1(\omega) + S_2(\omega) + 2\sqrt{S_1(\omega)}\sqrt{S_2(\omega)}|\mu_{12}(\omega)|\cos[\beta_{12}(\omega) - \delta] \quad (2.45)$$

where the spectral degree of coherence  $\mu_{12}(\omega) = G_{12} / \sqrt{S_1(\omega)S_2(\omega)}$  was used - similar to its counterpart in the time domain - in its polar form  $\mu_{12}(\omega) = |\mu_{12}(\omega)| \exp[i\beta_{12}(\omega)]$  with the phase angle  $\beta_{12}(\omega)$ . The last term on the right hand side is called the spectral interferogram. This spectral law of interference appears mathematically similar to equation 2.38. However, its physical meaning is different: Equation 2.38 describes the change of the average intensity one can observe at the interferometer exit depending on the time delay of the two superimposed waves.

Equation 2.45, however, explains changes in the spectrum of light exiting the interferometer, which are caused by just that run time difference. For a certain run time difference  $\Delta t = t_2 - t_1$ , i.e. for a certain path length difference  $\Delta z = z_2 - z_1$ , the spectrum of the superimposed beams will be sinusoidally modulated by a proportional argument  $\delta = \omega \Delta t$ . Thus, each modulation frequency corresponds to a specific path length difference between the two arms of the interferometer.

The interference phenomenon in the spectral domain is the basis of spectral domain (SD) OCT. When one of the mirrors in Fig. 2.14 is replaced by a sample (e.g., skin), the spectrum of the interference signal will be modulated in several ways. Each of the (N) layers is backscattering a portion  $R_i(\omega)$  of the probing light beam along the z-axis.

Light reflected from the i-th layer has a run time difference  $\Delta t_i - \Delta t_R$  with respect to the beam in the reference arm and a time delay  $\Delta t_i - \Delta t_j$  with respect to the beam returning from the j-th layer. Resulting from interference of sample beams (i, j = 1, ..., N) among each other and with the reference beam (R), the spectral density function at the interferometer exit will be [Gotzinger et al., 2005; Targowski et al., 2004; Wojtkowski et al., 2002]

$$S(\omega) = S_R(\omega) + \sum_i S_i(\omega) + 2 \sum_{i \neq j} |G_{ij}(\omega)| \cos[\omega(\Delta t_i - \Delta t_j)] + 2 \sum_i |G_{iR}(\omega)| \cos[\omega(\Delta t_i - \Delta t_R)] \quad (2.46)$$

The first two terms are the spectral densities of the beams reflected from the reference mirror and each of the N layers. The third term arises from interference among the object beams, i.e. from autocorrelation of the object structure. The last term contains the information about the position of the backscattering layers (with respect to the reference mirror) and their backscattering coefficients  $R_i$ .

Conform to the Wiener-Kintchine theorem, an inverse Fourier transform of equation 2.46 yields the coherence functions

$$FT^{-1}\{S(\omega)\} = \Gamma_{RR}(\Delta t) + \sum_i \Gamma_{ii}(\Delta t) + \sum_{i \neq j} [\Gamma_{ij}(\Delta t + (\Delta t_i - \Delta t_j)) + \Gamma_{ij}(\Delta t - (\Delta t_i - \Delta t_j))] + \sum_i [\Gamma_{iR}(\Delta t + (\Delta t_i - \Delta t_R)) + \Gamma_{iR}(\Delta t - (\Delta t_i - \Delta t_R))] \quad (2.47)$$

Just like in the time domain, also in this expression only the last two terms contain information on the backscattering layers with respect to the reference mirror. They result from the inverse Fourier transform:

$$\begin{aligned}
& FT^{-1} \left\{ 2 |G_{iR}(\omega)| \cos[\omega(\Delta t_i - \Delta t_R)] \right\} = \\
& = \int_{-\infty}^{\infty} I(\omega) \sqrt{R_i(\omega) R_R(\omega)} \cos[\omega(\Delta t_i - \Delta t_R)] e^{-i\omega t} d\omega = \quad (2.48) \\
& = \Gamma_{iR}(\Delta t + (\Delta t_i - \Delta t_R)) + \Gamma_{iR}(\Delta t - (\Delta t_i - \Delta t_R))
\end{aligned}$$

These expressions, which represent the object structure, are symmetric about the position of the reference mirror, i.e. the so-called zero delay. If the backscattering layers of a sample are located such that the light beam travels both a shorter light path than the reference beam (i.e.,  $z_i - z_R = c(\Delta t_i - \Delta t_R) < 0$ ) and a longer path (i.e.,  $z_j - z_R = c(\Delta t_j - \Delta t_R) > 0$ ), the modulations  $\cos[\omega(\Delta t_i - \Delta t_R)]$  and  $\cos[\omega(\Delta t_j - \Delta t_R)]$  will be apparent in the SD-OCT signal (equation 2.46). Since the cosine is an even function,  $f(x) = f(-x)$  holds, i.e.,  $\cos[\omega(\Delta t_i - \Delta t_R)] = \cos[-\omega(\Delta t_i - \Delta t_R)]$ . Hence, for two layers i and j with time delays  $\Delta t_i - \Delta t_R = -(\Delta t_j - \Delta t_R)$ , the cosine term will result in the same values. Two layers located at  $z_i = z_R + \Delta z$  and at  $z_j = z_R - \Delta z$  will modulate the last term of equation 2.46 with the same frequency. After the Fourier transform, the object structures will overlap due to their symmetry with respect to the reference mirror position. This phenomenon leads to the well-known mirror artifacts of SD-OCT. In order to avoid this overlap, the sample is usually placed such that only one half of the depth range (e.g., only  $\Delta z > 0$ ) is used.

### 2.4.3 Data Analysis

The signal being detected in the spectrometer is the spectral data  $S(\omega)$  (equation 2.46) for one A-scan. The depth signal can be calculated by the inverse Fourier Transform of  $S(\omega)$ . The diffraction grating in the spectrometer maps the spectrum onto the detector array of the camera. Dispersion in the grating is given by the grating equation [Born & Wolf, 1999]:

$$m\lambda G = (\sin \alpha - \sin \beta) \quad (2.49)$$

where  $m$  is the order of diffraction,  $\lambda$  the incident wavelength,  $\alpha$  is the angle between the surface normal of the grating and the incident beam,  $\beta$  between the normal and exiting

beam,  $G$  is the grating constant in lines/mm. The mapping of wavelength by the grating on the camera pixels ( $x$ ) can approximately be expressed by [Park et al., 2005]:

$$\lambda(x) = \frac{1}{G} \left[ \beta_0 + \left( 1 - \frac{\beta_0}{2} \right) \left( \frac{x}{f} \right) \pm \dots \pm \sin \alpha \right] \quad (2.50)$$

where  $f$  is the focal length of the focusing lens,  $\beta_0 = \arcsin(G\lambda_0 - \sin \alpha)$ , with  $\lambda_0$  the central wavelength. In order to obtain the object structure, the inversely Fourier transformed spectral interferogram has to be sampled equidistant in the spectral domain, thus in  $\omega$  [Fercher et al., 1995a; Wojtkowski et al., 2002]. If rescaling is not performed, the resolution in depth will not be equal over the pixels and will distort the structure of the image. The wavelengths are mapped on  $N$  pixel of a camera (0 through  $N-1$ ) by:

$$\lambda_i = \lambda_{\min} + \frac{i}{N-1} (\lambda_{\max} - \lambda_{\min}) \quad (2.51)$$

where  $\lambda_{\min}$  and  $\lambda_{\max}$  are the minimum and maximum wavelength,  $i$  is the pixel position. Equidistant mapping in  $k$ -space can be described by:

$$k_j = k_{\min} + \frac{j}{N-1} (k_{\max} - k_{\min}) \quad (2.52)$$

Since the wave number is inversely proportional to the wavelength ( $k \propto 1/\lambda$ ), the new index for interpolation can be written as:

$$i_{\text{new}} = \frac{N-1}{\lambda_{\max} - \lambda_{\min}} \left[ \left( \frac{1}{\lambda_{\max}} + \frac{j}{N-1} \left( \frac{1}{\lambda_{\min}} - \frac{1}{\lambda_{\max}} \right) \right)^{-1} - \lambda_{\min} \right] \quad (2.53)$$

Using the measured signal  $S(\lambda_i)$  and equation 2.53, the new value  $S(k_j)$  can be computed by interpolating  $S(\lambda_i)$ .



## Chapter 3

# Methodology

### 3.1 Multi spectral imaging

#### 3.1.1 System setup

The setup of the system can be seen in figure 3.1. A broadband light source (LS - halogen 150W, Techniquip, Pleasanton, CA) is being used for illumination of the sample, guided through a fiber waveguide, with a ring illuminator at the tip. On top of the ring illuminator, a polarization filter (P1 – Optarius, UK) is being mounted for illuminating the sample with linearly polarized light. Light being backscattered from the sample, passes a second polarizer (P2 – Optarius, UK), perpendicular to the incident polarization plane. Thus, only cross polarized light passes the second polarizer. A rotating filter wheel with six narrowband wavelengths filters (700nm, 750nm, 800nm, 850nm, 900nm, 1000nm and FWHM of 40nm) is positioned after P2. After passing the each filter consecutively, light is being focused (L) onto a CCD camera (16bit, Princeton Instruments CCD-612-TKB, Roper Scientific, 512 x 512 pixels). For in vivo measurements, the distance between the camera and sample surface is being held constant ( $d=50\text{mm}$ ) by two He-Ne lasers (F). The lasers are being tilted in an angle and the sample is placed at the spot of intersection of those two. The camera is controlled with LabView software (National Instruments) and the exposure time was user defined, usually 300ms for white skin and 400ms for black skin.

Description of the underlying polarization imaging, calibration of the spectral and spatial illumination, camera response, as well as fitting procedure (reconstruction) is described in the following subchapters.

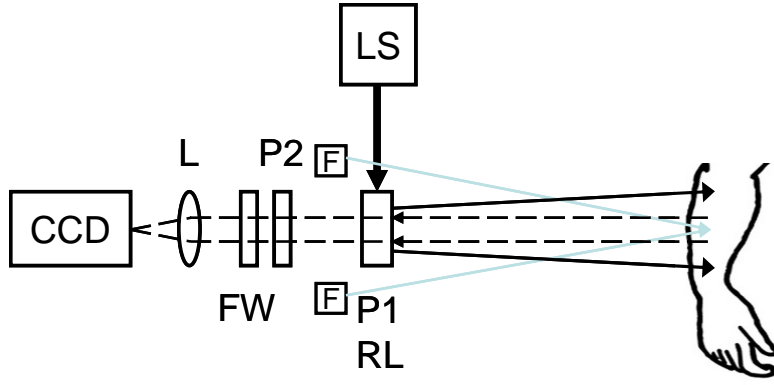


Figure 3.1 Multi-spectral imaging setup. A white light source (LS) is used for illumination of the arm. Two polarizer (P1 and P2) are used for suppressing specular reflection; A filter wheel (FW) is used for selecting specific wavelengths only, and light is focused onto (L) and imaged by the CCD camera.

### 3.1.2 Polarization imaging

The reason for imaging only cross polarized light (P1 – P2) is given by the work of Demos et al. [Demos & Alfano, 1996], which used time resolved imaging and demonstrated that the temporal profiles of polarized laser pulses propagating through scattering media differ for light parallel and perpendicular to the incident polarization. It was also shown, that the degree of polarization is conserved over 100 ps after the arrival of the ballistic component, where the degree of polarization is defined as:

$$D(t) = \frac{I(t)_{\parallel} - I(t)_{\perp}}{I(t)_{\parallel} + I(t)_{\perp}} \quad (3.1)$$

where  $I(t)_{\parallel}$  and  $I(t)_{\perp}$  are the components of the measured pulse intensity in polarization orientation aligned parallel and perpendicular, respectively, compared to the incident polarization. This finding shows that ballistic photons can be separated from diffuse photons, hence surface reflection from light backscattered from deeper layers. This information was used by the same research group for reflection imaging (not time resolved) of deep tissue [Demos et al., 2000]. Since light is being depolarized after  $\sim 5$  mean free scattering lengths [Schmitt et al., 1992], the light backscattered from a scattering medium for the parallel component ( $I_{\parallel}$ ), integrated over the exposure time of the camera, contains the surface reflection plus half of the diffuse light, and the perpendicular component ( $I_{\perp}$ ) contains the other half of the diffuse light.

The system setup used in this work uses only the perpendicular component ( $I_{\perp}(\lambda)$ ) for different wavelengths, hence only the diffuse light penetrating deeper into tissue. Details and changes made from the initial setup are being described in the next subchapters. All results shown throughout the text were acquired with this new system setup.

### 3.1.3 Light source and polarizer

In the course of this thesis, the light source and polarizer have been changed. The light source used in the initial design of the system was a 150 W EKE quartz halogen lamp (Dolan-Jenner Model 180, Edmund Optics, Barrington, NJ). Intensity fluctuations, as great as 40% within one hour of illumination, were found. Therefore the existing source was replaced with another, but more stable, halogen lamp based one, but DC regulated (150W, Techniquip, Pleasanton, CA). The reason for choosing another halogen lamp is based on the smooth white light spectrum. This rather inexpensive solution was sufficient for our needs and the source showed stabilization after 30min warm up time, as can be seen in figure 3.2.

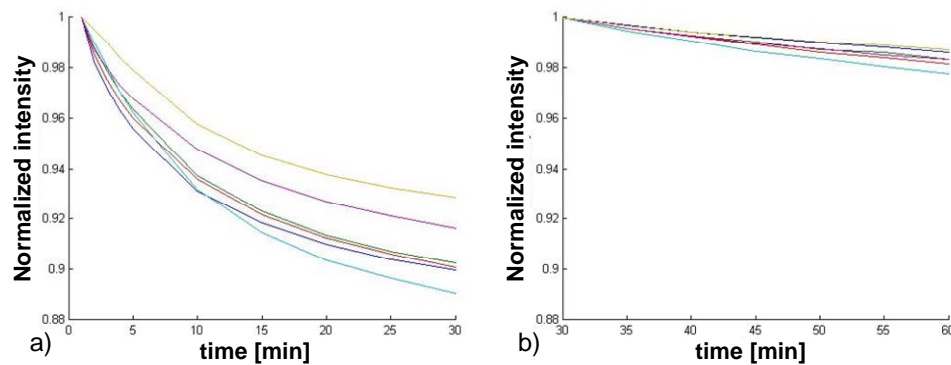


Figure 3.2 Light source intensity over time. The light source was imaged over time and each wavelength is being normalized to  $t=0\text{min}$  (a) and  $t=30\text{min}$  (b). The source shows a decrease in intensity over the first 30 minutes (a) and is stable within 2% decrease after 30 minutes (b).

Polarizers used in the first design of the instrument were laminate film sheet for wavelengths 740 – 2400 nm (Thermo Oriel (now Newport), Stratford, CT), 2 inch in diameter. The first linear polarizer was placed at the output of the light transporting fiber bundle after passing through a red filter (550 nm long wavelength pass) (FS40-NIR-I, CVI Laser, Albuquerque, NM). The red filter was necessary in order to protect the polarizer from excessive heating. The polarizer together with the red filter resulted

in intensity losses of about 1OD each way, which led to necessary exposure times of 900 ms per wavelength image. In order to enhance the transmittance and therefore reduce the exposure time, the original polarizers were changed to glass polarizer (Optarius, UK) with high transmittance and extinction ratios as shown in figure 3.3. By using glass polarizers instead of laminate sheet polarizers, the red filter could be removed and the exposure time could be reduced to 300ms.

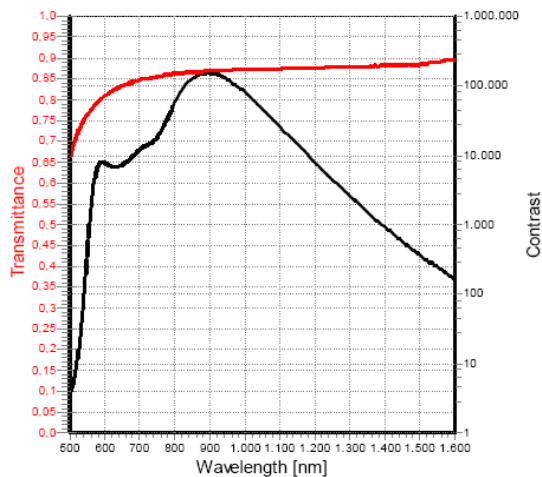


Figure 3.3 Polarizer. Transmittance and Contrast, which refers to the extinction ratio, curve over the NIR spectrum. Picture taken from <http://www.optarius.com/>

### 3.1.4 Calibration

Since the halogen light source does not have a spectrally flat emission spectrum, and since spatial illumination of the sample with the ring light guide is not uniform, spectral and spatial illumination in-homogeneities have to be accounted for. Calibration for both was performed by imaging a standard 90% reflectance reference card (Eastman Kodak, Rochester, NY), which has a flat reflection spectrum in the NIR.

Spatial in-homogeneity is being removed from the raw wavelength intensity images by division of the normalized intensity distribution obtained from the reference card. Normalization was done by dividing the wavelength images of the reference card by their corresponding peak intensity. Figure 3.4a shows a raw 750nm wavelength image of an arm, 3.4b the 750nm normalized reference card image, and 3.4c the corrected image (a divided by b). Inlets in a-c show the same images, but in false color scale for easier visualization of the intensity distributions.

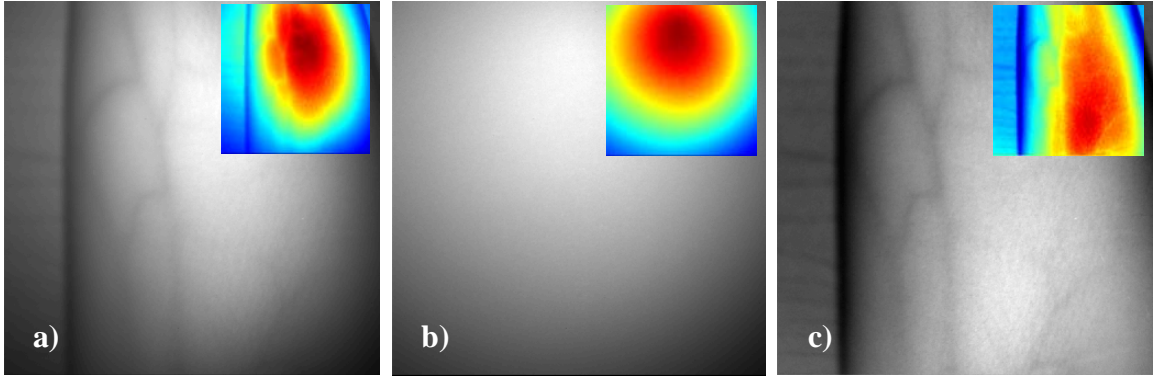


Figure 3.4 Source calibration. An 750nm reflectance image of a lower forearm is seen in a; the reflectance card image in b; a) divided by b) is seen in c), thus with spatial in-homogeneities removed. Inlets show the same area, but in false color to visualize the intensity distributions even better.

Spectral in-homogeneity is being corrected, utilizing the spectral ratio of the six wavelengths images obtained by the reference card and thus acquiring correction factors [Vogel et al., 2007]. Images of the 90% reflectance paper were used to determine the average (over the entire image area) intensity at 700, 750, 800, 850, 900, and 1000 nm. By additional normalization of these values to 1 at 750nm, the correction factors for each wavelength can be extracted. Multiplying the data intensity images by those factors yields spectrally corrected images, which are then used for further processing.

### 3.1.5 Reconstruction of blood volume and blood oxygenation

For reconstruction, the two layered skin model described in chapter 2 was used, shown again in equation 3.2:

$$I(x, y, \lambda) = S \cdot A_e^2(x, y, \lambda) \cdot A_d(x, y, \lambda) \quad (3.2)$$

where  $x$  and  $y$  denote the pixel position, and  $I(x, y, \lambda)$  are the calibrated intensity images. The scaling factor  $S$  in equation 3.2, which is a constant, is a combination of the following parameters:

- $I_0$  – the illumination intensity
- $h$  – the distance between the sample and the camera. This dependence is given by Lambert's law:  $I(\lambda) = I_0(\lambda) \cdot [\cos \theta / h^2]$ , where  $\theta$  is the angle between the surface normal and the detector.
- exposure time of the camera

Since the illumination intensity was not known in this setup, the scaling factor had to be calculated, rather than measured. The unknowns in equation 3.2 are thus  $S$ , blood volume concentration,  $v_{db}$ , blood oxygenation concentrations,  $v_{boxy}$ , melanin content,  $v_{mel}$ , and the epidermal thickness,  $d$ .

Reconstruction was performed in MATLAB (Math Works, Natick, MA) by least squares non linear fitting of the data to the analytical skin model. Four wavelength images were used for reconstruction, being 700, 750, 800, and 850nm. The reason for those wavelengths was that water and fat absorption could be neglected as described in chapter 2.

## 3.2 Optical Coherence Tomography imaging

### 3.2.1 System setup

The basics of OCT have been described in chapter 2. Here, details are being provided about the OCT setup used for this thesis. A fiber based spectral domain OCT system was built, which uses single mode (SM) fibers, thus not preserving polarization, with angle polished (AP) fiber tips. A superluminescence diode light source (DenseLight, Singapore), emitting at  $\lambda_0=1300$  nm with  $\Delta\lambda = 130$  nm and output power 24mW was used, which has an integrated isolator ( $I$ ). The basic setup can be seen in figure 3.5. The interferometer is based on a Michelson interferometer with a 50/50 fiber coupler. The beam is scanned across the sample via an x-y galvo-scanner, where the beam is focused onto the sample surface by an achromatic lens with focal length of  $f=35$  mm. The data flow and triggering of the acquisition is described in more detail in subchapter 3.2.2.

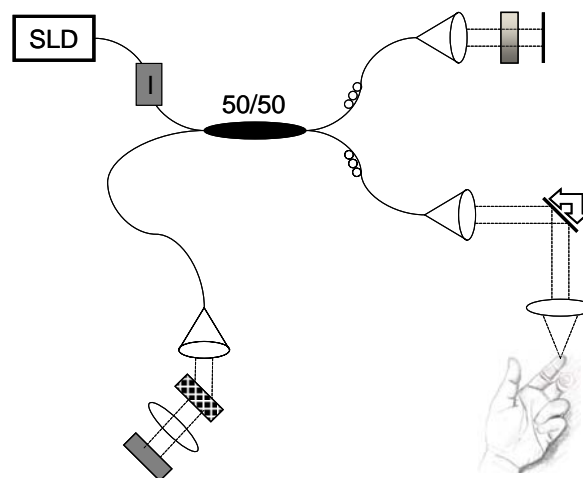


Figure 3.5 SD-OCT setup. A SLD light source is used for illumination. The sample is scanned by galvo-mirrors and the backscattered light from the sample and reference arm is measured in the spectrometer unit.

Optical power at the sample arm was measured to be  $\sim 5$ mW, which is the power used for measuring skin. A variable neutral density filter was used in the reference arm in order to operate the spectrometer camera close to the saturation limit. Both, reference and sample arm, included polarization paddles (Thorlabs) for controlling remaining polarization effects in the fibers. At the fiber tips of reference arm and sample arm, light is being collimated (OZ Optics, Canada), with a beam diameter of 2mm. Given the

beam diameter and focal length of the focusing lens, the transversal resolution  $\delta_x$  can be calculated [Reider, 1997]:

$$\delta_x = \frac{2 \cdot \lambda_0}{\pi \cdot \arctan\left(\frac{D_L}{2f}\right)} \approx 29.2 \mu m \quad (3.3)$$

Given the expression for the coherence length, the axial resolution is given by the full width at half maximum (FWHM) of the coherence function [Swanson et al., 1992]. It is half the coherence length, thus, for a Gaussian shaped spectrum:

$$\delta_z = \frac{2 \ln(2)}{\pi} \frac{\lambda_0^2}{\Delta\lambda} \approx 5.8 \mu m \quad (3.4)$$

which is the axial resolution in air. In tissue, the resolution scales inversely with the refractive index of the sample. In skin, the axial resolution can be estimated as

$$\delta_{z\_skin} \approx 5.8 / 1.42 \approx 4.1 \mu m \quad (3.5)$$

After light is being backscattered from the sample, it is recombined with the reference arm light at the interferometer exit and detected by the spectrometer. At the spectrometer light is being collimated (OZ optics), with a beam diameter of 10mm, and directed onto a diffraction grating (Wasatch, USA) with 1100 lines/mm. The dispersed spectrum is focused by an achromatic lens of 100 mm focal length and recorded with a 1024 element InGaAs line scan camera (Goodrich, Princeton, NJ), with a maximum line rate of 46 kHz.

The spectrum  $S(\lambda)$  is sampled at  $N$  equidistant sampling points by the spectrometer's line scan camera. The sampling theorem states that the maximal detectable modulation frequency is given by the Nyquist limit:  $N/2$  oscillations on the sensor line [Bracewell, 2000]. Hence, after a discrete Fourier transform, the maximum measurable path length difference is [Häusler & Lindner, 1998; Leitgeb et al., 2003; Wojtkowski et al., 2002]

$$\Delta z_{\max} = \frac{\lambda_0^2}{4 \delta\lambda} \quad (3.6)$$

where  $\delta\lambda = (\lambda_{\max} - \lambda_{\min})/N$ , the resolution of the spectrometer.

### 3.2.2 Data flow

The flow of data acquisition in the OCT system (seen in figure 3.6) consists of two National Instruments data acquisition cards and a CameraLink interface card. The first card is used to generate the pixel clock and X axis mirror control signals. The second card is used to generate the line clock and the Y axis mirror control signal. The pixel clock from the first card is routed to both the linescan camera and the second card, where the camera uses this signal to trigger a linescan acquisition (A-scan). Data from the camera is transmitted via a CameraLink bus to the PC. The pixel clock is also used to step through the analog signals controlling the X and Y axis mirrors. The pixel clock is used directly to drive the X axis mirror control signal and to generate the line clock which drives the Y axis mirror control signal.

The user inputs the pixel clock rate (A-scan rate), the number of pixels per line (B-scan size), and the number of B-scans per frame into the graphical user interface (GUI) of the OCT system. The program computes the rate of the line clock and generates the signals needed to trigger the camera and control the X and Y mirrors. The data is accumulated line by line, each representing a B-scan in the XZ plane.

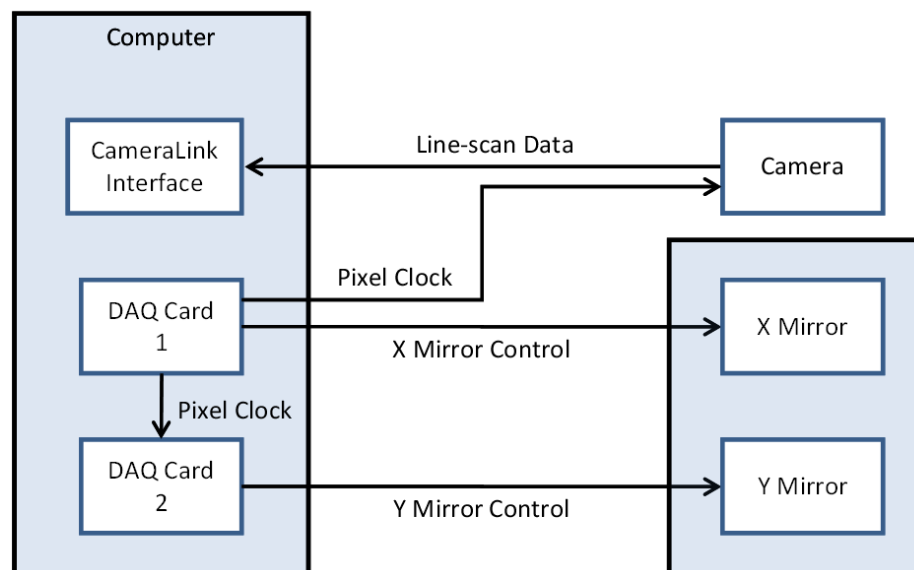


Figure 3.6 Data acquisition. The diagram shows the flow of triggering signals for acquiring 3D OCT data sets.

### 3.2.3 Post-processing

The post-processing of the data was done in Matlab (Math Works, Natick, MA). Each 3D data set was processed one B-scan after the other. Given the description in chapter 2, the data is first interpolated to have equidistant mapping in spectral domain ( $S(\lambda_i) \rightarrow S(k_j)$ ), using equation 3.7:

$$i_{new} = \frac{N-1}{\lambda_{max} - \lambda_{min}} \left[ \left( \frac{1}{\lambda_{max}} + \frac{j}{N-1} \left( \frac{1}{\lambda_{min}} - \frac{1}{\lambda_{max}} \right) \right)^{-1} - \lambda_{min} \right] \quad (3.7)$$

where  $\lambda_{min}=1150\text{nm}$ ;  $\lambda_{max}=1570\text{nm}$ ;  $N=1024$ ;  $j=0, \dots, 1024-1$ .

After interpolation, each spectral B-scan is averaged along the x-axis, resulting in the Gaussian shaped source signal, which is then subtracted from each A-scan, leaving only the modulated depth dependent signal (the spectral interferogram). This step removes the DC (direct current) component of the signal and also pattern noise. Fourier transforming the signal for each A-scan yields the desired depth information.

## Chapter 4

# Original paper 1 – Direct Curvature Correction for Non-Contact Imaging Modalities – Applied to Multi-Spectral Imaging

### 4.1 Abstract

Non-contact optical imaging of curved objects may result in strong artifacts due to the object's shape, leading to curvature biased intensity distributions. This artifact can mask variations due to the object's optical properties and makes reconstruction of optical/physiological properties difficult. In this work we demonstrate a curvature correction method, which removes this artifact, and recovers the underlying data, without the necessity of measuring the object's shape. This method is applicable to many optical imaging modalities, which suffer from shape based intensity biases. By separating the spatially varying data (e.g. physiological changes) from the background signal (DC component), we show that the curvature can be extracted by either averaging or fitting the rows and columns of the images. Numerical simulations showed that our method is equivalent to directly removing the curvature, when the object's shape is known, and accurately recovers the underlying data. Experiments on phantoms validated the numerical results and showed that for a given image with 16.5% error due to curvature, the method reduces that error to 1.2%. Finally, diffuse multi-spectral images were acquired on forearms *in vivo*. We demonstrated the enhancement in image quality on intensity images and consequently on reconstruction results of blood volume and oxygenation distributions.

## 4.2 Introduction

Over recent years, the unique potential of optical imaging for disease diagnostics and treatment monitoring has become evident. This has resulted in the rapid development of different optical modalities for biomedical imaging. Some of these techniques have been already moved from bench to bedside. Besides the non-ionizing nature of optical methods and their relatively cheap implementation, an attractive feature of optical imaging is that it is usually minimally invasive, often being realized as a non-contact imaging technology, e.g., near-infrared fluorescence imaging [Kovar et al., 2007], colorimetry [Miyamoto et al., 2002; Pladellorens et al., 2008], tissue reflectance spectroscopy [Riordan et al., 2001], polarization imaging [Bae et al., 2008; Demos & Alfano, 1997a; Jacques et al., 2000], Pearson correlation imaging [Sviridov et al., 2005a; Sviridov et al., 2005b; Sviridov et al., 2006], and diffuse multi-spectral imaging [Arimoto, 2006; Arimoto, 2007; Attas et al., 2001; Cuccia et al., 2005; Vogel et al., 2007; Vogel et al., 2006]. Though more convenient or even practical for many clinical applications, non-contact imaging can become a quantitative technique, only if data processing adequately takes into account the shape of the target object (e.g., body surface). The bias, introduced into optical images by the surface curvature of the object, can mask real distributions of optical characteristics of the media which characterize physiological status of the region of interest, making even qualitative assessment impossible without specially developed methods to remove curvature related image artifacts.

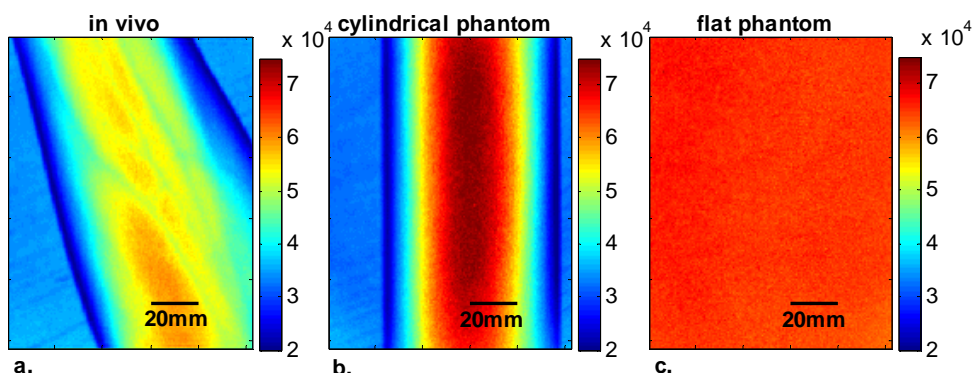


Figure 4.1 Examples of multi-spectral intensity images containing the curvature effect are shown. (a) Shows an intensity image of a healthy volunteer's lower arm, (b) an intensity image of the cylindrical phantom and (c) the flat phantom. Images shown were taken at a wavelength of 800nm.

An example of the curvature effect can be seen in Figure 4.1a and 4.1b, where we see the distortion of the images due to curvature. The images were acquired by diffuse reflectance imaging at a wavelength of 800nm and respectively show a volunteer's forearm and a cylindrical phantom. For comparison, Figure 4.1c shows an image of a flat phantom with the same optical properties as the cylindrical one, but no curvature.

When trying to remove the effect of curvature on reflected intensity, two general approaches are possible. Either the object's shape is being measured and taken into account or the curvature effect, which is the intensity bias, is being extracted. Several methods aimed at curvature artifact correction have been discussed recently in the literature. These approaches include hardware modification, changes in the measurement protocol and image processing techniques to qualitatively reduce the curvature effect. All these approaches have in common that the shape is being extracted rather than the effect of shape. Westhauser et al [Westhauser et al., 2008] illuminated the object with fringe patterns and acquire data from three cameras for extracting the surface curvature. Another approach is to use structured light generated by a beam splitter mounted on a laser diode and reconstructing the surface by an optical triangulation approach [Paquit et al., 2007; Paquit et al., 2006]. However, these approaches require hardware modification and additional measurements to extract the shape of the object before extracting and removing the intensity artifacts. Gioux et al [Gioux et al., 2009] combined phase-shifting profilometry for shape extraction and modulated imaging for optical properties measurements into one single instrument. The same group showed that modulated imaging is a powerful tool for reconstruction of absorption and scattering coefficient and that low spatial frequencies are maximally sensitive to absorption contrast [Cuccia et al., 2009]. The combination of these approaches into one machine does therefore not require any hardware modification, but still additional measurements. Another approach was developed by Zeman et al., which is based on image processing and which is used for non-quantitative image enhancement [Zeman et al., 2005]. This is not a correction model, however, and is not useful for quantitative modeling as it cannot provide real intensity values. At this time, no techniques, to our knowledge, have been proposed for quantitative curvature extraction and removal in the images which do not involve additional measurements.

In this paper we are introducing a correction method, which extracts and corrects the curvature intensity bias, rather than measuring the shape of the object. It is not

dependent on the imaging modality and does not require any additional measurement on the object. To demonstrate and evaluate the method, we are considering the case of diffuse multi-spectral imaging, which measures the diffuse reflection from the skin, using a flat light illumination. Spatial frequencies in the data are therefore not sensitive to absorption contrast. This technique is used to reconstruct and map blood volume and blood oxygenation concentrations. The acquired images are often biased by the curvature of the objects [Arimoto, 2006; Arimoto, 2007; Attas et al., 2001; Cuccia et al., 2005; Vogel et al., 2007; Vogel et al., 2006]. This problem has to be addressed after acquisition of the images because clinical protocols typically prohibit patient skin manipulation to flatten the skin surface for curvature removal.

The method we are proposing for extracting and correcting the curvature effect is computationally inexpensive, adding only a few seconds to the analysis, and robust, as we will be demonstrating in the results section. It is based on the diffuse reflectance images acquired and does not require additional measures of the objects shape. As it is based on intensity images, it can be applied to any imaging modality, which captures diffuse reflectance images. In our approach, the curvature effect can be removed from existing data, by either averaging or fitting of the intensity images, without direct shape reconstruction. Our goal is to separate the effects of curvature and skin chromophore variations in the images. We demonstrate that the curvature effect can be separated by either averaging or fitting the rows and columns of the image, giving access to the chromophore dependent variation. Limitations of the method lay in the object's shape when using the averaging approach and in the choice of fitting function used for the fitting approach. The advantage of this suggested method is not only that no additional measures are necessary, but also that previously collected data can be re-analyzed to remove curvature effects.

In order to demonstrate the strengths and limitations of the method we applied it to numerically simulated objects, phantoms, and in vivo data. We would like to point out that the cases presented here are examples for demonstrating the performance of the algorithms, which might differ for different objects imaged. For the interested reader and for trying the method on images of different geometry than described here, the Matlab codes can be obtained from the corresponding author.

In the first part of the paper, we show the application of curvature correction in the case of numerically simulated objects. In the second part, we describe phantom experiments performed on cylindrical and flat objects to validate the technique

experimentally. Finally, the fitting method is applied using *in vivo* acquired multi-spectral images. We demonstrate the enhancement in image quality on raw intensity images and consequently on reconstruction results of blood volume and oxygenation distributions.

## 4.3 Materials

### 4.3.1 Instrumentation

A non-invasive, non-contact diffuse reflectance multi-spectral imaging system was developed in cooperation with Lawrence Livermore National Laboratory [Vogel et al., 2007; Vogel et al., 2006]. Polarized light from a white light source (halogen 150W, Techniquip, Pleasanton, CA) is used for flat illumination of the sample imaged. A second polarizer (Optarius, UK) is placed before the detection unit, perpendicular to the incident beam polarization, thus guaranteeing diffuse reflectance measurements and removal of specular reflection [Demos & Alfano, 1997a].

The distance ( $h$ ) between the sample and detection unit was held constant ( $h=500mm$ ), by using two He-Ne lasers at a fixed angle. The highest point of the sample was placed at the point where the two lasers intersect.

Light is then captured in a CCD camera (Princeton Instruments CCD-612-TKB, Roper Scientific) after passing consecutively one of six narrow bandpass filters (40nm FWHM, FS40-NIR-I, CVI Laser, Albuquerque, NM) on a filter wheel. Six wavelength images are taken, the wavelengths being 700, 750, 800, 850, 900 and 1000nm. Only the first four wavelengths were used for further analysis in order to avoid water and lipid absorption.

For calibration purposes, images from a 90% reflectance paper (Kodak) are taken. The raw wavelength intensity images are being divided by the normalized intensity distribution from the paper in order to remove spatial inhomogeneity from the illumination. Spectral inhomogeneity from the source is being corrected for by utilizing the spectral ratio of the six wavelengths images of the paper and thus acquiring correction factors [Vogel et al., 2007]. These corrected images are then used for further processing and will be referred to as ‘raw’ intensity images.

### 4.3.2 Reconstruction of blood volume and oxygenation

*In vivo* data acquired from healthy volunteers' forearms using diffuse multi-spectral imaging was used for reconstruction of blood volume and oxygenation. Reconstruction was performed in MATLAB (Math Works, Natick, MA) by least squares non linear fitting of the data to our analytical skin model [Vogel et al., 2007]. Four wavelength ( $\lambda$ ) images were used for reconstruction, being 700, 750, 800, and 850nm. The analytical skin model used is based on a two layered structure, the first one being the melanin containing epidermis, the second one being the blood containing dermis. Optical properties of the skin were taken from literature values [Jacques, 1998; Meglinski & Matcher, 2002; Prah1, 1998] and are summarized in table 1. Our model is given as:

$$I_e(x, y, \lambda) = S \cdot A_e(x, y, \lambda)^2 \cdot A_d(x, y, \lambda) \quad (4.1)$$

The attenuation by the epidermis,  $A_e$ , is based on Lambert's law and can be written as:

$$A_e(\lambda) = e^{-\mu_e \cdot d_e} = e^{-(v_m \cdot 0.66 \cdot 10^{11} \cdot \lambda^{-3.33} \cdot d_e)}, \quad (4.2)$$

where  $v_m$  is the concentration of melanin,  $d_e$  is the thickness of the epidermis and  $\mu_e$  is the absorption coefficient of the epidermis, which is based on the absorption of melanin. The attenuation by the dermis,  $A_d$ , which includes the absorption due to blood volume and oxygenation, is based on the analytical solution of photon migration in turbid media based on random walk theory [Gandjbakhche & Weiss, 1995a] and can be written as:

$$A_d(\lambda) = \frac{e^{-2(\mu_d / \mu'_s)}}{\sqrt{24(\mu_d / \mu'_s)}} \cdot \left(1 - e^{-\sqrt{24(\mu_d / \mu'_s)}}\right) \approx 1.06 - 1.45 \cdot (\mu_d / \mu'_s)^{0.35}, \quad (4.3)$$

where  $\mu'_s$  is the reduced scattering coefficient and  $\mu_d$  is the absorption coefficient of the dermis, defined as:

$$\mu_d = v_{db} \cdot \left[ (1 - v_{boxy}) \cdot \mu_{deoxy} + (v_{boxy}) \cdot \mu_{oxy} \right], \quad (4.4)$$

The scaling factor  $S$ , blood volume,  $v_{db}$ , and blood oxygenation,  $v_{boxy}$ , are unknown a priori and were solved for.

Wavelength (nm)	$\mu_{deoxy} [mm^{-1}]$	$\mu_{oxy} [mm^{-1}]$	$\nu_m * \mu_{mel} [mm^{-1}]$	$\mu'_s [mm^{-1}]$
700	1.068	0.232	1.772	1.912
750	0.788	0.330	1.408	1.606
800	0.478	0.468	1.136	1.372
850	0.424	0.583	0.928	1.190

## 4.4 Methods

In this section, we explain in detail our curvature correction method which uses either averaging of intensity images or fitting of intensity images. Potentially each of these algorithms can be applied. However, depending on the nature of the acquired images, one may provide more accurate results than the other. After this we describe the specific model of skin chromophores incorporated into our diffuse multi-spectral imaging system. This system provides a good example for using the curvature correction because it acquires diffuse reflectance images in a non-contact fashion of objects where the curvature effects are expected to be considerable.

### 4.4.1 Curvature Correction

Our curvature correction algorithm, is based on extracting the curvature effect on intensity images, and does not require additional measures of the shape of the object. It is applicable when the curvature effect is stronger than signals due to intrinsic changes. If the curvature of the object causes intensity variations, which are smaller than intrinsic changes, the curvature effect may be considered negligible. From now on, we will refer to these changes as physiological changes, e.g. due to hematological variation. One may consider physiological changes on top of curvature as variations on top of a carrier frequency, much like AM radio signal. Extracting the curvature is similar to removal of the carrier frequency, which makes the signal (physiologically significant information) available.

The raw detected intensity  $I_r(x,y)$ , which is the intensity after correcting for spatial and spectral in-homogeneities of illumination, at image pixel position  $(x,y) \in \{1, \dots, n\} \times \{1, \dots, m\}$ , where n and m are the total number of pixels in the horizontal

and vertical image axis respectively, can be described as a function of emitted intensity ( $I_e(x,y)$ ) from the sample surface, the distance of the detector from the object's surface ( $h(x,y)$ ) and the angle between the surface normal of the object and the direction to the detector ( $\theta(x,y)$ ). Assuming Lambertian reflection, we can write this dependence as

$$I_r(x,y) = C(x,y) \cdot I_e(x,y), \quad (4.5)$$

where  $C(x,y) = \cos(\theta(x,y))/h^2(x,y)$  is the curvature term. The assumption of diffuse reflection is valid for our multi-spectral imaging system, as the cross polarizer used removes specular reflection.

Given a separate measure of the surface, one can eliminate the curvature effect directly using this equation. In the absence of such measures, we may extract the curvature by considering it as an intensity effect. To do this, we must first recast Equation 4.5, separating the background intensity,  $I_b$  (DC component of the signal, constant), and information intensity,  $I_d(x,y)$  (physiologically significant information, spatially varying). This gives us

$$I_r(x,y) = C(x,y) \cdot (I_b + I_d(x,y)), \quad (4.6)$$

where the background  $I_b$  is independent of  $x$  and  $y$ . It will turn out that if we assume that the physiological signal  $I_d(x,y)$  is much weaker than the background  $I_b$  ( $I_d(x,y) \ll I_b$ ), where the magnitude of  $I_b$  is in the order of the average image intensity, we can extract and eliminate the curvature effect  $C(x,y)$ . If this assumption is violated, then the method may perform poorly. We will demonstrate in the results section that the assumption  $I_d(x,y) \ll I_b$  is valid for our physiological data.

If we further assume that the distance  $h(x,y)$  between the camera and the sample is much bigger than the elevation changes of the sample's surface that is due to the curvature, then  $h$ 's dependency on  $x$  and  $y$  is negligible. In the following we treat  $h$  as a constant height component that we put into  $I_b$  and  $I_d$  such that the curvature term becomes only angle dependent. We can then recast equation (4.6):

$$I_r(x,y) = C'(x,y) \cdot (I'_b + I'_d(x,y)), \quad (4.7)$$

where  $C'(x,y) = \cos(\theta(x,y))$ ,  $I'_b = I_b/h^2$ , and  $I'_d(x,y) = I_d(x,y)/h^2$ , with  $I'_b$  and  $I'_d$  being the background and data signal at height  $h$ , which is the smallest distance between the surface and camera (highest point of the sample). If the measurement is being focused on this point,  $h$  corresponds to the focal distance. We developed two different and independent algorithms to extract  $C'(x,y)$ . The use of one or the other depends on the geometry of the imaged object.

#### 4.4.1.1 Known Parametric geometries

For our first method we assume that the curvature term  $C'$  only changes along the  $x$  and  $y$  axis, i.e., there are two functions  $C_1$  and  $C_2$ , that do not have to be further specified, such that

$$C'(x,y) \approx C_1(x) \cdot C_2(y). \quad (4.8)$$

For instance, this assumption holds if the object is cylindrical and aligned to either the  $x$  or  $y$  axis in the image. This applies to any geometry which can be described in a separable two part parametric function. We note, however that this requires knowledge of the underlying geometry, for example in an elliptical geometry we would need to know it's center.

The second assumption, that was already mentioned, is that the physiological signal is weak compared to the background, i.e.,

$$I_d(x,y) \ll I_b. \quad (4.9)$$

Moreover we suppose that there is a point  $(x_0, y_0)$  on the surface whose tangent is perpendicular to the image axis. This yields  $\theta(x_0, y_0) = 0$  and hence

$$\max_{\substack{x=1,\dots,n \\ y=1,\dots,m}} (C'(x,y)) = 1. \quad (4.10)$$

This last assumption will be satisfied for almost any geometry of objects imaged.

First, we compute the averages  $r_1(y)$  and  $r_2(x)$  of each column and row of  $I_r$ , respectively, i.e.,

$$r_1(y) := \frac{1}{n} \sum_{x=1}^n I_r(x,y), \quad r_2(x) = \frac{1}{m} \sum_{y=1}^m I_r(x,y).$$

We will verify in the following that - under the above assumptions - the term

$$E(x,y) := \frac{r_1(y) \cdot r_2(x)}{\max_{y=1,\dots,m} (r_1(y)) \cdot \max_{x=1,\dots,n} (r_2(x))} \quad (4.11)$$

approximates the curvature term  $C'(x,y)$ .

To derive  $E(x,y) \approx C'(x,y)$ , we first try to estimate the denominator of  $E$ . The maximum of  $r_l$  is

$$\max_{y=1,\dots,m} (r_1(y)) = \max_{y=1,\dots,m} \left( \frac{1}{n} \sum_{x=1}^n C'(x,y) I_b + \frac{1}{n} \sum_{x=1}^n C'(x,y) I_d(x,y) \right). \quad (4.12)$$

By using  $0 \leq C'(x,y) \leq 1$  and  $\Gamma_d(x,y) \ll \Gamma_b$ , the term  $\frac{1}{n} \sum_{x=1}^n C'(x,y) \Gamma_d(x,y)$  is negligible in (4.12), and we can estimate  $\max_{y=1,\dots,m} (r_1(y)) \approx \Gamma_b \cdot \max_{y=1,\dots,m} (\frac{1}{n} \sum_{x=1}^n C'(x,y))$ . Due to (4.8), this finally yields

$$\max_{y=1,\dots,m} (r_1(y)) \approx \Gamma_b \cdot \frac{1}{n} \sum_{x=1}^n C_1(x) \cdot \max_{y=1,\dots,m} (C_2(y)). \quad (4.13)$$

Analogously, we obtain

$$\max_{x=1,\dots,n} (r_2(x)) \approx \Gamma_b \cdot \frac{1}{m} \sum_{y=1}^m C_2(y) \cdot \max_{x=1,\dots,n} (C_1(x)). \quad (4.14)$$

Due to (4.8) and (4.10), we have  $1 = \max_{\substack{x=1,\dots,n \\ y=1,\dots,m}} (C'(x,y)) \approx \max_{y=1,\dots,m} (C_1(y)) \cdot \max_{x=1,\dots,n} (C_2(x))$ ,

and (4.13) and (4.14) then yields that the denominator of  $E(x,y)$  is approximately given by

$$\Gamma_b \cdot \Gamma_b \cdot \frac{1}{n} \sum_{x=1}^n C_1(x) \cdot \frac{1}{m} \sum_{y=1}^m C_2(y). \quad (4.15)$$

The numerator

$$r_1(y) \cdot r_2(x) = \frac{1}{n} \sum_{x'=1}^n (C'(x',y) \cdot (\Gamma_b + \Gamma_d(x',y))) \cdot \frac{1}{m} \sum_{y'=1}^m (C'(x,y') \cdot (\Gamma_b + \Gamma_d(x,y')))$$

can be expanded such that

$$r_1(y) \cdot r_2(x) = \frac{1}{n} \cdot \frac{1}{m} \sum_{\substack{x'=1 \\ y'=1}}^{n,m} C'(x',y) \cdot \Gamma_b \cdot C'(x,y') \cdot \Gamma_b + T(x,y),$$

where  $T$  captures the missing terms. The assumption (4.9) implies

$$\frac{\Gamma_d(x,y)}{\Gamma_b} = \frac{I_d(x,y)}{I_b} \approx 0 \text{ which yields } \frac{T(x,y)}{\Gamma_b \Gamma_b} \approx 0. \text{ This leads to}$$

$$\frac{r_1(y) \cdot r_2(x)}{\Gamma_b \cdot \Gamma_b} \approx \frac{1}{n} \cdot \frac{1}{m} \sum_{\substack{x'=1 \\ y'=1}}^{n,m} C'(x',y) \cdot C'(x,y') \approx \frac{1}{n} \cdot \frac{1}{m} \sum_{\substack{x'=1 \\ y'=1}}^{n,m} C_1(x') \cdot C_2(y) \cdot C_1(x) \cdot C_2(y'),$$

where we have used (4.4). By combining this with (4.7) and (4.11), we obtain

$$E(x,y) \approx \frac{C_1(x) \cdot C_2(y) \cdot \frac{1}{n} \sum_{x=1}^n C_1(x) \cdot \frac{1}{m} \sum_{y=1}^m C_2(y)}{\frac{1}{n} \sum_{x=1}^n C_1(x) \cdot \frac{1}{m} \sum_{y=1}^m C_2(y)} = C_1(x) \cdot C_2(y) \approx C'(x,y). \quad (4.16)$$

We can now divide  $I_r$  by  $E$  which gives us the desired

$$\frac{I_r(x,y)}{E(x,y)} \approx I'_b + I'_d(x,y). \quad (4.17)$$

The retrieved intensity  $I_e = I'_b + I'_d$  is the emitted intensity at the focal distance  $h$ . If different distances are used for multiple samples, one must further calibrate for the  $h^2$  component of  $C(x,y)$ .

A drawback of the above approach is its limitation to curvature terms  $C'(x,y) \approx C_1(x) \cdot C_2(y)$ . This condition is violated as soon as the sample has an unknown / complex geometry.

#### 4.4.1.2 Generalized geometries

To circumvent the limitation of having a known geometry, we have developed a second numerical method that is based on iterative polynomial fitting of the intensity image. We skip assumption (4.8), but we keep (4.9) and (4.10). Removal of the data signal  $I'_d(x,y)$  to retrieve  $C'(x,y) \cdot I'_b$  is done by local smoothing. A polynomial function is fitted for each row and each column in the image  $I_r$  using the polyfit function in MATLAB (Math Works, Natick, MA).

The polynomial function is fitted for each row ,

$$p_x(y) = p_{x,\alpha}y^\alpha + p_{x,\alpha-1}y^{\alpha-1} + \dots + p_{x,1}y^1 + p_{x,0} \quad x \in \{1, \dots, n\}$$

and each column

$$q_y(x) = q_{y,\beta}x^\beta + q_{y,\beta-1}x^{\beta-1} + \dots + q_{y,1}x^1 + q_{y,0} \quad y \in \{1, \dots, m\}$$

where  $\alpha$  and  $\beta$  are the polynomial orders. This results in two surface fits of the image. We expect that the spatial average of these 2D fits gives the first approximation  $[C'(x,y) \cdot I'_b]^1$  of the background modulated by the curvature, i.e.,

$$[C'(x,y) \cdot I'_b]^1 := \frac{p_x(y) + q_y(x)}{2}. \quad (4.18)$$

The first fit of the curvature  $C'(x,y) \cdot I'_b$  provides a reasonable resemblance of the object's surface, but is still an approximation. In the presence of a spatially varying data signal, the first fit of the curvature will not be smooth. Considering Equation (4.18) as being a function of the image,

$$[C'(x,y) \cdot I'_b]^1 = f(I_r) \quad (4.19)$$

we may iterate the curvature fit, using

$$[C'(x,y) \cdot I'_b]^k := f\left([C'(x,y) \cdot I'_b]^{k-1}\right) \quad (4.20)$$

where  $k$  is the number of iterations. Performing this iterative fitting will smooth the curvature fit and eliminate distortions which might be present in the first fit.

The choice of fitting function used is based on the geometry of the object. Here we are considering a forearm and will show in the results section that a fifth order polynomial in horizontal and vertical direction fits the data best and that six iterations were sufficient for the fitting procedure. For consistency, we have used these fitting parameters for all results.

Due to (4.9) and (4.10), the maximum of  $I_r$  is essentially given by

$$\max_{\substack{x=1,\dots,n \\ y=1,\dots,m}} (I_r(x,y)) \approx I'_b \cdot \max_{\substack{x=1,\dots,n \\ y=1,\dots,m}} (C'(x,y)) = I'_b.$$

By assuming that  $[C'(x,y) \cdot I'_b]^k \approx C'(x,y) \cdot I'_b$ , for  $k = 6$ , we can compute

$$\frac{[C'(x,y) \cdot I'_b]^k}{\max_{\substack{x=1,\dots,n \\ y=1,\dots,m}} (I_r(x,y))} \approx \frac{C'(x,y) \cdot I'_b}{I'_b} = C'(x,y). \quad (4.21)$$

The constraint of this method lies in the choice of the fitting function used. Care must be taken that the spatial frequency of the fitting function chosen is lower than that of the signal, or in other words, that the fitting function used does not fit the data. Otherwise the fitting function used will fit and remove the data content as well. This curve fitting method was evaluated using the numerical simulation, experimental phantom, as well as *in vivo* data.

#### 4.4.2 Numerical Simulation

A data wave was placed on a 50mm radius cylinder with a distance of 400mm away from the detection plane. To test the theory we used a background (or average) intensity of unit value and applied to it a sine grating signal of amplitude 1% of the background. We tested and compared three approaches, the approach where we have a measured surface (exact kernel), the averaging approach and fitting model. We used equation 4.6 to create the cylindrical numerical object and the exact kernel deconvolution inverts equation 4.6 to extract the emitted intensity,  $I_e(x,y)$ , with all variables known. The exact kernel is used as a gold standard to compare the averaging

and curve fitting method to, and is equivalent to having a separate system to measure shape.

As no imaging technique is free of noise, we evaluated the performance of our curvature correction method in presents of noise. Noise is defined as average white Gaussian noise applied to the final signal (background plus data wave modulated onto the cylinder) with magnitude determined as a percentage of the original data wave.

#### 4.4.3 Phantom Experiments

We used a cylindrical tube embedded in blue paper and flat blue paper, which will be referred to as cylindrical phantom and flat phantom, respectively. The blue paper used was regular office paper and several layers of paper were used to avoid any reflected light from the underlying tube. The diameter of the cylinder was 74mm. Structures were introduced by imprinting shaped objects (letters) on the phantoms. We used pencil, black, and red permanent markers, which will be referred to as contrast agents. Different contrast agents result into different data to background (DC component) ratios ( $I_d/I_b$ ). For these experiments, optical properties of the paper and contract agents were not known and not relevant. In order to experimentally test the curvature correction approaches, the quantity to change was the ratio of data to background ( $I_d/I_b$ ). In order to calculate the ratio, we imaged the flat phantom with the same letters imprinted and evaluated the data signal ( $I_d$ ) and the background signal ( $I_b$ ) by the following equations.

$$I_d = \frac{\max(I_e(x, y)) - \min(I_e(x, y))}{2} \quad (4.22)$$

$$I_b = \frac{\max(I_e(x, y)) + \min(I_e(x, y))}{2} \quad (4.23)$$

The ratios ( $I_d/I_b$ ) for the different contrast agents at wavelength 800nm were 0.73 (black marker), 0.51 (red marker), and 0.39 (pencil).

#### 4.4.4 In Vivo Experiments

Multi-spectral images were taken on healthy volunteers' forearms. All subjects signed a consent form, which was approved by the Institutional Review Board (IRB) of the National Institutes of Health under the protocol 08-CH-0001.

## 4.5 Results

### 4.5.1 Numerical Simulation

In Figure 4.2, we show that in the case of a data wave in form of a sine grating (a), superimposed on a cylindrical shape object (created using Equation (4.6)), (b-i) without noise and (b-ii) with 50% noise, we can recover the data wave using any of the three considered approaches. These approaches are (c) exact kernel, (d) averaging and (e) curve fitting approach. (c-i to e-i) Show the deconvolution without noise, (c-ii to e-ii) show the deconvolution with noise. (ii) Shows that in the case of noise, all three models respond to noise in a qualitatively similar manner and allow reliable recovery of the data wave. The point-wise percentage error is shown in column (iii); it is the deconvolved data wave (ii) minus the data wave (a-i), divided by the data wave. Wherever the data wave is of zero value, the error goes to infinity (division by zero). Remarkably this shows that all three approaches perform qualitatively equivalently. In order to demonstrate that the response to noise of the three models is also quantitatively equivalent, we have taken a set of images over a noise range of 1 to 100% (data not shown). Results show that the average error is the same for all approaches over the entire noise range and stays around zero. The normalized standard deviation shows an equivalent linear trend for all three methods and goes from 0.03 at zero noise to 0.537 at 100% noise applied.

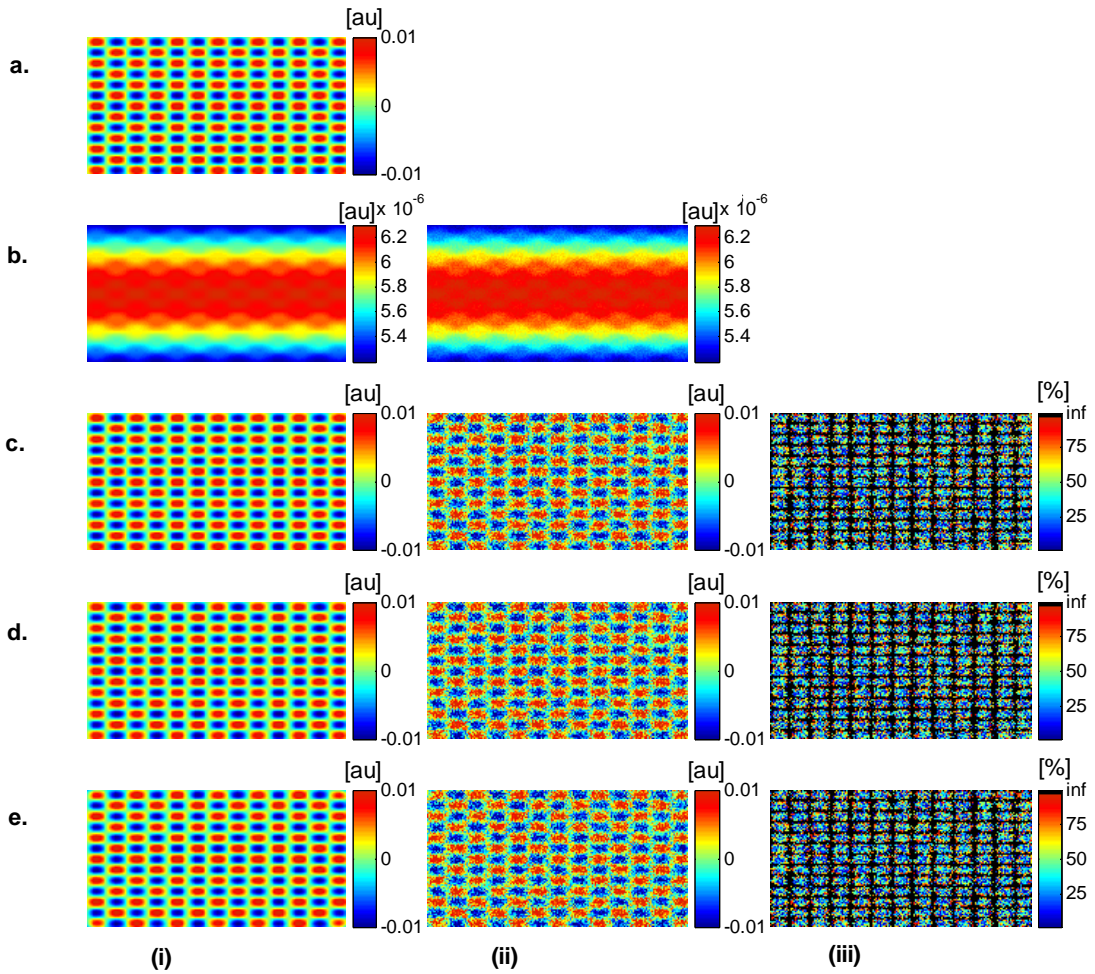


Figure 4.2 (a) Data wave (a sine grating), superimposed on (b – i) a cylindrical object without noise and (b – ii) with 50% noise. Three different approaches for curvature removal were tested, (c) exact kernel deconvolution, (d) horizontal and vertical averaging and (e) curve fitting. Qualitatively all three approaches perform equally well in the noise free scenario (i), as well as in the noise scenario (ii). The point-wise percentage error for the noise case is shown in column (iii).

In Figure 4.3a, we assess the dependence of the objects alignment relative to the horizontal or vertical image axis. The cylindrical numerical object was rotated 90 degrees in 5 degree steps and the error in reconstruction caused by this rotation was calculated. As expected, the averaging approach depends on the objects orientation, whereas the curve fitting approach does not. In Figure 4.3b, we show the effect of varying the radius of the cylinder, therefore the maximum angle theta, whilst holding the image size constant at 50mm, on the error on reconstructed data. The angles evaluated were 25 – 85 degree. The averaging method is not influenced by changes in angle, therefore changes in the curvature, and recovers the data wave accurately in all cases. The curve fitting method shows an exponential increase in error with increasing angles. At 85 degrees the error is 0.47, which is 47 times larger than the data wave. At angles greater 85 degrees the curve fitting approach brakes down and shows a dependence on

sampling accuracy. The exponential increase in error can be explained by the fact that a polynomial function cannot fit a cylinder. When excluding high angles ( $> 35$  degree), therefore only taking a fraction of the cylinder into account, the curve fitting method performs well, with an error smaller than the data wave. For all other numerical simulation results, a radius of 50mm (30 degrees) was used where the error is much smaller than the data wave ( $2.6 \times 10^{-4}$ ).

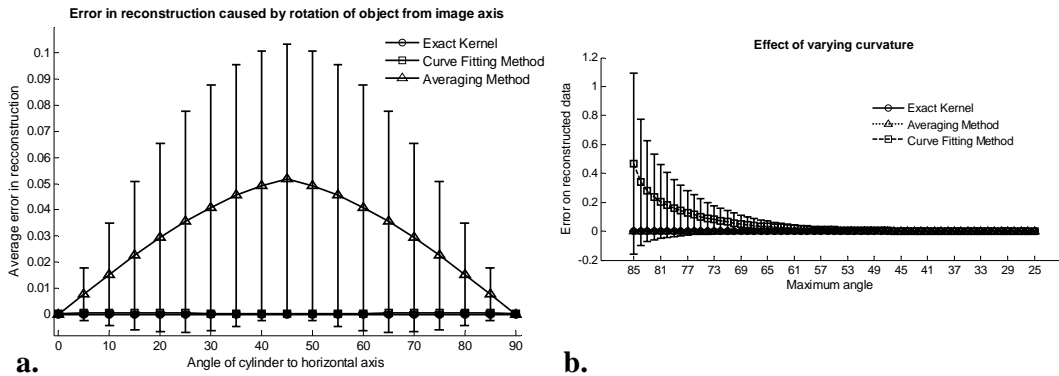


Figure 4.3 (a) Error in reconstruction caused by rotation of object from image axis. The cylindrical object was rotated 90 degrees, in 5 degree steps. The average error in reconstruction is plotted against the angle of rotation for all three methods. The averaging method highly depends on the orientation of the objects axis to the image axis, whereas the curve fitting method does not. (b) Error due to varying curvature. Changes in the radius, therefore maximum angle of the cylinder were evaluated. The error displayed has units of the data signal, which is of the order of 0.01. The curve fitting method shows an error greater than the data for angles between 85 and 35 degree and brakes down at angles  $> 85$  degree. At angles smaller than 35 degrees, the error is smaller than the data signal. The averaging method is not affected by the angle.

In Figure 4.4a, we illustrate a potential limitation of the curve fitting approach. Two columns of images are shown, the left column being the target data wave and the right being the deconvolved data wave. Here we have reduced the spatial frequency (top to bottom) of our sine grating gradually towards a point where the polynomial function used for fitting begins to fit the data wave. In this degenerative case we know that the model will not hold. This is expected, but as asserted, such cases should not occur in typical biological samples, which will be demonstrated in the *in vivo* result section. In figure 4.4b we provide a quantitative analysis of this effect. The average error in reconstruction is plotted against the number of cycles of the sine grating in the data wave. With increasing number of cycles, or spatial frequency, the error in reconstruction for the curve fitting method decreases. As expected, the averaging approach is not affected by the spatial frequency of the data wave.

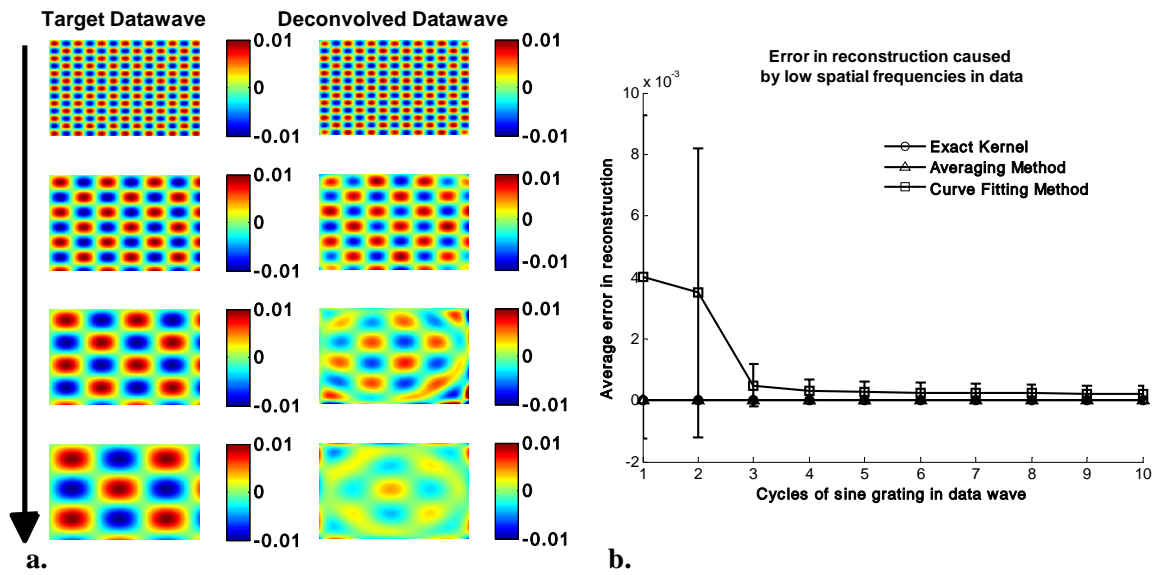


Figure 4.4 (a) Gradual degradation of the curvature correction using the curve fitting approach, when data with decreasing spatial frequencies (top to bottom) are applied. The left column shows the data waves and right column the deconvolved ones. (b) Error in reconstruction caused by low spatial frequencies in data. The dependence of spatial frequency of the data wave for the curve fitting approach is pointed out by plotting the average error in reconstruction against the number of cycles of the sine grating in the data wave. As expected, the averaging approach is not affected by the varying spatial frequency.

Figure 4.5 shows an assessment of our fundamental assumption that  $I_d \ll I_b$ . The percentage error in reconstruction is plotted against data to background ratio. Ratios evaluated were up to 1, where the data equals the background. Physiologically reasonable ratios, assessed by the *in vivo* results, were in the order of 0.15. As expected, the error increases with increased ratio for the curve fitting method. Whilst the  $I_d/I_b$  ratio is needed for the theoretical derivation, the averaging approach appears unaffected by the  $I_d/I_b$  ratio and performs equivalently to the known geometry model.

With the numerical simulation we have shown that all three approaches of extracting the curvature are equivalent, qualitatively and quantitatively, and can accurately recover the data wave. We showed the dependence of the results on noise and assessed the potential limitations of the numerical approaches.

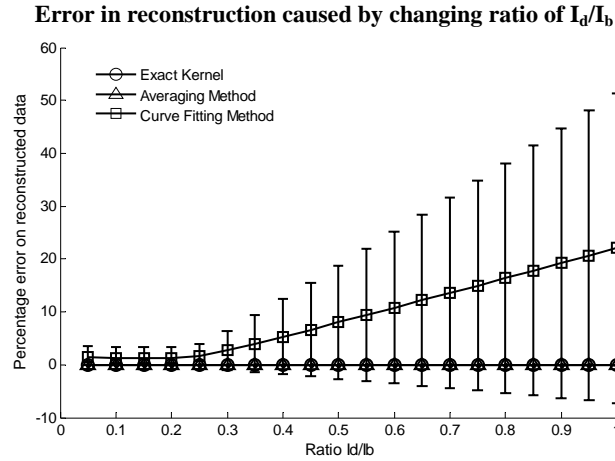


Figure 4.5 Error in reconstruction caused by increasing data to background signal level. The percentage error in reconstruction was plotted against the ratio of data to background ( $I_d/I_b$ ) for all three methods. (a) shows the percentage error for ratios up to 1 (data equals background) and (b) shows the same graph, but zoomed in to physiologically reasonable ratios. The error increases dramatically as the ratio goes to 1.

#### 4.5.2 Phantom Experiments

Multi-spectral images were acquired from a cylindrical and a flat phantom with the same optical properties. For illustrative purposes and conciseness, images will only be shown at one wavelength (800nm). We evaluated the curve fitting approach and we will illustrate the importance of adequate choice of polynomial order for fitting, the qualitative and quantitative recovery of the object shape, as well as the limitations of the algorithm with high background to data ratio.

In Figure 4.6 we show the effect of polynomial order on fitting quality. An averaged cross-section along the cylinder axis after correction can be seen (a). Polynomial orders two and three reduce the curvature effect but do not remove it completely at the edges. No significant difference can be seen between order five and six, which both remove the curvature accurately. Minor residuals (<2%) can be seen at the edges of the cylinder, which can be explained by the high angular dependence of the objects shape at the edges as well as by the fitting function used. A polynomial function cannot fit a circle and breaks down at the edges. We generated L-curves in order to make a decision of the best choice of polynomial order for fitting. The normalized standard deviation of all six wavelengths images, after correction for each polynomial order, was calculated. The standard deviation for each L curve was normalized against the maximum standard deviation for each wavelength and the dependence of standard

deviation on the polynomial order can be seen in Figure 4.6b. Based on these L-curves we chose fifth order polynomials for the curve fitting approach for our case.

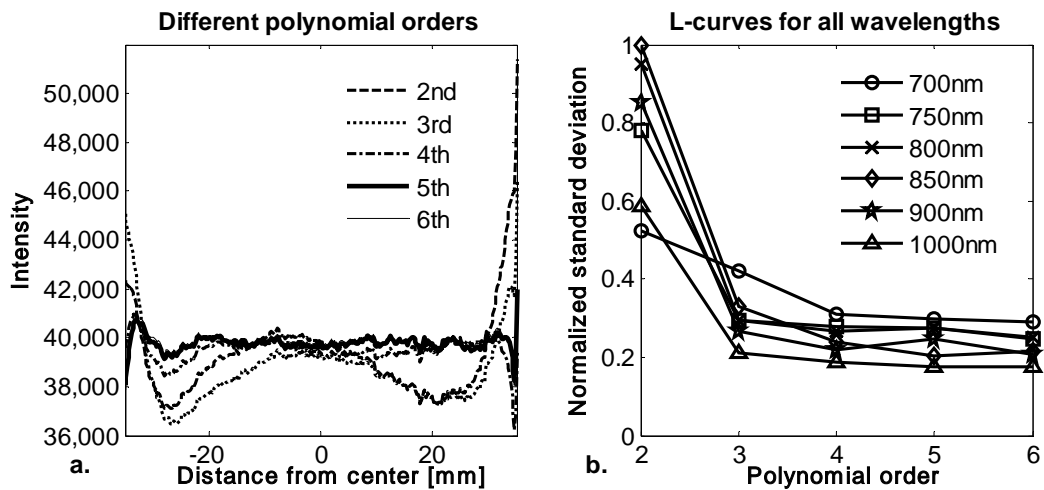


Figure 4.6 (a) Dependence of polynomial order on the fitting quality. The averaged, normalized cross-section through the cylinder (along y-axis) is plotted for each polynomial order tested. Order five and six fit the object shape accurately leaving only minor residuals ( $<2\%$ ) at the edges of the cylinder. (b) Shows the dependence of polynomial order on normalized standard deviation of the curvature corrected cylinder, illustrated by the L-curves.

Figure 4.7 shows the cylindrical phantom (a) before and (b) after curvature correction with the curve fitting approach in comparison to (c) the flat phantom. We demonstrate that our algorithm is capable of removing the curvature effect qualitatively in the comparison of Figures 4.7b and 4.7c. In Figure 4.7d we illustrate this recovery quantitatively by showing the averaged cross section for (a-c) with error-bars given by the standard deviation over all rows. The mean intensities over the entire image area are  $68105 \pm 997$  and  $65930 \pm 1095$  for the curvature corrected and the flat phantom respectively. Values are greater than the saturation limit of the 16bit camera due to calibration for spectral inhomogeneities [Vogel et al., 2007] and due to the curvature correction. Remaining discrepancies between these numbers may be explained by the fact that we used a cylindrical phantom, which cannot be fitted perfectly by a polynomial function. In comparison, the uncorrected phantom mean intensity is  $55022 \pm 15760$ . We therefore show that real intensity values can be recovered within 1.2% error, which is in comparison to 16.5% error before correction

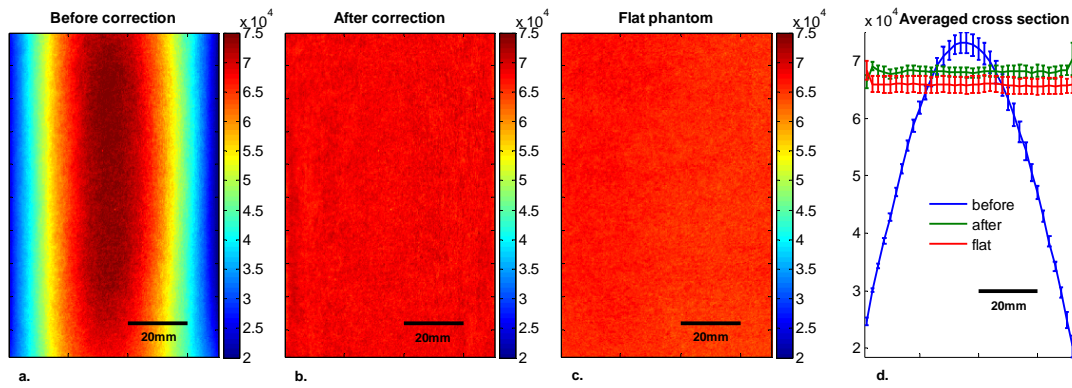


Figure 4.7 The curvature correction based on curve fitting on the cylindrical phantom without data content and compared to the flat phantom. (a) Shows the curvature uncorrected intensity image, (b) the curvature corrected intensity image, and (c) shows the flat phantom. (d) shows the averaged cross section of (a-c) with errorbars given by the standard deviation over all rows.

Figure 4.8 shows the cylindrical phantom with different contrast agents, having decreasing data to background ratios (a-c). The contrast agents used have different absorption coefficients compared to the background and were therefore used to mimic local changes, which are present for *in vivo* imaging (vein, hair, lesion, etc.). Different contrast agents were used in order to see the effect of contrast on the curvature correction. The method used for correction was based on the curve fitting approach. Letters were written perpendicular to the axis of curvature (i and ii) and along it (iii and iv) in order to assess the effect of structure orientation on the curvature correction. Figure 4.8a shows that for the highest  $I_d/I_b$  ratio (black marker), the least effective curvature correction is achieved. From left to right, Figure 4.8a shows the phantom (i) before correction and (ii) after correction for letters aligned perpendicular to the curvature, (iii) before and (iv) after correction for letters aligned along the curvature. After correction, remaining curvature is clearly visible in the image area where the letters are written, regardless of orientation. In this case the  $I_d/I_b$  ratio was 0.73 (calculated using equations 4.22 and 4.23), which is a much higher ratio than physiological changes found in typical biological samples. Qualitative improvement can be seen in Figure 4.8b and 4.8c (ratios 0.51 (red marker) and 0.39 (pencil) respectively), where the algorithm works better, as the ratio decreases.

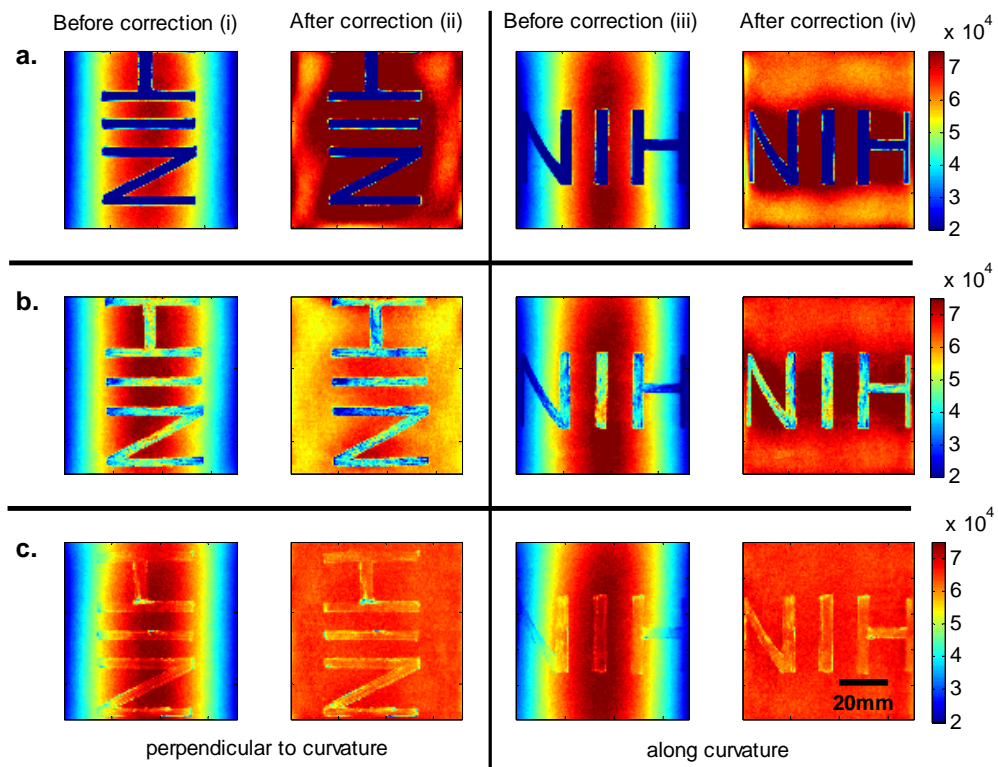


Figure 4.8 The curvature correction based on curve fitting on the cylindrical phantom with data (letters). Intensity images are shown before (i and iii) and after (ii and iv) curvature correction. Different contrast agents were used, with decreasing data to background ratios. The different  $I_d/I_b$  ratios are (a) 0.73, (b) 0.51 and (c) 0.39. The figure qualitatively shows the dependence of data to background ratio on the correction performance.

The quantitative relationship between the  $I_d/I_b$  ratio and the normalized standard deviation of the curvature corrected image is shown in Figure 4.9. For this comparison, the standard deviation of the background (no letters) was calculated after correction, as it is the background (no letters) which should be equivalent for all contrast agent images. Both cases of feature alignment were considered, perpendicular and along the curvature axis. The descending trend of standard deviation for decreasing ratios is found for both directions of feature alignment. Features which are aligned along the axis of curvature are less disruptive to the correction than features perpendicular to the curvature axis.

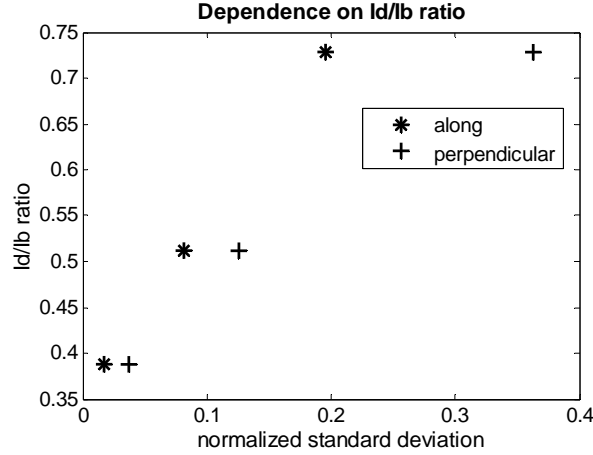


Figure 4.9 Dependence of contrast on the curvature correction. The  $I_d/I_b$  ratio is plotted against the normalized standard deviation of the background of the curvature corrected image at the wavelength of 800nm. Both cases of feature alignment are shown, as well as in comparison to the flat phantom without contrast agents.

The phantom experiments demonstrated that our algorithm does not only qualitatively remove the curvature, but provides quantitative agreement with flat objects with the same optical properties. We investigated the influence of data to background ratio on the correction efficiency and show that if the ratio is too high, the algorithm may not remove the curvature completely.

### 4.5.3 *In Vivo* Experiments

We evaluated the curve fitting curvature correction method described in the previous sections using *in vivo* images taken by our multi-spectral imaging system. Specifically, using images of a healthy volunteers lower arm, we will show the improvement in intensity image quality as well as on the reconstruction results for blood volume and oxygenation.

Figure 4.10 shows the effect of multiple iterations on the curvature fit, when using the curve fitting approach. Figure 4.10a shows a cross-section through the curvature fit with veins present. The locations of veins are pointed out by black arrows. The first fit of the curvature is clearly biased by intensity variations due to veins. This effect disappears with increasing numbers of iterations and the curvature becomes smooth. To quantify this behavior, the squared error of the difference between fits over increasing iterations was calculated, which can be assessed as:

$$E_n = \left( \left\langle C'(x, y) \cdot I_b' \right\rangle^{l-1} - \left\langle C'(x, y) \cdot I_b' \right\rangle^l \right)^2, \quad (4.24)$$

where  $l: 2 \rightarrow L$ , with  $L$  being the maximum number of iterations. The results of the squared error are shown in Figure 4.10b. Based on this L-curve, we have chosen six iterations for our curvature correction method.

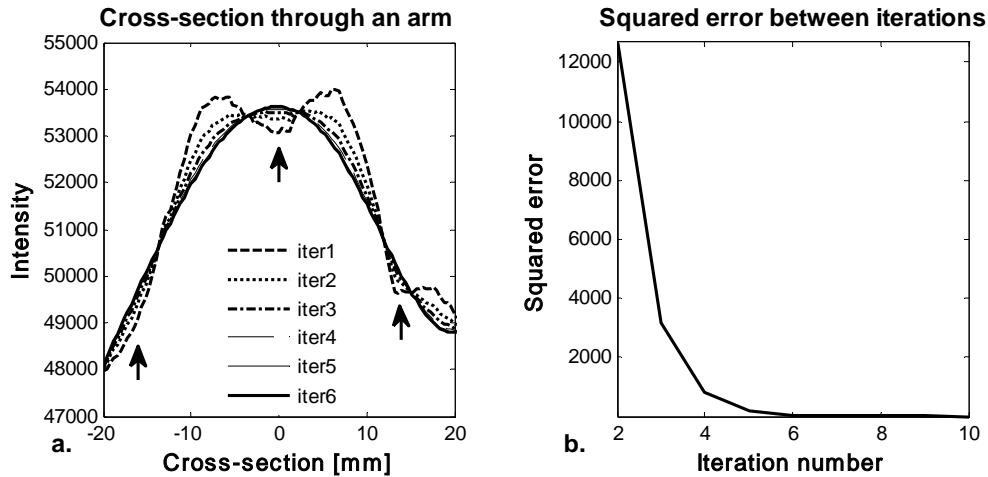


Figure 4.10 The effect of multiple iterations on the goodness of fit of curvature is shown in this graph. (a) Shows a cross-section through the curvature fit is shown for all six iterations. Black arrows indicate the location of veins. It can be seen that the effect of veins disappear after several iterations, leaving a smooth curvature. The L-curve (b) shows the squared error against number of iterations.

The qualitative improvement of image quality and feature extraction on intensity images for all six wavelengths acquired can be seen in Figure 4.11. Our method is able to recover real intensities and therefore spectral ratios are retained, which makes further analysis, i.e. reconstruction for blood volume and oxygenation, possible. The curvature corrected images in Figure 4.11 were used to evaluate the data to background ratios and to confirm that our assumption of  $I_d \ll I_b$  holds for our multi-spectral images. The data signal ( $I_d$ ) and the background signal ( $I_b$ ) were calculated by equations 4.22 and 4.23 using the curvature corrected images. We were confident using the corrected images for calculation, as the curvature effect is clearly larger than the data variation, as can best be seen in figure 4.12e and 4.12f (corrected vs. uncorrected). The ratios ( $I_d/I_b$ ) for all six wavelengths images were calculated and were 0.12 (700nm), 0.15 (750nm), 0.16 (800nm), 0.16 (850nm), 0.13 (900nm), and 0.09 (1000nm). Comparing these ratios to the results of the numerical simulation (Figure 4.5), a maximum error of 1.2% is expected in the removal of the curvature effect.

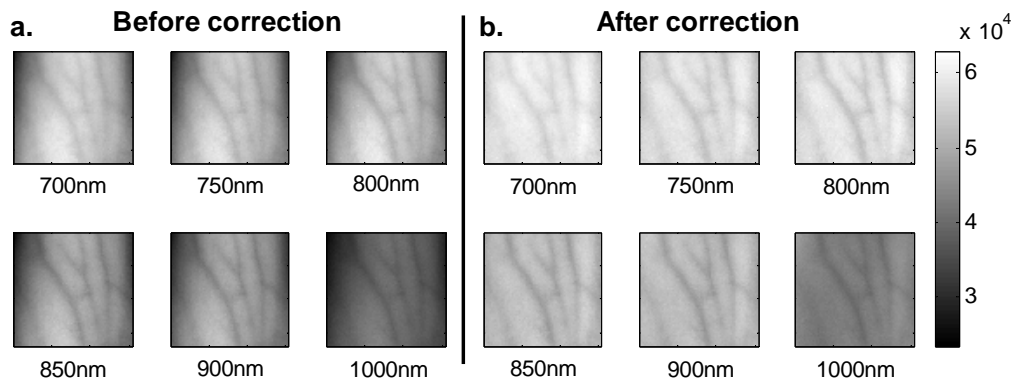


Figure 4.11 Curvature correction for *in vivo* data. Intensity images of a healthy volunteer's arm (a) before and (b) after correction are demonstrated for all six wavelengths. The qualitative enhancement in image quality can be seen in the corrected images.

To assess the improvement on skin chromophore concentration image reconstruction for blood volume and oxygenation was performed; representative results are shown in Figure 4.12. Reconstruction was performed on uncorrected intensity images and the corresponding curvature corrected ones in order to evaluate the curvature effect on reconstruction of chromophore distribution and concentration. Figure 4.12a and 4.12b show the reconstruction results for uncorrected images. Almost no structures can be identified, which is even more evident when looking at a cross section through the images, indicated by the dotted line in 4.12a and plotted in 4.12e and 4.12f. The curvature is clearly visible in both (a) blood oxygenation and (b) blood volume maps. The effect leads to overestimation of oxygenation in the center of the image and underestimation at the edges; the opposite effect is visible for blood volume. The curvature biases the reconstruction not only towards higher or lower chromophore concentrations, but obscures the structures in the sample imaged. Figure 4.12c and 4.12d show the results for curvature corrected images. The overall distribution of chromophore concentration is more uniform and not biased by the curvature anymore. A cross sectional comparison between uncorrected and corrected images can be seen in Figure 4.12e and 4.12f. With the curvature correction applied, pixel-wise assessment of chromophore concentration and detailed assessment of small structures was made possible.

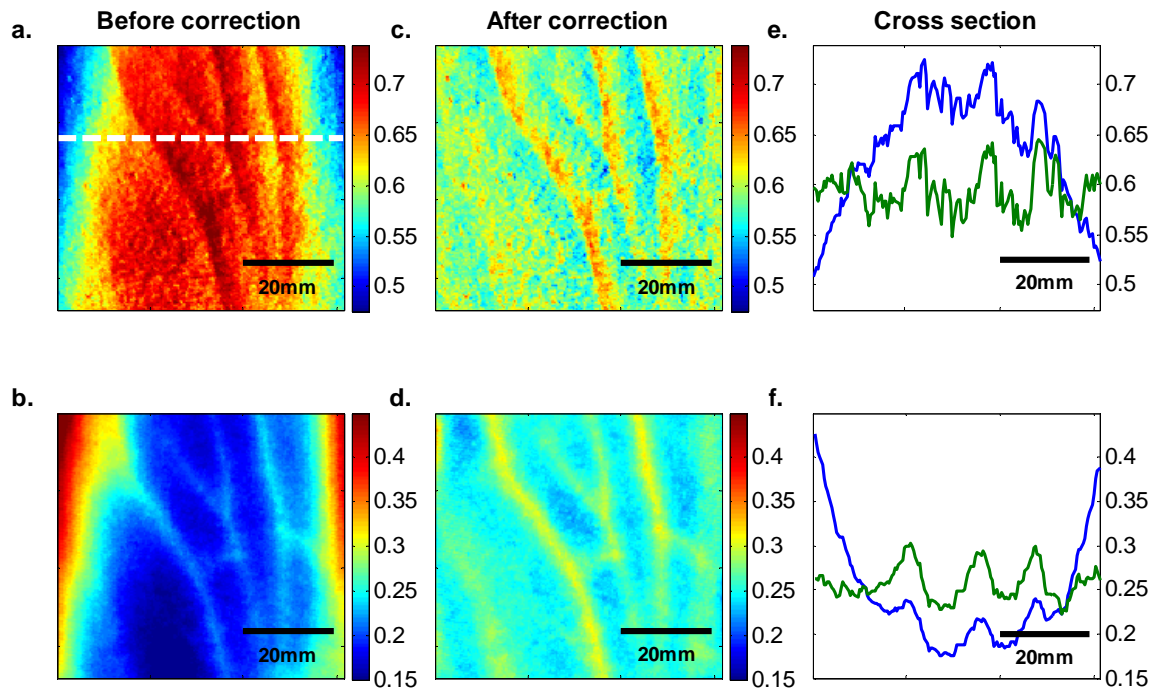


Figure 4.12 The effect of curvature correction on quantification of fraction blood oxygenation (a, c) and fraction blood volume (b, d). Reconstruction results before curvature correction (a, b) are clearly biased by it. Results after correction (c, d) don't show this effect, which can be seen in more detail in the cross sectional plots shown in (e, f – uncorrected in blue, corrected in green). The cross sections shown are indicated by the dotted line in (a). Detailed assessment of tissue chromophore concentration was made possible.

We demonstrated the qualitative improvement of curvature correction for multi-spectral images of *in vivo* data. The importance of correction becomes evident in the reconstruction results, where the curvature highly biases the spatial distribution of chromophore concentrations and makes pixel-wise assessment impossible. We further demonstrated that detailed feature extraction became possible, allowing assessment of structures over the entire image.

## 4.6 Discussion

Direct approaches to curvature correction in non-contact imaging allow us to remove the curvature artifact without extra measurements being required. We present two approaches that may be used in a complementary fashion depending on the imaging paradigm and sample imaged. The performance of the approaches depends on the objects images and the spatial extend of the data. Examples shown here shall therefore be seen as examples.

Numerical simulations allowed us to compare the two methods to an exact kernel deconvolution. The exact kernel is equivalent to measuring the geometry precisely with a secondary instrument, as such it provides a gold standard of the best possible result. We showed that the recovered signal is qualitatively (Figure 4.2) and quantitatively equivalent to the exact kernel. Figure 4.2 illustrates the images recovered from the two methods in the presence of noise, showing qualitative agreement to the exact kernel. We showed that over a range of noise up to 100% that the error in these images is numerically matched to that of the exact kernel. From these results we can assert that the two methods perform with the same quantitative performance as a separate measurement approach. This performance is demonstrated experimentally in Figure 4.7, where we recover the intensity value of a curved object to within 1.2% (average over the image); the average error in the uncorrected image is 16%.

The correction of the curvature is achieved by extracting information from the original intensity image. The information is the shape dependent bias in the image as described in equation 4.5. We extract this information by one of two methods, the first method is to use an x/y averaging algorithm. This method gives good qualitative and quantitative results as shown in figure 4.2. However it is limited by the assumption given in equation 4.8. This constrains us to images with simple geometries aligned to the imaging frame of reference. For the case of generalized geometries we have developed a curve fitting method as an alternative approach to extract the information. As illustrated in figure 4.3a, we see that the averaging method does indeed break down significantly with as little as 5% change in angular orientation to the imaging frame of reference. As expected, our generalized curve fitting model performs equivalently to the exact kernel through all orientations.

Having demonstrated the improvement of the generalized curve fitting approach over the averaging method, we now discuss the limitations of this approach where the

averaging approach may prove more suited to a given curvature correction problem. The first limitation is evidenced in figure 4.3b, where we see under areas of high curvature the curve fitting approach does not recover the background levels as accurately as an exact kernel, however the averaging approach is unaffected in this case. The second limitation of the curve fitting approach lies in the choice of the fitting function, which has to be chosen carefully, so that it fits the curvature of the object without fitting the spatially varying data signal. The curve fitting method rapidly degenerates both qualitatively (figure 4.4a) and quantitatively (Figure 4.4b) when the spatial frequencies are low. The averaging method is again not affected by such spatial frequency constraints (Figure 4.4b). Examples of physiological conditions, for which the described curve fitting method is suitable for, are port wine stains, body parts similar in structure, as described here, wounds, skin lesions, and others. The latter two are suitable conditions to study, if they are large compared to the image size and thus occupy most of the image. In general, the curve fitting method, with its parameter as chosen for this presented work, brakes down, if features in the image are of low spatial frequency. Examples of those cases could include nevi, lesions, if small compared to image size, and others. The final limitation of the curve fitting method is in the  $I_d/I_b$  ratio. Both methods require that  $I_d \ll I_b$  and the curvature extraction rapidly degenerates as  $|I_d| \rightarrow |I_b|$  (see figure 4.5); no such degeneration is seen for the averaging approach when using a sine grating as data wave.

For the case of Multi-Spectral imaging we wish to choose the most appropriate method. We know that these images may come from any part of the body and therefore the geometry may not be suitable to the averaging method, without rotation and image segmentation. This suggests the curve fitting approach would be more suitable, however we must first consider the other limitations. We know that the spatial variation of the chromophores is high, and that the images will not typically contain high curvature, however we must consider the ratio ( $I_d/I_b$ ). For our *in vivo* arm data, we found a maximum  $I_d/I_b$  ratio of 0.15, which corresponds to an expected error of 1.2% in recovered signal based on numerical simulation results (Figure 4.5). To further validate these numerical results we tested our imaging system on a cylindrical phantom with imprinted letters (Figure 4.8 & 4.9) to compare the error in recovery. The calculated  $I_d/I_b$  ratios were 0.73 (black marker), 0.51 (red marker), and 0.39 (pencil). A maximum error of 40% was found for black permanent marker (highest ratio), which equates to the expected value from the numerical simulation results with the same ratio. We would

like to point out, that the phantom experiments with blue paper were not aimed towards mimicking optical properties, rather than mimicking intensity ratios present when different structures with different optical properties are present in the area to be imaged. Due to this, we were able to use paper and markers, which do not have comparable optical properties, but do have comparable intensity ratios. For interested readers, we suggest to use equations (4.22) and (4.23) for calculating  $I_d/I_b$  and for putting their work in the same context.

*In vivo* results demonstrated the importance of curvature correction on identifying underlying tissue structures in the intensity images (Figure 4.11) and consequently in the reconstructed blood volume and oxygenation maps (Figure 4.12). Whilst the accurate concentrations are unknown due to the lack of a control measurement, the curvature effect in the raw images causes distortions in reconstructed maps, leading to physiologically unreasonable over- and underestimation of chromophore concentration. After curvature correction, the chromophore concentrations are more uniform, except for areas of different physiology (veins). We demonstrated that the overall spatial distribution is improved over the uncorrected reconstruction results. Pixel wise comparison between areas was made possible.

## 4.7 Conclusion

We introduced a direct, robust, rapid and elegant methodology to correct for curvature artifacts present in many non-contact optical imaging modalities. The method is based on analysis of raw intensity images by one of two algorithms, either averaging or curve fitting, and does not require any additional measurements of the shape. As no additional data is required, an attractive feature of the method is that already acquired data can be curvature corrected and reanalyzed. The effectiveness of our technique was demonstrated on numerical simulations, phantom experiments and *in vivo* data acquired from forearms, using multi-spectral imaging. We evaluated both algorithms in the presence of noise, for different angles of sample orientation, for varying curvature, and for varying data signal, either varying in spatial frequency or contrast. Results showed that the curvature removal does not bias the recovered signal. They also demonstrated that the curve fitting approach is better for generalized geometries. However, care must be taken regarding degree of curvature, spatial frequency and data to background

intensity ratios, if this approach is to be chosen over the averaging algorithm. Furthermore, results from phantom experiments showed that real intensity values can be recovered and objects with same optical properties but different shape can be directly and pixel wise compared. Based on the numerical simulation results, we found that in the case of *in vivo* arm data, a maximum error of less than 2% can be expected in the recovery of the signal. We demonstrated the curve fitting approach on *in vivo* data of the arm for intensity images as well as for reconstruction results of blood volume and oxygenation and showed the importance of taking the curvature into account if pixel wise assessment of skin chromophores is desired.

**Acknowledgement:** The research was funded by the Intramural Research Program of the Eunice Kennedy Shriver National Institute of Child Health and Human Development. The Graduate Partnership Program at the National Institutes of Health and the Department of Physics at the University of Vienna in Austria are also acknowledged.



## **Chapter 5**

# **Interlude 1 – Importance of curvature correction for Principal Component Analysis**

### **5.1 Introduction**

In the previous chapter it was shown that the shape of the object influences the intensity distribution in reflectance images. This artifact has to be removed before reconstruction of blood volume and oxygenation; otherwise, the reconstructed results will reflect curvature rather than chromophores. The curvature distribution is thus the strongest component in the data and masks the physiological information.

Since we showed that the curvature information can be separated and removed, it is independent from physiological information. Given this independence, the idea of separating it based on independence measures springs to mind. Here we are showing briefly the idea of extracting the curvature based on Principal Component Analysis (PCA), which is a tool for finding linear independent components, described by eigenvectors in the data. We show that the first eigenvector indeed correlates with curvature, but does not remove it completely.

Additionally it was found that when removing the curvature in the images based on curve fitting and applying PCA to those, a resemblance of blood volume and oxygenation could be found. This resemblance led to further investigations and the findings described in chapter 6. PCA applied to multi-spectral data for extracting skin chromophores will be described in detail in chapter 6.

### **5.2 Principal Component Analysis**

Principal Component Analysis extracts the primary components in the data by linearly transforming it onto an orthogonal coordinate system, where the axes correspond to the principal components in the data, which are the eigenvector of the data. Through an eigenanalysis, the principal components are determined as

eigenvectors of the dataset's covariance matrix and the corresponding eigenvalues refer to the variance that is captured within each eigenvector.

Here PCA was employed as a tool for curvature extraction. We use three wavelengths (750, 800, 850nm) images taken from a healthy volunteer's lower forearm. The three 2D images are first transformed into vectors, the mean is being subtracted, and the covariance matrix calculated and diagonalized:

$$Cov(X) = E(XX^T), \quad (5.1)$$

where  $X = (x_1, \dots, x_n)$  is the zero mean data matrix with pixel vectors  $\{x_1, \dots, x_n\}$ . The three eigenvectors  $p_1, p_2, p_3$  - the principal components ordered according to the magnitude of their eigenvalues - provide the transformed data

$$Y = W^T X, \quad (5.2)$$

where  $W = (p_1 \ p_2 \ p_3)$ . Rearranging the vectors in  $Y$  into matrices yields again three 2D images. The first image represents the projected data along the first eigenvector, which is hypothesized to correspond to curvature.

### 5.3 PCA on raw images

Intensity distributions of a healthy volunteer's lower forearm can be seen in figure 5.1 for 750nm, 800nm, and 850nm. The images shown are not curvature corrected, thus showing the shape of the arm in the intensity distributions. Applying PCA to those images yields again three 2D images, which are the projection along the eigenvectors of the data. This projection can be seen in figure 5.2.

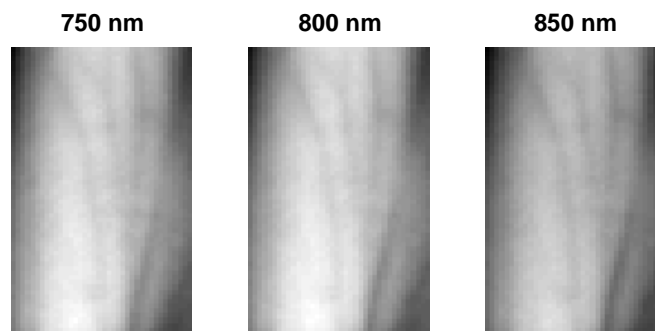


Figure 5.1 Intensity images of a healthy volunteer's lower forearm before curvature correction.

As hypothesized, eigenvector 1, which describes the component of the data with the most variance, primarily describes curvature. If PCA would be used as a dimension reduction technique, the bulk part of the curvature artifact could be removed.

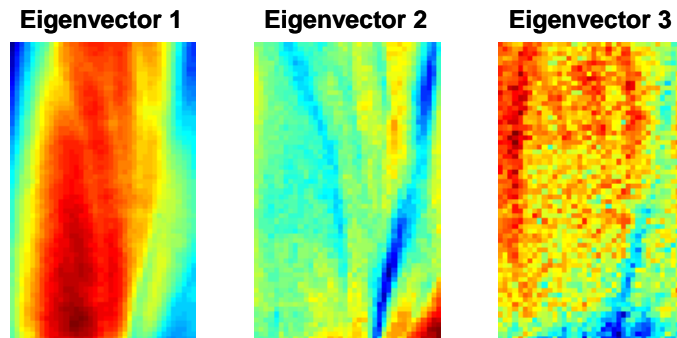


Figure 5.2 PCA results of the data shown in figure 5.1. Eigenvector 1 strongly correlates with curvature.

When looking at the images closely though, eigenvector 1 also contains structures, which correspond to vessels, thus does not uniquely describe curvature. Also, eigenvector 2 still contains curvature (right lower corner in the image). We thus dismissed PCA as an additional curvature removal technique. Interestingly though, eigenvector 2 primarily shows vessel structures, which spatially correspond to reconstructed blood volume (data not shown).

#### 5.4 PCA on curvature corrected images

Intensity images after curvature correction with curve fitting can be seen in figure 5.3. The curvature artifact is clearly removed and vessel structures became visible even at the edges of the images. Images are in the same scale as in figure 5.4.

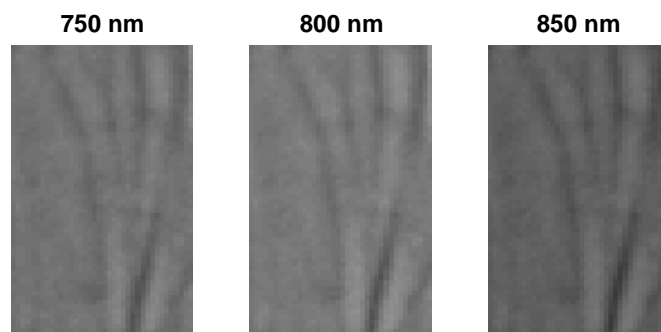


Figure 5.3 Intensity images of a healthy volunteer's lower forearm after curvature correction.

Results from applying PCA to those curvature corrected images can be seen in figure 5.4. Eigenvector 1 and 2 show spatial distributions which resemble reconstruction results of blood volume and oxygenation. No curvature artifact is visible, which is additional reassurance of the curvature removal algorithm removing the curvature information in the multi-spectral images.

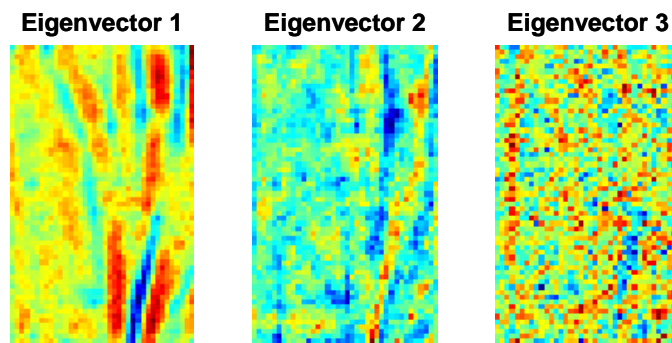


Figure 5.4 PCA results of the data shown in figure 5.3. No curvature artifact is visible. Eigenvector 1 and 2 show spatial distributions similar to blood volume and oxygenation.

The results of this first attempt to use PCA on multi-spectral images led to the work described in the following chapter 6. Since the spatial distributions of the PCA results very much reminds of blood volume and oxygenation distributions, the idea of using PCA for extracting those was investigated

## Chapter 6

# Original paper 2 – Principal Component Model of Multi Spectral Data for Near Real Time Skin Chromophore Mapping

### 6.1 Abstract

Multi-spectral images of skin contain information on the spatial distribution of biological chromophores, such as blood and melanin. From this, parameters such as blood volume and blood oxygenation can be retrieved using reconstruction algorithms. Most such approaches use some form of pixel-wise or volumetric reconstruction code. In this work we explore the use of Principal Component Analysis (PCA) of multi spectral images to access blood volume and blood oxygenation in near real time. We present data from healthy volunteers under arterial occlusion of the forearm, experiencing ischemia and reactive hyperemia. Using a two layered analytical skin model, we show reconstruction results of blood volume and oxygenation and compare it with the results obtained from our new spectral analysis based on Principal Component Analysis. We demonstrate that PCA applied to multi-spectral images gives near equivalent results for skin chromophore mapping and quantification with the advantage of being three orders of magnitude faster than the reconstruction algorithm.

### 6.2 Introduction

Assessing spatial distributions of skin chromophores such as blood and melanin can be achieved by diffuse multi-spectral imaging. Acquiring several wavelength images in the near infrared spectrum together with an analytical skin model, allows fitting the data to the model, thus extracting and mapping the spatial distribution of those parameters.

Diffuse multi spectral imaging of the skin and image reconstruction of skin chromophores has found its application in the clinic, successfully assessing parameters

for healthy and diseased skin [Jacques et al., 2002; Mantis & Zonios, 2009; Miyamae et al., 2008; Tseng et al., 2009; Vogel et al., 2007; Zakian et al., 2008; Attas et al., 2001]. Assessment of the metabolic state of skin surface lesions is often desired in clinical routines as a measure for treatment outcome. Near infrared diffuse multi-spectral imaging of the skin combined with an analytical, numerical, or stochastic skin model can provide this information by producing spatial maps of skin chromophore concentrations [Kainerstorfer et al., 2009a; Vogel et al., 2007; Vogel et al., 2006]. The main parameters of interest are blood, melanin, lipids, and water, which exhibit separable absorption coefficients in the near infrared wavelengths range. The disadvantage of finding these parameters by fitting the data to an analytical skin model lies in the computationally expensive data post processing. This makes immediate conclusions difficult or even impossible if the image size is large, whereas in clinical routines it is often desired to assess the metabolic state of a tumor in real time. We are not aware of any current imaging protocol and reconstruction algorithm which can assess quantitative blood concentrations in real time.

Principal Component Analysis (PCA), first introduced in 1901 [Pearson, 1901], is a statistical tool, which linearly transforms data into an orthogonal coordinate system, where the axes correspond to the inherent information within the data set. The idea is to reveal the data components (in a decreasing order) that best explain the variance in the data. PCA has found applications in fields such as face recognition [Moon & Phillips, 2001; Turk & Pentland, 1991], and image compression [Du & Fowler, 2008], and is a common technique for finding patterns in high dimensional data [Ferraz et al., 1998]. It is further used for analyzing and visualizing gene expression data [de Haan et al., 2007; Nishimura et al., 2003; Sghaier-Hammami et al., 2009], for dimension reduction in hyperspectral imaging [Begelman et al., 2009], as well as image enhancement [Mandelkow et al., 2010]. The main advantage of PCA is the speed of computation, which is in the order of seconds per image. For the biomedical optical imaging field, PCA found its place in various applications. The usage ranges from noise reduction and image enhancement [Mandelkow et al., 2010] in multi spectral data for biological cell analysis [Nuffer et al., 2006] to pattern analysis for skin lesion classification [She et al., 2007]. Applied to RGB images, PCA was used on relative color features for unsupervised lesion classification [Cheng et al., 2008; Hance et al., 1996; Umbaugh et al., 1993].

When imaging the skin in the visible light range, the dominant absorbing materials are blood and melanin and should therefore explain most of the variance in multi spectral data. Previous work by Tsumura et al. [Tsumura et al., 1999] showed that skin color in digital RGB images can be described by attributing melanin and blood to the first two principal components. Fadzil et al. [Fadzil et al., 2009; Nugroho et al., 2007] used the same idea and applied PCA and Independent Component Analysis (ICA) to RGB data for blood and melanin extraction of vitiligo lesions to qualitatively evaluate the skin repigmentation progression.

In this work we evaluate the use of Principal Component Analysis (PCA) for retrieving quantitative near real time blood volume and blood oxygenation maps of skin areas of several square centimeters from a selected set of spectral images in the near infrared range (700 – 1000nm). Our experimental protocol involves imaging of healthy volunteers' lower forearm before, during, and after arterial occlusion. Occlusion experiments were chosen, as the behavior of blood oxygenation is well known which is ischemia during and reactive hyperemia after release of pressure.

In the first part of the paper we describe the two layered analytical skin model used and show reconstruction results of blood volume and blood oxygenation over time. In the second part we apply PCA to the same data set and show that the first eigenvector correlates with blood volume and the second eigenvector with blood oxygenation. Finally we compare reconstruction results with the eigenvectors found by PCA and demonstrate the relationship between blood volume and the first eigenvector, as well as the relationship between blood oxygenation and the second eigenvector.

## **6.3 Materials**

### **6.3.1 Instrumentation**

The non-invasive, non-contact diffuse reflectance multi-spectral imaging system used in this work has been described in detail elsewhere [Vogel et al., 2007] and shall only be described briefly here. Polarized light from a white light source (halogen 150W) is used for illumination of the sample. A second polarizer is placed before the detection unit, with its polarization orientation perpendicular to the incident beam polarization,

thus guaranteeing diffuse reflectance measurements and removal of specular reflection [Demos & Alfano, 1997a].

Images are captured by a CCD camera (Princeton Instruments CCD-612-TKB, Roper Scientific) after passing consecutively one of six narrow bandpass filters (40nm FWHM, CVI Laser) on a filter wheel centered at 700, 750, 800, 850, 900 and 1000nm. For calibration purposes, images from a 90% reflectance paper (Kodak) are also acquired at each image filter.

### **6.3.2 Occlusion experiments on healthy volunteers**

A pressure cuff was used to occlude the upper right arm of five right handed healthy volunteers with 180mmHg pressure. This amount of pressure was chosen to achieve arterial occlusion and the pressure lasted for 5min. Multi-spectral images were taken every 30 seconds before occlusion, during occlusion and for 5 minutes afterwards, resulting in 21 time points in total. Occlusion experiments were chosen as the behavior of blood volume and blood oxygenation over time is well known, which is ischemia during, and reactive hyperemia after occlusion [Kainerstorfer et al., 2009a; Tseng et al., 2009; Cuccia et al., 2009; Merschbrock et al., 1994].

All volunteers signed a consent form approved by the Institutional Review Board of the Eunice Kennedy Shriver National Institute of Child Health and Human Development under the protocol number 08-CH-0001.

## **6.4 Methods**

### **6.4.1 Reconstruction of skin chromophores**

Diffuse multi-spectral images obtained during the occlusion experiment were used for reconstruction of blood volume and blood oxygenation. Preprocessing of the data included spectral and spatial illumination artifact removal as described in [Vogel et al., 2007]. The next step in preprocessing was rigid body registration for motion artifact removal and was performed by MultiStackReg in Image J. In a last step, curvature correction was performed to remove shape based intensity bias [Kainerstorfer et al., 2010a].

Four wavelength ( $\lambda$ ) images were used (700, 750, 800, and 850nm) and reconstruction was performed using MATLAB (Math Works, Natick, MA) by least squares non linear fitting of the data to the analytical skin model used [Vogel et al., 2007]. The analytical skin model is based on a two layered structure, the first one being the melanin containing epidermis, the second one being the blood containing dermis, with optical properties of the skin taken from literature values [Jacques, 1998; Meglinski & Matcher, 2002; Prahl, 1998], and can be written as:

$$I_e(\lambda) = S \cdot A_e(\lambda)^2 \cdot A_d(\lambda) \quad (6.1)$$

where  $I_e$  is the wavelength dependent intensity measured in the CCD camera. The attenuation by the epidermis,  $A_e$ , is based on Lambert's law and can be written as:

$$A_e(\lambda) = e^{-\mu_e d_e} = e^{-(v_m \cdot 0.66 \cdot 10^{11} \cdot \lambda^{-3.33} \cdot d_e)} \quad (6.2)$$

with  $v_m$  the concentration of melanin,  $d_e$  the thickness of the epidermis and  $\mu_e$  the absorption coefficient of the epidermis, which is based on the absorption of melanin. The attenuation by the dermis,  $A_d$ , which includes the absorption due to blood volume,  $v_{db}$ , and oxygenation,  $v_{boxy}$ , is based on the analytical solution of photon migration in turbid media [Gandjbakhche & Weiss, 1995a] based on random walk theory and can be written as:

$$A_d(\lambda) = \frac{e^{-2(\mu_d / \mu'_s)}}{\sqrt{24(\mu_d / \mu'_s)}} \cdot \left(1 - e^{-\sqrt{24(\mu_d / \mu'_s)}}\right) \approx 1.06 - 1.45 \cdot (\mu_d / \mu'_s)^{0.35}, \quad (6.3)$$

$$\mu_d = v_{db} \cdot \left[ (1 - v_{boxy}) \cdot \mu_{deoxy} + (v_{boxy}) \cdot \mu_{oxy} \right] \quad (6.4)$$

where  $\mu'_s$  is the reduced scattering coefficient and  $\mu_d$  is the absorption coefficient of the dermis, with  $\mu_{deoxy}$  and  $\mu_{oxy}$  being the absorption coefficients of deoxygenated and oxygenated blood respectively. The scaling factor S, blood volume,  $v_{db}$ , and blood oxygenation,  $v_{boxy}$ , are unknown a priori and were solved for.

The scaling factor was calculated for each subject and time point and averaged over time. This so obtained subject specific scaling factor was then used to compute the 2D maps of blood volume and oxygenation over the course of the experiment. Computational time for each 2D image, which is in the order of 200 x 200 pixels, was 45min on a 2.6GHz, 3GB RAM Personal Computer (PC).

#### 6.4.2 Principal Component Analysis

Principal Component Analysis [Pearson, 1901] linearly transforms the data into an orthogonal coordinate system whose axes correspond to the principal components in the data, i.e., the first principal component accounts for as much variance in the data as possible and, successively, further components capture the remaining variance. Through an eigenanalysis, the principal components are determined as eigenvectors of the dataset's covariance matrix and the corresponding eigenvalues refer to the variance that is captured within each eigenvector.

We use three wavelengths (750, 800, 850nm) from the occlusion experiment, which provides three 2D images. These wavelengths were chosen, as they are centered around 800nm, which is the isosbestic point of blood, where the absorption coefficient of deoxygenated (Hb) and oxygenated (HbO<sub>2</sub>) blood are equal. Fig. 6.1 shows the absorption spectra for Hb and HbO<sub>2</sub>, illustrating that the absorption of Hb is dominant at 750nm and for HbO<sub>2</sub> at 850nm. In this wavelength range, the dominant chromophore is blood and should therefore explain most of the variance of the data.

After subtracting the mean of the data, PCA was performed on the collection of three-dimensional pixel vectors  $\{x_1, \dots, x_n\}$  of the zero mean data. We first diagonalize the covariance matrix

$$Cov(X) = E(XX^T), \quad (6.5)$$

where  $X = (x_1, \dots, x_n)$  is the zero mean data matrix. The three eigenvectors  $p_1, p_2, p_3$  - the principal components ordered according to the magnitude of their eigenvalues - provide the transformed data

$$Y = W^T X, \quad (6.6)$$

where  $W = (p_1 \ p_2 \ p_3)$ . Rearranging the vectors in  $Y$  into matrices yields again three 2D images. The first image represents the projected data along the first eigenvector. As mentioned above, blood is the dominant chromophore, and it will turn out that the first layer correlates with blood volume. The second image is each datapoint's projection along the second eigenvector and we will show that it correlates with blood oxygenation.

The computational time to process one set of data (three images at 21 timepoints) on a 2.6GHz, 3GB RAM PC was in the order of 1 second.

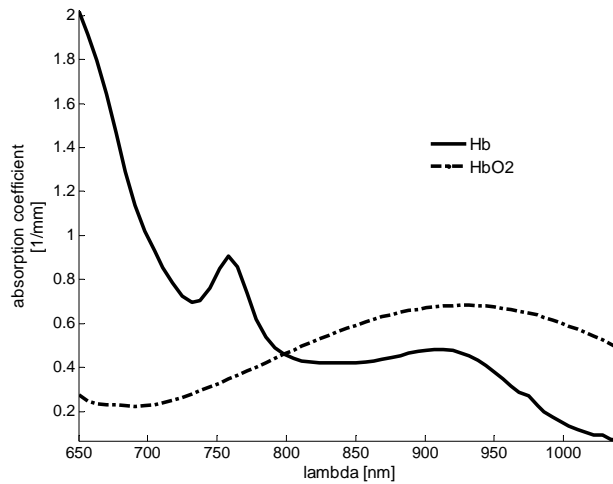


Figure 6.1 Absorption spectra of deoxygenated (Hb) and oxygenated (HbO<sub>2</sub>) blood with the isosbestic point of blood at 800nm. For 750nm and 850nm, the absorption coefficients for oxygenated and deoxygenated blood are well separable.

## 6.5 Results

In order to evaluate the potential of PCA to retrieve the spatial distribution of chromophores, we first generate a conventional pixel-wise reconstruction of blood volume and oxygenation over an imaging area of several centimeters. We then compare results after applying PCA to the contributions of the principal components. The objective was to demonstrate the anticipated response (ischemia and reactive hyperemia) for all subjects and a qualitative and quantitative assessment of the consistency between reconstruction results and the eigenvectors.

Fig. 6.2 shows 2D reconstruction maps of fractional blood volume concentrations over time for one representative healthy volunteer's lower forearm. Only every second time point is shown for conciseness, with the first row showing the baseline before occlusion, row 2 and 3 showing results during and after occlusion respectively. Veins contain more blood than the surrounding tissue and are clearly separable in the reconstruction maps by increased blood volume. Fig. 6.3 shows the corresponding blood oxygenation result over time, before, during, and after occlusion. Veins do not show a significant difference in blood oxygenation compared to surrounding tissue and can not be easily separated. The overall tissue oxygenation follows the typical expected trend of ischemia during occlusion (drop of oxygenation compared to baseline) and reactive hyperemia after occlusion (over shoot compared to baseline).

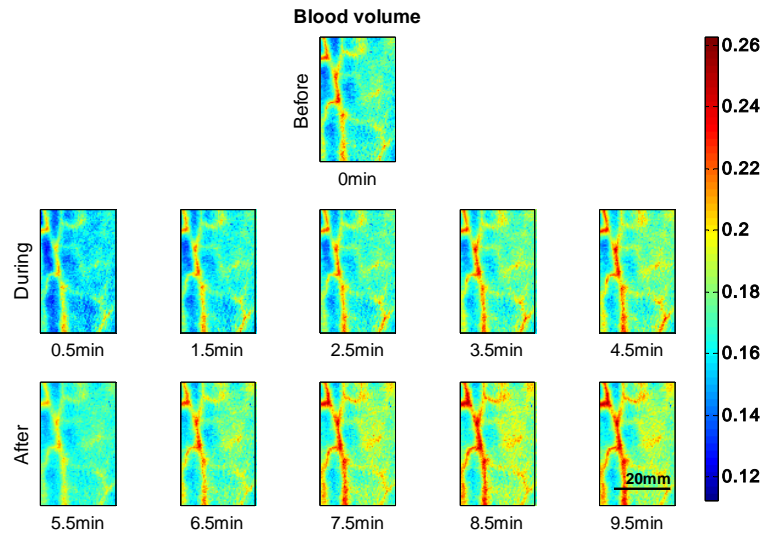


Figure 6.2 Fractional blood volume concentrations over time. The first row shows the reconstructed blood volume map over several centimeters of a lower forearm before occlusion. The second row shows blood volume of the same area of the arm during occlusion and the third row shows results after release of pressure. Veins are clearly distinguishable due to the increase in blood compared to surrounding tissue.

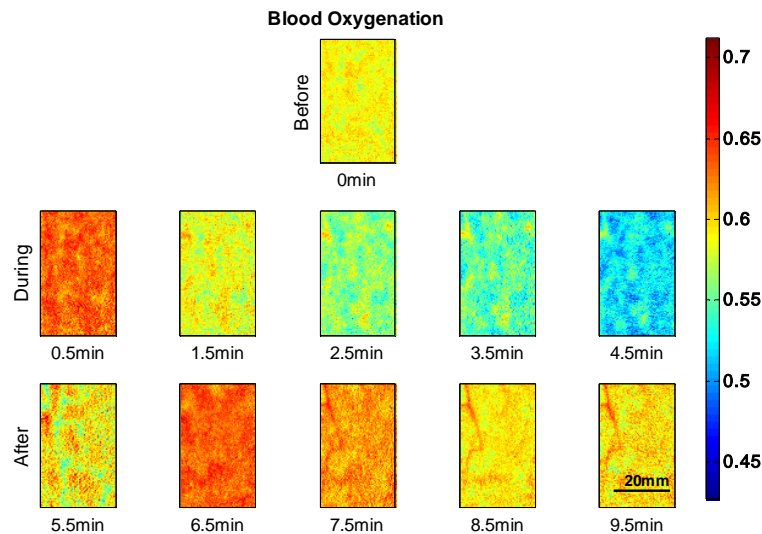


Figure 6.3 Fractional blood oxygenation over time of the same area as shown in figure 6.2. The second row shows blood oxygenation during occlusion and the expected ischemic behavior, which is a decrease in oxygenated blood. The third row shows the expected hyperemic behavior, which is an overshoot of oxygenation.

To evaluate the ischemic and hyperemic behavior even further, average concentrations of blood volume and oxygenation were calculated over the entire 2D maps for each time point. The results for four subjects can be seen in Fig. 6.4a for blood volume and 4b for blood oxygenation, with error-bars given by the standard deviation over all pixels per time point. Only four of the five subjects were included in the analysis, as the analysis of the fifth subject was hindered by motion artifacts greater

than one third of the image size. The dashed lines indicate the time points of beginning and ending of applied pressure. Fig. 6.4a shows that blood volume stays over time within 5% variation, while Fig. 6.4b shows changes in blood oxygenation over time, corresponding to ischemia during and reactive hyperemia after occlusion.

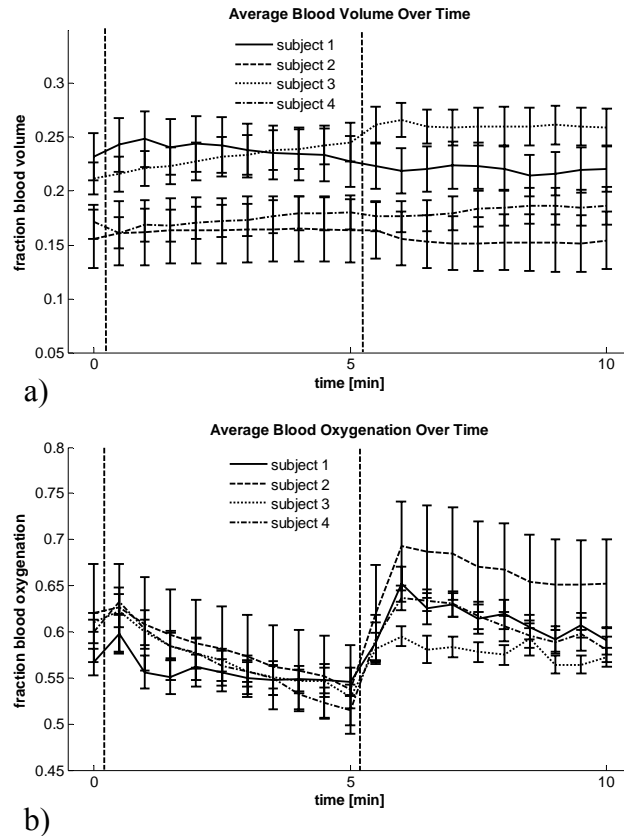


Figure 6.4 Average Blood Volume (6.4a) and Blood Oxygenation (6.4b) over time for four subjects. The dashed lines indicate start and end of occlusion.

Fig. 6.5 shows a set of three wavelength images (750, 800, 850nm), represented in a 3D scatter-plot in the wavelength space, with each pixel being color-coded by the reconstruction results of blood volume (Fig. 6.5a) and blood oxygenation (Fig. 6.5b). Data shown in this figure are from the same subject as in Fig. 6.2 and Fig. 6.3 at the 12<sup>th</sup> time point, which is the first point after occlusion. All other subjects and time points show a similar behavior, which can be summarized as following: a) the data is of elliptical distribution, indicating that it can be described by a linear transformation. b) The reconstruction values of blood volume lay along the main axis of the ellipse, which will be described as eigenvector 1 (vertical black line in Fig. 6.5a and Fig. 6.5b), and are well separable. c) The reconstruction results of blood oxygenation show a separation perpendicular to the main axis of the ellipse, which will be described as eigenvector 2

(horizontal black line in Fig. 6.5a and Fig. 6.5b). All three points combined indicate that a linear transform of the data by PCA is not only valid, but that it should be possible to separate blood volume and oxygenation. The separation between blood volume and oxygenation with PCA can only be possible, if alignment perpendicular to each other is given. This is an inherent necessity for PCA, since data is being described with eigenvectors, which are perpendicular to each other.

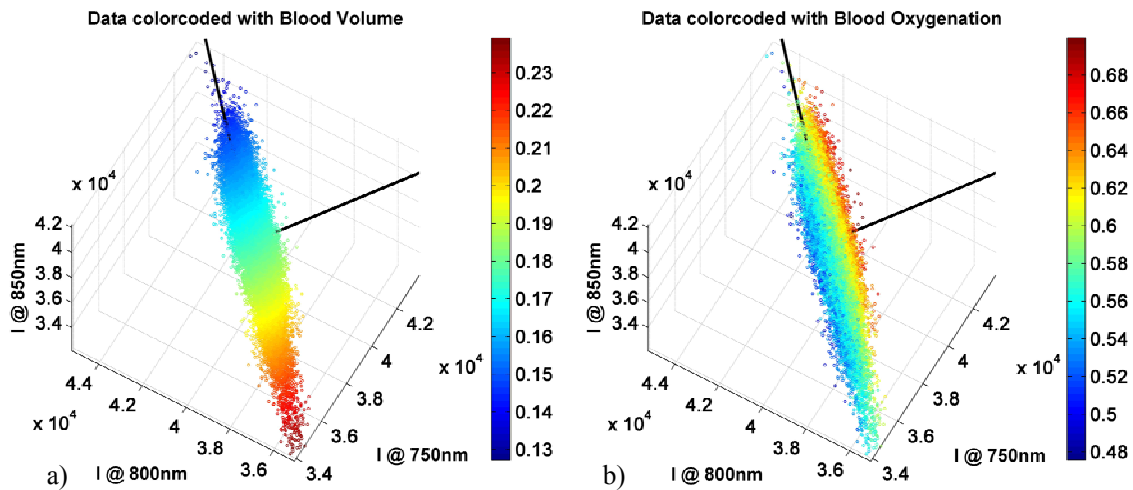


Figure 6.5 3D scatterplots of wavelength specific intensity data colorcoded with a) blood volume and b) blood oxygenation. The black lines indicate the eigenaxes found by PCA. Eigenvector 1 is aligned with blood volume, eigenvector 2 with blood oxygenation.

We subsequently performed PCA for each set of wavelength images and time points for all subjects. Doing so, we obtained three eigenvectors per time point and subject. Eigenvector 1 was found to be the same for each subject and over all 21 time points, except for small angular shifts (data not shown), and being well aligned with blood volume (see Fig. 6.5a). Stability over time and subjects in eigenvector 1 indicates reliability in calculation. Eigenvector 2 and 3 showed large deviations within one subject and no consistent pattern was found over time, indicating that the separation between eigenvector 2 and 3 was ambiguous. An ambiguity in eigenvector 2 and 3 indicates that blood volume and oxygenation can not be reliably separated. Neither eigenvector 2 nor 3 showed any temporal change similar to blood oxygenation over time. Fig. 6.6a demonstrates this non specific behavior, showing a transformed data set along the 2<sup>nd</sup> and 3<sup>rd</sup> eigenvector, color-coded by blood oxygenation. Data shown here is from the same subject as in Fig. 6.5, but at different time point. As the apparent structure of the oxygenation results is not aligned with either eigenvector, PCA failed to

attribute one specific direction to blood oxygenation when performed on one single data set of three wavelength images.

The blood oxygenation color-coded data appeared aligned and perpendicular to the primary axis of the ellipse when looking at each time point separately. The next step in the analysis was therefore to create one large data set per subject, which included all time points (21 times 3 wavelength images) and resulted into one set of eigenvectors per subject. Fig. 6.6b shows the result of the same subject for the large data set color-coded by blood oxygenation. The data are well aligned along the second eigenvector with blood oxygenation values being aligned in the same direction, therefore showing a dependence of the 2<sup>nd</sup> eigenvector on oxygenation. Fig. 6.6c shows the same data as in Fig. 6.6a (one time point) but transformed with the eigenvectors found by the data set including all time points. When applying the subject specific eigenvector set, the data and its oxygenation become aligned to the second eigenvector. This phenomenon is consistent for all subjects and time points, making it possible to separate blood volume and oxygenation.

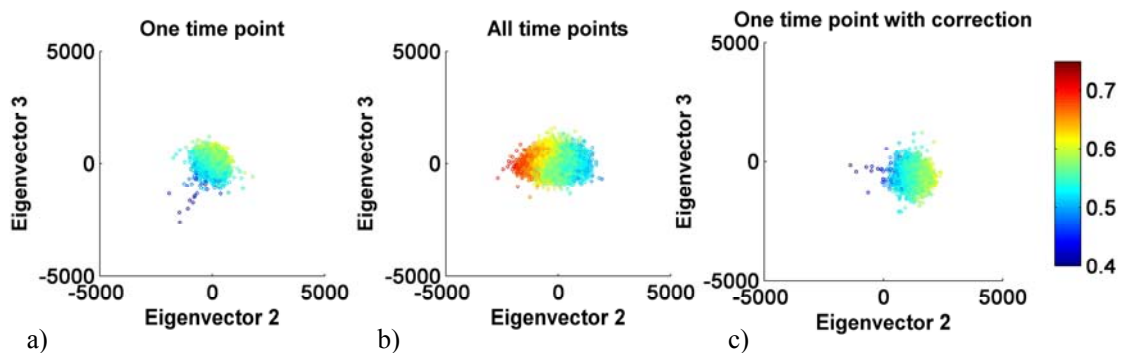


Figure 6.6 Transformed data after PCA in the eigenvector 2 and 3 plane, color-coded with the corresponding blood oxygenation results. 6.6a shows PCA performed on one time point, 6.6b over the data including all time points, and 6c shows the transformed data of one time point using the set of eigenvectors obtained in 6.6b.

In Fig. 6.7 we demonstrate the validity of image summation (creating a single data set for all time points) for PCA analysis. Here we assume that the set of 21 images is sufficient to develop a patient specific component space. We plot ‘n’ against angular offset of the eigenaxes, where n is the number of images used to generate the PCA summation space. For each n we generate 100 random choices of images (note that duplication occurs only for n=1 and n=21). Fig. 6.7a shows the plot of average angular separation of an individual summation space from the average space (21 images), with standard deviation for eigenvector 1 (data in blue). The separation of the final angular

eigensystem from ground truth (given as the eigensystem of the entire image ensemble) is also shown (data in red). Fig. 6.7b and Fig. 6.7c show the same data for eigenvectors 2 and 3.

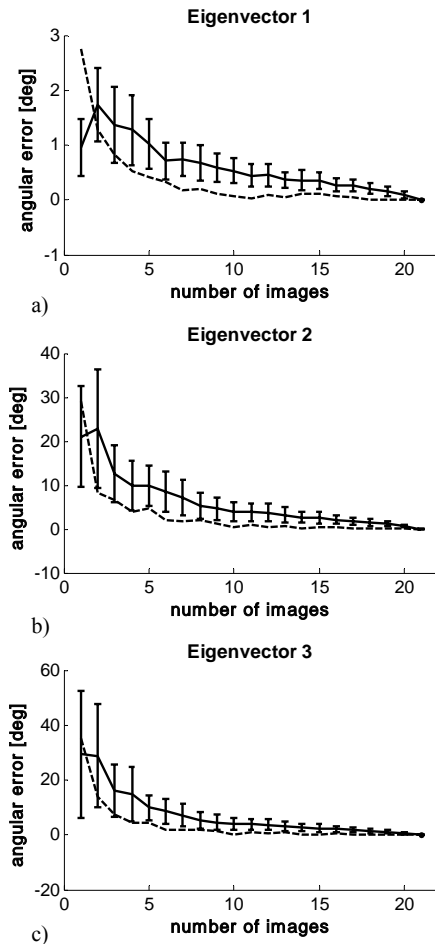


Figure 6.7 Validity of image summation for PCA. Data in blue is average distance from local ensemble plus its standard deviation. Data in red is distance of local ensemble average from ‘truth’ (21 image ensemble). Fig. 6.7a shows data from eigenvector 1; 6.7b from eigenvector 2; and 6.7c from eigenvector 3.

Fig. 6.8 shows the 2D representation of the transformed data along the three eigenvectors over time for the same subject as in Fig. 6.2 and Fig. 6.3. The eigenvectors used were obtained by taking a combined data set of all time points per subject. Fig. 6.8a shows the result for the first eigenvector, which shows the same structures and temporal behavior as blood volume in Fig. 6.2. Eigenvector 2 can be seen in Fig. 6.8b, which shows a similar temporal and spatial appearance as blood oxygenation, as seen in Fig. 6.3. Fig. 6.8c shows eigenvector 3, which does not show significant trends or structures and might be attributed to noise. It shall be mentioned that the scales in the

three images is different from each other and that the first eigenvector is one magnitude larger than eigenvector 2 and 3.

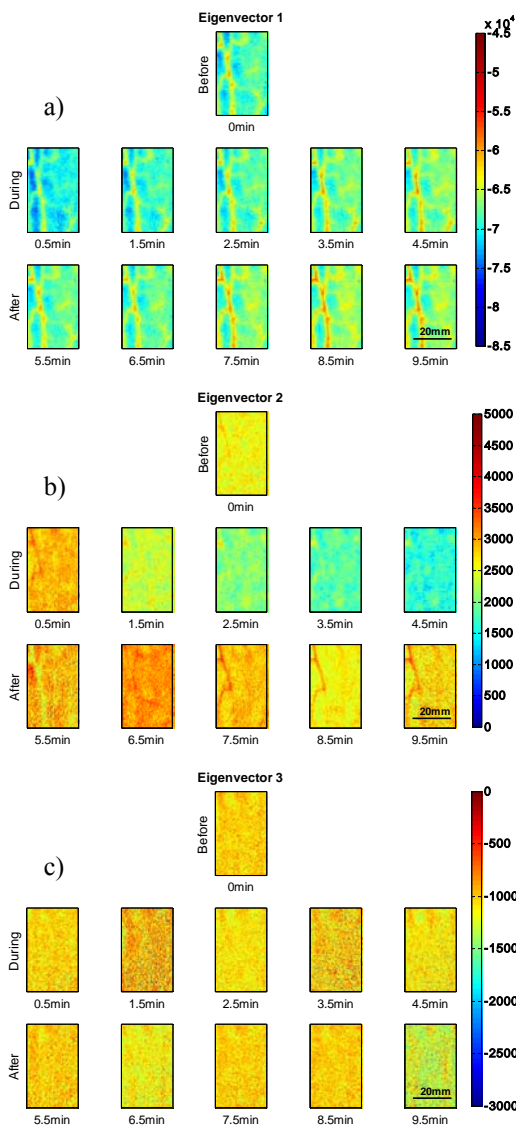


Figure 6.8 Eigenvectors obtained by PCA over time for one subject. 6.8a shows the first eigenvector, which corresponds to blood volume; 6.8b shows the second eigenvector, which corresponds to blood oxygenation; 6.8c shows the third eigenvector.

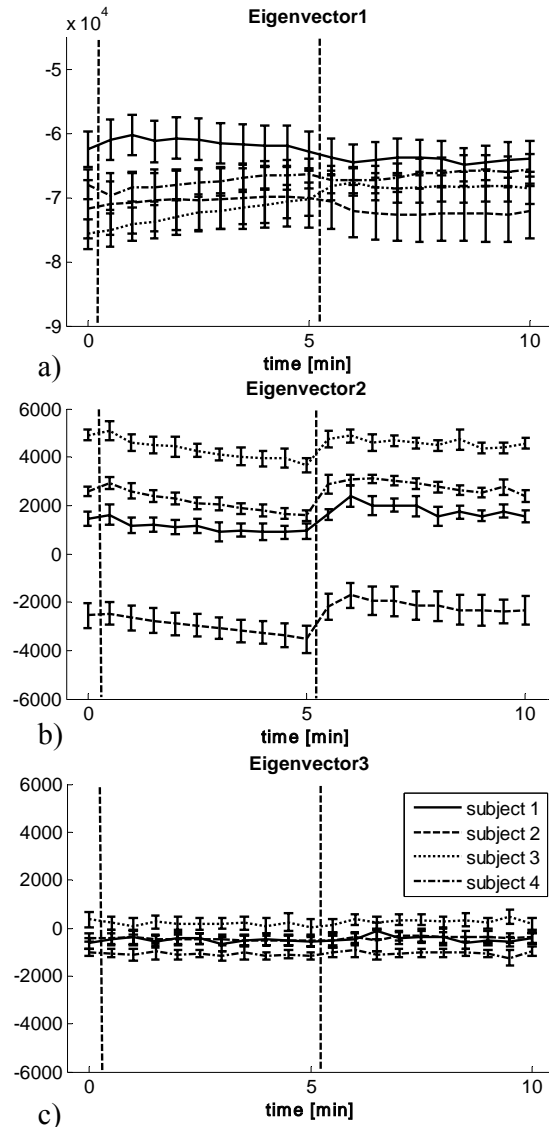


Figure 6.9 Average eigenvectors over time for four subjects. The dashed lines indicate start and end of occlusion. Fig. 6.9a shows eigenvector 1, 6.9b eigenvector 2, 6.9c eigenvector 3.

Results in Fig. 6.9 show the average distances along the eigenvectors. The average was taken as in Fig. 6.4 over the entire 2D maps for each time point, with error-bars given by the standard deviation over all pixels per time point. The qualitative behavior over time for eigenvector 1 (6.9a) matches the behavior seen in Fig. 6.4a; eigenvector 2 (6.9b) shows the same temporal behavior as Fig. 6.4b. Combined with the results from Fig. 6.5 and Fig. 6.6, the data suggest that the first eigenvector can be

described by blood volume and the second one by blood oxygenation. The third eigenvector (6.9c) does not show any change over time.

Fig. 6.10a shows the direct comparison between eigenvector 1 and blood volume and 10b between eigenvector 2 and blood oxygenation for all pixels and time points per subject. A clear almost linear relationship can be seen between eigenvector 1 and blood volume, indicating that these two are uniquely correlated. The same trend can be seen for all subjects, but subject 3 shows a shift towards higher blood volume values. Fig. 6.10b shows the results for eigenvector 2 versus blood oxygenation. The relationship is not as linear but blurred compared to 10a, as well as shifted along the eigenvector axis. This indicates that blood oxygenation values can be recovered within a constant shift compared to reconstruction results.

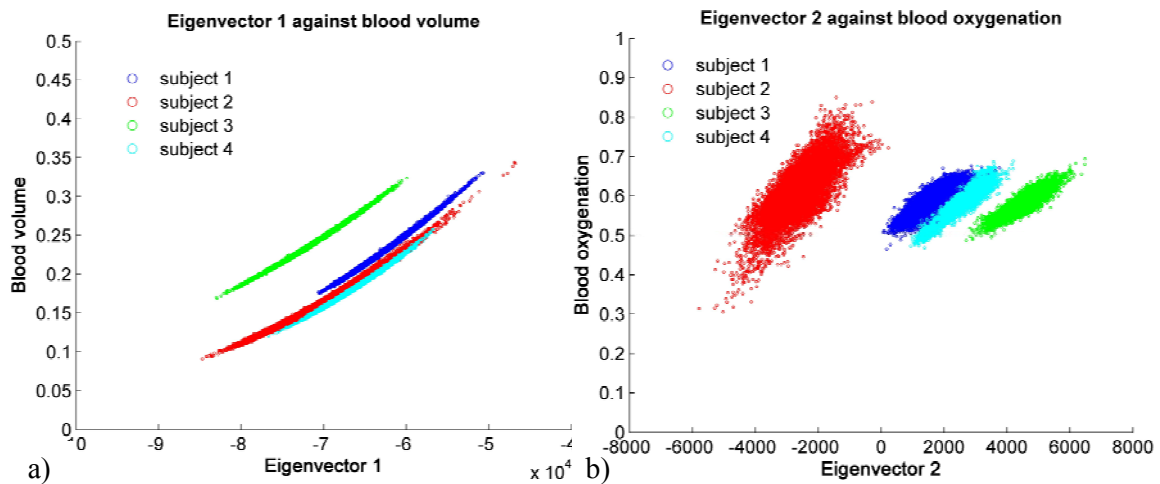


Figure 6.10 Blood volume vs. eigenvector 1 (6.10a) and Blood oxygenation vs. eigenvector 2 (6.10b).

## 6.6 Discussion

Diffuse multi spectral imaging of skin in the near infrared wavelength range allows for quantitative chromophore assessment which can be used to attain functional information. Especially blood volume and oxygenation are of interest for skin lesion treatment follow up as a parameter of the angiogenic process and metabolic state of a tumor. Previous work of assessing these parameters in healthy and diseased skin [Attas et al., 2001; Jacques et al., 2002; Kainerstorfer et al., 2009a; Mantis & Zonios, 2009; Miyamae et al., 2008; Tseng et al., 2009; Vogel et al., 2007; Vogel et al., 2006; Zakian et al., 2008] included fitting the acquired intensity data to an analytical model of photon migration in diffuse media. Reconstructed concentration maps are therefore based on

the wavelength dependent absorption coefficient and require an accurate model. Furthermore, model based reconstruction is computationally intense and time consuming, therefore not applicable for real time assessment in a clinical setting.

PCA has been used as a tool to analyze digital RGB images for extracting blood and melanin concentration and for lesion segmentation in various conditions [Cheng et al., 2008; Hance et al., 1996; She et al., 2007; Tsumura et al., 1999; Umbaugh et al., 1993]. To our best knowledge, no attempt was done for extraction of blood oxygenation using PCA from RGB or multispectral images or for comparison of PCA with reconstruction results.

The reconstruction results of four healthy volunteers undergoing occlusion of the upper arm and imaged at the forearm (Fig. 6.2-6.4) presented in this work demonstrate that the spatial distribution (Fig. 6.8) and temporal behavior (Fig. 6.9) of eigenvector 1 matches that of blood volume and eigenvector 2 matches that of blood oxygenation. In order to obtain these results, one data set, including all time points per subjects, was created, as we have seen that PCA does not pick up on blood oxygenation otherwise. Surprisingly the subject specific eigenvector set is the same for all four subjects with only small angular shifts smaller than 7 degree (data not shown). This overlap in eigenvectors indicates that it might be possible to create one general set of eigenvectors describing blood volume and oxygenation. This of course raises the question if such a description is valid when applied to a different data set, i.e. from skin lesions, and if the transformation still holds. In addition, arterial blood could not be imaged, as arteries lie deeper in the skin. It would be of interest to validate the PCA results with arterial oxygenation values, which are in the order of 99%.

The results also indicate an almost linear dependence of the first eigenvector with blood volume (Fig. 6.10a), demonstrating that values from PCA can be converted to actual concentrations of blood volume. Only subject 3 showed a deviation from the others in terms of a shift towards higher values of blood volume. This shift might be explained by the nature of our reconstruction algorithm, which assumes the same epidermal thickness for all subjects' forearms (60 $\mu$ m). We have data (unpublished) which shows that a difference of the epidermal thickness within the standard deviation of reported literature values for arms will lead to a significant overestimation of blood volume. The shift in Fig. 6.10a can therefore be explained by the inaccuracy of the reconstruction rather than due to PCA errors.

Fig. 6.10b indicates that there is a defined relationship between eigenvector 2 and blood oxygenation, but it is much more blurred and shifted along the eigenaxis. We hypothesize that the blurring might be partially explained by reconstruction errors of blood oxygenation as well as PCA itself. As mentioned above, PCA applied to one single image did not successfully align the axis of oxygenation changes to one specific eigenaxis and a data set including all time points was required to do so. The data was therefore centered on the mean of the large data set, not the individual ones. As the second principal component is one order of magnitude smaller than the first component, even small shifts in the data over time will lead to relatively larger errors (blurring) compared to the first component. The shift along the second eigenvector, in particular for subject 2 (Fig. 6.10b), might well be explained by centering the large data set rather than the individual ones. When transforming the data with a given set of eigenvectors, the resulting data is not necessarily centered on the origin, leading to shifts along the axes.

The results from the direct comparison between reconstruction of blood volume and oxygenation with the PCA results of the same multi-spectral image set indicates that PCA may be a viable alternative tool for skin chromophore assessment. Future work will have to include phantom experiments as well as skin structure assessment for improvement of the reconstruction results and thus explaining remaining variation in the direct comparison between PCA and reconstruction results. Since PCA is considerably faster (three orders of magnitude) compared to the time consuming reconstruction algorithms commonly used, it may provide a significant advantage for extracting metabolic information results in real time. Future work will include applying PCA to multi spectral data from skin surface lesions, as well as acquiring more data from healthy volunteers to increase statistical power.

## **6.7 Conclusion**

We acquired multi spectral images from healthy volunteers' lower forearms during an occlusion experiment and compared reconstruction results for blood oxygenation and blood volume with results from PCA. Reconstruction was performed by fitting the data to our two layered analytical skin model and blood oxygenation results showed the expected course of ischemia during occlusion and reactive hyperemia afterwards. PCA was performed on a large data set of all time points per

subject and one subject specific set of eigenvectors was used to transform the time dependent data. Results showed that the first principal component corresponds well to the time course and spatial distribution of blood volume, the second one to blood oxygenation, and the third one did not show any temporal or spatial change. A direct comparison between reconstruction results and principal components showed a linear dependence between blood volume and blood oxygenation with the first and second component respectively. The correspondence between blood oxygenation and the second principal component was blurred and a shift between subjects was observed, indicating that the dependence is more susceptible to noise and errors. The results are encouraging and demonstrate the potential of PCA for quantitative skin chromophore assessment. The biggest advantage of PCA compared to reconstruction algorithms is its computational inexpensiveness, with PCA being three orders of magnitude faster. This allows for real time mapping of skin chromophores with PCA and would therefore find great use in clinical routines.

**Acknowledgements:** The research was funded by the Intramural Research Program of the Eunice Kennedy Shriver National Institute of Child Health and Human Development. The Graduate Partnership Program at the National Institutes of Health and the Department of Physics at the University of Vienna in Austria are also acknowledged.



## **Chapter 7**

### **Interlude 2 – Reconstruction-Free Imaging of Kaposi’s Sarcoma Using Multi-Spectral Data**

In the previous chapter, PCA was used on healthy skin and it was shown that the first eigenvector corresponds to blood volume and the second eigenvector to blood oxygenation. Here it shall be shown that the same is true for diseased skin. This chapter is based on a conference proceeding, presented at OSA Biomedical Optics (BIOMED) Topical Meeting, Miami, 2010 [Kainerstorfer J. M. et al., 2010].

#### **7.1 Abstract**

Multi-spectral imaging was used for Kaposi’s sarcoma lesion follow-up. Reconstruction of blood volume and oxygenation as well as Principal Component Analysis was performed and we demonstrate the relationship between the first and second eigenvector and blood volume and oxygenation, respectively, with the advantage of obtaining results in real-time when using PCA.

#### **7.2 Introduction**

Assessment of the metabolic state of skin surface lesions is often desired in clinical routines as a measure for treatment outcome. Diffuse multi-spectral imaging of the skin combined with an analytical skin model can provide this information by producing spatial maps of skin chromophore concentrations [Arimoto, 2007; Kainerstorfer et al., 2009b; Vogel et al., 2007]. The disadvantage of this method lies in the computationally expensive data post processing, making real time conclusions difficult or even impossible if the sample size is large.

The basic idea of PCA is to reveal the data components (in a decreasing order) that best explain the variance in the data. The main advantage of PCA is the speed of computation, which allows analysis in real time. Here we are describing multi-spectral

imaging on Kaposi's sarcoma skin surface lesions and apply a reconstruction algorithm as well as PCA. We will show reconstruction results over the course of treatment, therefore following the metabolic state of the tumor and will show that qualitatively the same results can be obtained with PCA. Furthermore we propose PCA on multi-spectral images for clinical routines for real time vascular imaging of lesion progression or regression.

## **7.3 Materials and Methods**

### **7.3.1 Kaposi's Sarcoma Patients**

Kaposi's sarcoma (KS) is a frequent cause of morbidity and mortality among individuals infected with human immunodeficiency virus (HIV). HIV related Kaposi's sarcoma (KS) is a multicentric angioproliferative neoplasm, caused by KS associated herpes virus (KSHV / HHV-8). Patients develop skin surface lesions, which vary in size, and color, where the color is due to the highly vascular nature of the lesion and subsequent vessel leakage, which leads to the breakdown of hemoglobin and consequent hemosiderin formation. KS lesions may be red, purple, brown, or black, and are usually raised above the skin. Growth can range from very slow to explosively fast, and be associated with significant mortality and morbidity.

The HHV-8 virus encodes for several factors with angiogenic activity and KS spindle cells have been shown to produce and respond to a number of proangiogenic factors including basic fibroblast growth factor (bFGF) and vascular endothelial growth factor (VEGF) [Boshoff & Endo, 1997; Ensoli & Barillari, 1992]. Also, KSHV encodes for a constitutively active G-protein coupled receptor (ORF74) that induces a pro-angiogenic state and upregulates VEGF production in part through activating hypoxia inducible factor (HIF) [Bais & Santomasso, 1998; Sodhi & Montaner, 2000]. Cutaneous KS lesions are easily accessible for noninvasive techniques that involve imaging of tumor vasculature, and they may thus represent a model tumor in which to assess certain parameters of angiogenesis.

Patients enrolled in this study were treated with an agent that blocks angiogenesis, which is Intravenous Recombinant Humanized anti-vascular endothelial cell growth factor antibody, called Bevacizumab, more commonly known as Avastin. One lesion was selected for follow up with multi-spectral imaging, and was imaged

before treatment and approximately every 12 weeks during therapy. All patients gave written informed consent, and the protocol was approved by the Institutional Review Board of the National Cancer Institute.

### 7.3.2 Instrumentation

A non-invasive, non-contact diffuse reflectance multi-spectral imaging system has been used, which was described in detail previously [Kainerstorfer et al., 2009b; Vogel et al., 2007]. Polarized light from a white light source (halogen 150W) is used for illumination of the sample. A second polarizer is placed before the detection unit, perpendicular to the incident beam polarization, thus guaranteeing diffuse reflectance measurements and removal of specular reflection [Demos & Alfano, 1997b].

Light is captured in a CCD camera (Princeton Instruments CCD-612-TKB, Roper Scientific) after passing consecutively one of six narrow bandpass filters (40nm FWHM, CVI Laser) on a filter wheel. Six wavelength images are taken, the wavelengths being 700, 750, 800, 850, 900 and 1000nm. For calibration purposes, images from a 90% reflectance paper (Kodak) are taken.

### 7.3.3 Reconstruction of skin chromophores

*In vivo* data acquired from Kaposi's sarcoma lesions using diffuse multi-spectral imaging was used for reconstruction of blood volume and oxygenation. Reconstruction was performed by least squares non linear fitting of the data to our analytical skin model. Four wavelength ( $\lambda$ ) images were used for reconstruction, being 700, 750, 800, and 850nm. The analytical skin model used is based on a two layered structure, the first one being the melanin containing epidermis, the second one being the blood containing dermis and can be written as:

$$I_e(\lambda) = S \cdot A_e(\lambda)^2 \cdot A_d(\lambda) \quad (1)$$

The attenuation by the epidermis,  $A_e$ , is based on Lambert's law and can be written as:

$$A_e(\lambda) = e^{-\mu_e \cdot d_e} = e^{-(v_m \cdot 0.66 \cdot 10^{11} \cdot \lambda^{-3.33} \cdot d_e)} \quad (2)$$

with  $v_m$  the concentration of melanin,  $d_e$  the thickness of the epidermis and  $\mu_e$  the absorption coefficient of the epidermis, which is based on the absorption of melanin.

The attenuation by the dermis,  $A_d$ , which includes the absorption due to blood volume and oxygenation, is based on the analytical solution of photon migration in turbid media based on random walk theory and can be written as:

$$A_d(\lambda) = \frac{e^{-2(\mu_d/\mu_s)}}{\sqrt{24(\mu_d/\mu_s)}} \cdot \left(1 - e^{-\sqrt{24(\mu_d/\mu_s)}}\right) \approx 1.06 - 1.45 \cdot (\mu_d/\mu_s)^{0.35} \quad (3)$$

$$\mu_d = v_{db} \cdot \left[ (1 - v_{boxy}) \cdot \mu_{deoxygen} + (v_{boxy}) \cdot \mu_{oxy} \right] \quad (4)$$

where  $\mu_s$  is the reduced scattering coefficient and  $\mu_d$  is the absorption coefficient of the dermis. The scaling factor  $S$ , blood volume,  $v_{db}$ , and blood oxygenation,  $v_{boxy}$ , are unknown a priori and were solved for.

### 7.3.4 Principal Component Analysis

Principal component analysis (PCA) is a statistical tool that linearly transforms the data into an orthogonal coordinate system whose axis correspond to the principal components in the data, i.e., the first principal component accounts for as much variance in the data as possible and, successively, further components capture the remaining variance. Through an eigenanalysis, the principal components are determined as eigenvectors of the dataset's covariance matrix and the corresponding eigenvalues refer to the variance that is captured within each eigenvector.

We acquired multi-spectral images from KS patients for three wavelengths (750, 800, 850nm), which provides a datacube that is built from three-dimensional pixel vectors. In this wavelength range, the dominant chromophore is blood and should therefore explain most of the variance of the data. PCA was performed on the collection of three-dimensional pixel vectors. We then projected the data along the eigenvectors.

## 7.4 Results

Multi-spectral data was collected before the therapy and on three consecutive visits during the therapy (week 14, 26, and 38). Digital images in figure 7.1 show the lesion over time. Reconstruction of blood oxygenation and blood volume was performed and results can be seen in figure 7.2 and 7.3, with the colorbars indicating fractional concentrations. Before treatment (week 0), a clear reduction in blood oxygenation can be seen within the lesion (figure 7.2), surrounded by a ring like shape

of hypoxic tissue. A local increase in blood volume is seen as well (figure 7.3), which does not extend to surrounding tissue. After 14 weeks of treatment, a decrease in blood volume and an increase in blood oxygenation can be seen, indicating remission of the disease, whereas the digital image does not show any decrease in size. The same trend is observed 26 weeks and 38 weeks after start of treatment. The patient was released from the protocol at week 48, with pathologic complete remission of disease.



Figure 7.1. Digital images of KS lesion over time. left to right: week 0, 14, 26, and 38

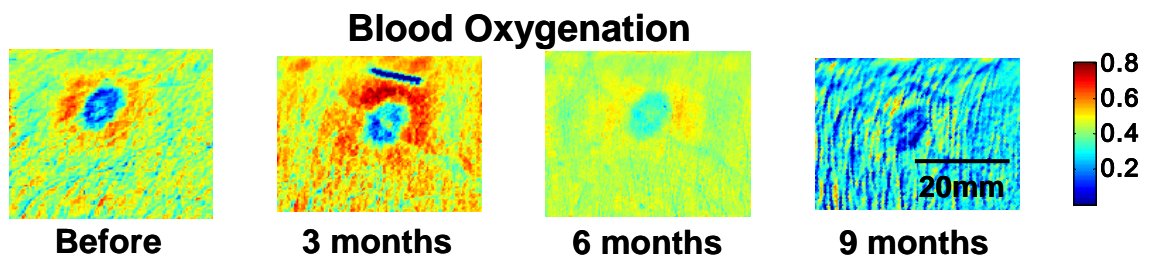


Figure 7.2. Blood oxygenation over time. left to right: week 0, 14, 26, and 38

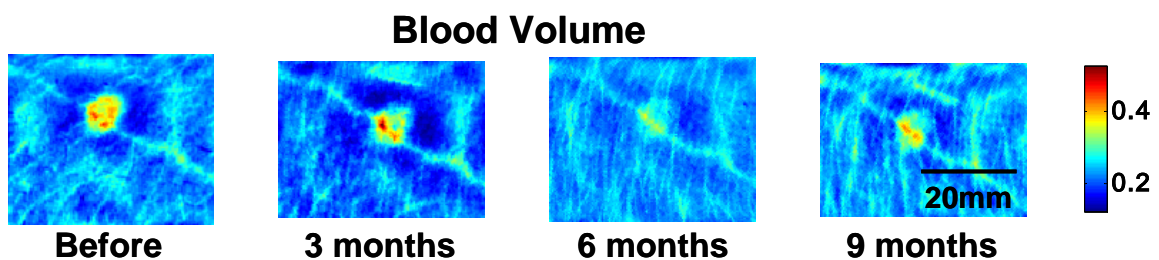


Figure 7.3. Blood volume over time. left to right: week 0, 14, 26, and 38

In figure 7.4 we see results obtained by PCA, showing the projection along the first and second eigenvector in arbitrary units. A similar spatial distribution of local changes of blood oxygenation within the lesion can be seen before treatment (figure 7.4 left). The same spatial distribution in eigenvector 1 compared to blood volume can be seen in figure 7.5. The PCA results also show strong correlation with the reconstruction results throughout the treatment (temporal behavior).

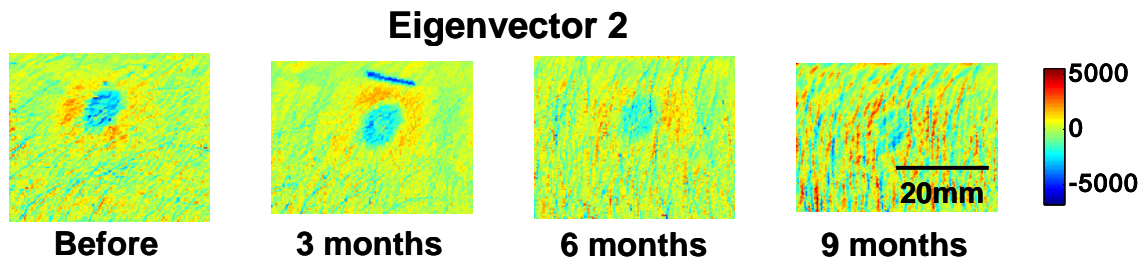


Figure 7.4. Projection along the second eigenvector. left to right: week 0, 14, 26, and 38

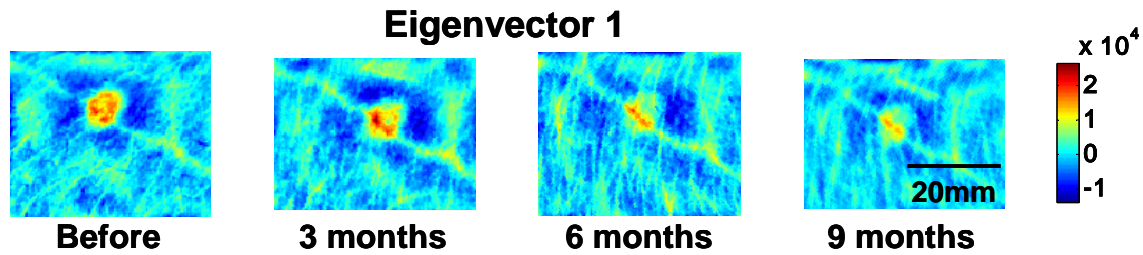


Figure 7.5 Projection along the first eigenvector. left to right: week 0, 14, 26, and 38

## 7.5 Discussion and Conclusion

Multi-spectral imaging was used for Kaposi's sarcoma lesion follow-up. Reconstruction of blood volume and oxygenation as well as Principal Component Analysis was performed and we demonstrate the relationship between the primary eigenvector and blood.

Results of oxygenation and blood volume showed an increase and decrease (figure 7.2 and 7.3) respectively inside the lesion over the course of the treatment. Results indicated remission of the disease already at week 14, even though the lesion on the surface did not clinically decrease in size. Pathologic complete remission of disease was confirmed by the clinic in week 48.

Principal component analysis has been applied to the same data set and the projection along the first and second eigenvector was calculated for each pixel. The 2D spatial representation of this projection shows the same distribution as reconstructed blood volume (figure 7.5) and oxygenation (figure 7.4). Furthermore, the changes over time resemble those of blood volume and blood oxygenation.

When in clinical routine, very often a real time assessment of the lesion and its metabolic state is desired. Reconstruction of blood volume and blood oxygenation has the potential to deliver quantitative results, but the drawback is that it is computationally expensive and seldom achievable in real time. PCA proves to be an alternative to

reconstruction of blood and due to its computational inexpensiveness could be used in real time. Future work will include assessment of PCA as a quantitative tool for blood volume and oxygenation extraction. In order to bring clinically useful meaning to the obtained data, the unitless PCA results will have to be converted into actual concentrations. Only if actual concentrations of blood volume and blood oxygenation can be obtained with PCA, conclusions about the treatment course can be drawn.



## Chapter 8

# Original paper 3 – Quantitative principal component model for skin chromophore mapping using multi spectral images and spatial priors

### 8.1 Abstract

We describe a reconstruction algorithm based on Principal Component Analysis (PCA) applied to multi-spectral imaging data, which produces quantitative characterization of blood volume/oxygenation distributions in real time. Using numerical phantoms, we develop analytical expressions, which convert initial PCA results into actual blood volume and oxygenation values, assuming the epidermal thickness to be known. We also evaluate the limits of accuracy of this method when the value of the epidermal thickness is not known. We show that blood volume can reliably be extracted (within 10% error) even if the difference between actual and assumed thickness is as large as 0.08mm, whereas the error in blood oxygenation can be as large as 50% for the same difference in thickness. This PCA based reconstruction was found to extract blood volume and blood oxygenation within 8% error, if the underlying structure is known. These estimated performance characteristics indicate that this approach may be a suitable tool for clinical implementation.

### 8.2 Introduction

Assessment of the metabolic state of skin surface lesions is often desired in clinical routines as a measure for treatment outcome. Since the main absorbing components of the skin in the near-infrared spectrum are blood, melanin, lipids, and water, spatial maps of those can be obtained by near infrared diffuse multi-spectral imaging. Such concentration maps can be provided by applying an analytical, numerical, or stochastic skin model, where reconstruction is usually performed pixel by pixel. Diffuse multi spectral imaging of the skin and image reconstruction of skin

chromophores has already found its application in the clinic, successfully assessing parameters for healthy and diseased skin [Attas et al., 2001; Jacques et al., 2002; Mantis & Zonios, 2009; Miyamae et al., 2008; Tseng et al., 2009; Vogel et al., 2007; Zakian et al., 2008]. The main disadvantage of these methods arises from calculating the parameters by fitting the digitized imaging data to a model, which, dependent on the model used and the image size, can be rather computationally expensive. As a result, these methods are not capable to address applications where the functional information is needed in real time.

Principal Component Analysis (PCA) applied to multi-spectral images in the near-infrared has been proposed previously as an alternative tool for assessing skin chromophores [Kainerstorfer et al., 2010c; Tsumura et al., 1999; Umbaugh et al., 1993]. PCA, first introduced in 1901 [Pearson, 1901], is a statistical tool, which linearly transforms imaging data into an orthogonal coordinate system, where the axes correspond to the inherent information within the data set. One of the biggest advantages of using PCA lies in its speed of computation, which allows real-time analysis of large image sets. PCA has found applications in fields such as face recognition [Moon & Phillips, 2001; Turk & Pentland, 1991], image compression [Du & Fowler, 2008], pattern recognition in high dimensional data [Ferraz et al., 1998], analysis of gene expression data [de Haan et al., 2007; Nishimura et al., 2003; Sghaier-Hammami et al., 2009], dimension reduction [Begelman et al., 2009], as well as image enhancement [Mandelkow et al., 2010]. Applied to optical imaging, PCA has been used for noise reduction and image enhancement [Mandelkow et al., 2010] in multi spectral imaging data for biological cell analysis [Nuffer et al., 2006] to pattern analysis for skin lesion classification [She et al., 2007]. Applied to RGB images, PCA was used on relative color features for unsupervised lesion classification [Cheng et al., 2008; Hance et al., 1996; Umbaugh et al., 1993].

Using PCA for extracting blood and melanin values has been proposed by Tsumura et al. [Tsumura et al., 1999], showing that skin color in digital RGB images can be described by attributing melanin and blood to the first two principal components. Fadzil et al. [Fadzil et al., 2009; Nugroho et al., 2007] applied PCA and Independent Component Analysis (ICA) to RGB imaging data for extraction of blood and melanin values in vitiligo lesions to qualitatively evaluate the skin re-pigmentation progression. Our group has shown previously [Kainerstorfer et al., 2010c] that PCA applied to multi-spectral images from the skin in the wavelength range between 750nm and 850nm can

be used for mapping blood volume and blood oxygenation, where the first eigenvector describes blood volume, the second eigenvector blood oxygenation. This description was found to qualitatively match the temporal behavior and spatial distribution of reconstruction results, using a two-layered analytical skin model. However, a subject dependent shift in the data was also observed, which was hypothesized to be due to epidermal thickness variations.

The aim of this paper is to explore the ability of PCA to provide clinically relevant accuracy, thus obtaining quantitative blood volume and oxygenation values. To the best of our knowledge, no attempt was done previously for converting PCA results into actual concentrations, which we will be referring to as PCA based reconstruction. We are thus investigating a PCA based reconstruction of blood volume and blood oxygenation from multi-spectral images. The main advantage of PCA based reconstruction lies in the computation time. Reconstruction of multi-spectral images based on non-linear fitting of the data can take several hours, whereas the results of the PCA based reconstruction explored in this work can be provided in real-time.

The work is performed by introducing numerical phantoms based on an analytical two-layered skin model for photon migration in the near infrared spectrum, where the first layer describes the epidermis and the second one the dermis. We created multiple image sets, all sets having the same spatially varying blood volume and blood oxygenation distribution, but different epidermal thickness. We then apply PCA on each image set of three wavelengths and show the correlation between the first eigenvector and blood volume as well as the second eigenvector and blood oxygenation, both in dependence of the epidermal thickness. Based on those correlations we describe analytical expressions for converting values on the eigenvector 1 axis to blood volume values, as well as values on the eigenvector 2 axis to blood oxygenation values. We postulate that the accuracy of PCA based reconstruction is dependent on the epidermal thickness. To address this issue, we assume prior knowledge of the underlying skin structures imaged and we estimate the error in the reconstruction if the epidermal thickness used deviates from the actual values.

## 8.3 Materials and Methods

### 8.3.1 Multi-Spectral Instrument

The diffuse reflectance multi-spectral imaging system used in this work has been described in detail elsewhere [Vogel et al., 2007] and shall only be described here briefly. Polarized light from a white light source (halogen 150W) is used for illumination of the sample. A second polarizer is placed before the detection unit, with its polarization orientation perpendicular to the incident beam polarization, thus guaranteeing diffuse reflectance measurements and removal of specular reflection [Demos & Alfano, 1997a].

Images are captured by a CCD camera (Princeton Instruments CCD-612-TKB, Roper Scientific) after passing consecutively narrow bandpass filters (700, 750, 800, 850 nm; 40nm FWHM, CVI Laser). For calibration purposes, images from a 90% reflectance paper (Kodak) are also acquired at each image filter.

### 8.3.2 Analytical two-layered skin model

The skin model has been previously described in detail [Kainerstorfer et al., 2010b; Kainerstorfer et al., 2010c; Vogel et al., 2007]. The model is based on a two layered structure, the first one being the melanin containing epidermis, the second one being the blood containing dermis, with optical properties of the skin taken from literature values [Jacques, 1998; Meglinski & Matcher, 2002; Prahl, 1998], and can be written as:

$$I_e = S \cdot A_e(\lambda)^2 \cdot A_d(\lambda) \quad (8.1)$$

where  $I_e$  is the wavelength ( $\lambda$ ) dependent intensity measured in the CCD camera,  $S$  is a scaling factor,  $A_e(\lambda)$  the wavelength dependent attenuation by the epidermis, and  $A_d(\lambda)$  the attenuation by the dermis. The attenuation by the epidermis,  $A_e(\lambda)$ , is based on Lambert's law and can be written as:

$$A_e(\lambda) = e^{-\mu_e \cdot d} = e^{-(v_m \cdot 0.66 \cdot 10^{11} \cdot \lambda^{-3.33} \cdot d)} \quad (8.2)$$

with  $v_m$  the concentration of melanin,  $d$  the thickness of the epidermis and  $\mu_e$  the absorption coefficient of the epidermis, which is based on the absorption of melanin. The attenuation by the dermis,  $A_d(\lambda)$ , which includes the absorption due to blood

volume,  $v_{db}$ , and oxygenation,  $v_{boxy}$ , is based on the analytical solution of photon migration in turbid media [Gandjbakhche & Weiss, 1995a] based on random walk theory and can be written as:

$$A_d(\lambda) = \frac{e^{-2(\mu_d / \mu'_s)}}{\sqrt{24(\mu_d / \mu'_s)}} \cdot \left(1 - e^{-\sqrt{24(\mu_d / \mu'_s)}}\right) \approx 1.06 - 1.45 \cdot (\mu_d / \mu'_s)^{0.35}, \quad (8.3)$$

$$\mu_d = v_{db} \cdot \left[ (1 - v_{boxy}) \cdot \mu_{deoxygenated} + (v_{boxy}) \cdot \mu_{oxygenated} \right] \quad (8.4)$$

where  $\mu'_s$  is the reduced scattering coefficient and  $\mu_d$  is the absorption coefficient of the dermis, with  $\mu_{deoxygenated}$  and  $\mu_{oxygenated}$  being the absorption coefficients of deoxygenated and oxygenated blood respectively.

### 8.3.3 Principal Component Analysis

Principal Component Analysis (PCA) and reasoning for applying it to multi-spectral images have been described before [Kainerstorfer et al., 2010c; Kainerstorfer J. M. et al., 2010] and shall only be touched briefly here. PCA [Pearson, 1901] linearly transforms the imaging data into an orthogonal coordinate system whose axes correspond to the principal components in the data, i.e., the first principal component accounts for as much variance in the data as possible and, successively, further components capture the remaining variance. Through an eigenanalysis, the principal components are determined as eigenvectors of the dataset's covariance matrix and the corresponding eigenvalues refer to the variance that is captured within each eigenvector.

For three wavelength images, PCA is performed on the collection of three-dimensional pixel vectors of the zero mean data. The three eigenvectors  $p_1, p_2, p_3$  - the principal components ordered according to the magnitude of their eigenvalues - provide the transformed data

$$Y = W^T X \quad (8.5)$$

where  $W = (p_1 \ p_2 \ p_3)$ . Rearranging the vectors in  $Y$  into matrices yields again three 2D images. We showed previously [Kainerstorfer et al., 2010c] that, when applied to multi-spectral skin imaging data between 750nm and 850nm, the first eigenvector qualitatively correlates with blood volume, and the second with blood oxygenation.

### 8.3.4 Numerical Phantoms

We created numerical phantoms of intensity images based on the two layered skin model (equations (1-4)). Those wavelength images (750nm, 800nm, and 850nm) were 500 pixels x 500 pixels, with each pixel having a given unique combination of blood volume and blood oxygenation values. These values were set to vary between 0.001 – 0.5 fractional blood volume and 0.001 – 0.99 fractional blood oxygenation, covering physiologically relevant as well as extreme values. The spatial distribution of blood volume and blood oxygenation can be seen in figure 8.1. The scaling factor,  $S$ , in equation (1) was held constant and set to be  $S = 9.26 \cdot 10^4$ , taken from previous in vivo imaging data calculation [Kainerstorfer et al., 2010c; Vogel et al., 2007]. Since the scaling value is dependent on the exposure time of the camera, the average  $S$  value was calculated based on previous subject data and used here. The value for melanin was held constant as well and set to be  $v_{mel} = 0.08$ , which corresponds to a Fitzpatrick scale value of 1 [Roberts, 2009 ].

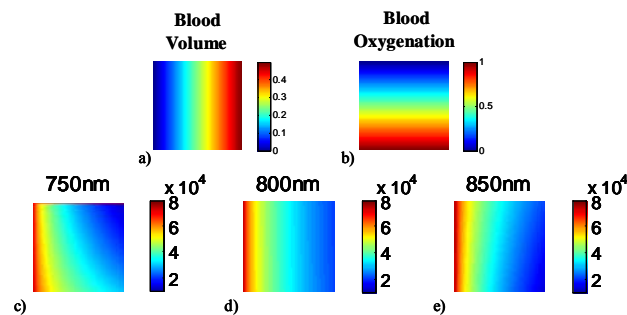


Fig. 8.1. Spatial distributions of blood volume (a) and blood oxygenation (b) for the numerical phantoms. Each resulting intensity image pixel has a unique combination of those two. Resulting intensity images with epidermal thickness of  $d = 0.06$  mm are shown for 750 nm (c), 800 nm (d), and 850 nm (e).

In order to account for the influence of the epidermal thickness on PCA results, different image sets were created, in total 30 images sets. The blood volume and oxygenation distribution was held the same for all sets, but the epidermal thickness was varied. Ten sets were created, with each one having a uniform (flat) epidermal thickness (d) distribution, with the epidermal thickness being  $d = [0.02, 0.04, 0.06, 0.08, 0.10, 0.12, 0.14, 0.16, 0.18, 0.20]$  mm for all image pixels. One set of intensity images with  $d = 0.06$ mm can be seen in figure 8.1c-e.

Since PCA is performed on the 2D images rather than pixel wise, spatial variations had to be evaluated as well. Thus, another ten sets of intensity images were created with a spatially varying epidermal thickness, containing three different thicknesses ( $d_1$ - $d_3$ ), arranged in a grid pattern. The values for those were chosen as seen in table 1. The last set of ten image sets was created based on the grid patterns, with the center pixel being smaller than the other pixels, with a thickness  $d_4$ , shown in table 1. The reason for this third set of images was results driven, as we will show that the smallest thickness within the image becomes an important variable.

**Table 1. Epidermal thickness variation within different image sets**

$d_1$ [mm]	$d_2$ [mm]	$d_3$ [mm]	$d_4$ [mm]
0.02	0.04	0.06	0.015
0.03	0.07	0.11	0.02
0.04	0.08	0.12	0.03
0.06	0.09	0.12	0.03
0.07	0.10	0.13	0.05
0.08	0.10	0.12	0.06
0.10	0.14	0.18	0.09
0.11	0.13	0.15	0.08
0.12	0.15	0.18	0.09
0.14	0.16	0.18	0.13

### 8.3.5 PCA on numerical phantoms

PCA was performed separately for each image set (30 in total) of 750nm, 800nm, 850nm images, resulting in 30 eigenvector sets of 3; 10 for spatially uniform  $d$  and 20 for spatially varying  $d$ . The correlation between eigenvector 1 and blood volume, as well as eigenvector 2 and blood oxygenation, was then evaluated in dependence to  $d$ .

### 8.3.6 PCA based reconstruction

In order to convert the unitless PCA results into actual blood volume and blood oxygenation values, the imaging data projection onto the eigenvectors was being investigated in dependence of blood volume, oxygenation, and epidermal thickness. The

data projected onto eigenvector 1 was plotted against blood volume and eigenvector 2 against blood oxygenation. By curve fitting of the data, analytical expressions could be found, which convert eigenvector 1 into blood volume and eigenvector 2 into blood oxygenation, both as a function of the epidermal thickness. This conversion will be referred to as PCA based reconstruction and is described in detail in the results section.

### **8.3.7 Thickness dependent error analysis**

Using those numerical phantom image sets, reconstruction, using the two layered skin model, and PCA based reconstruction of blood volume and oxygenation was performed, assuming an epidermal thickness of  $d=0.06\text{mm}$  for all sets, which does not correspond to the actual thickness. This chosen value corresponds to a representative literature value for the lower forearm [Mogensen et al., 2008; Whitton & Overall, 1973]. Reconstruction with the analytical two layered skin model will be from now on referred to as reconstruction, in comparison to PCA based reconstruction. Since the image sets have given blood volume and oxygenation values, the thickness dependent error in reconstruction could be calculated. The error was defined as true blood volume and oxygenation, minus blood volume and oxygenation, assuming  $d=0.06\text{mm}$ .

## **8.4 Results**

### **8.4.1 PCA applied to numerical phantoms**

PCA was performed separately for each image set. The relationship between data projected onto eigenvector 1 and blood volume values, as well as eigenvector 2 and blood oxygenation values for image sets of uniform and spatially varying epidermal thickness are shown in figure 8.2. The first row of images (a-c) shows these relationships for uniform epidermal thickness within one image set, for 10 image set, each having a different epidermal thickness. All 10 image sets were used to create figure 8.2a, each one color-coded with its corresponding thickness value ( $d=0.02\text{ mm} - d=0.2\text{ mm}$ ). Figure 8.2b shows eigenvector 2 projection vs. blood volume for  $d=0.06\text{mm}$ , color-coded with  $d$ .

Figure 8.2c shows eigenvector 2 vs. blood oxygenation for  $d=0.06$  mm, color-coded with blood volume, where a high dependency on blood volume can be seen. The same relationships are shown in figure 8.2d-f for one image set with varying epidermal thickness of  $d=[0.02 \ 0.06 \ 0.10]$ mm. Figure 8.2f shows eigenvector 2 vs. blood oxygenation color-coded with blood volume. Results for eigenvector 1 (8.2a, d) show that blood volume can uniquely be extracted, if the epidermal thickness is known. Eigenvector 2 (8.2b-d, e-f) shows a dependency on blood volume as well as epidermal thickness.

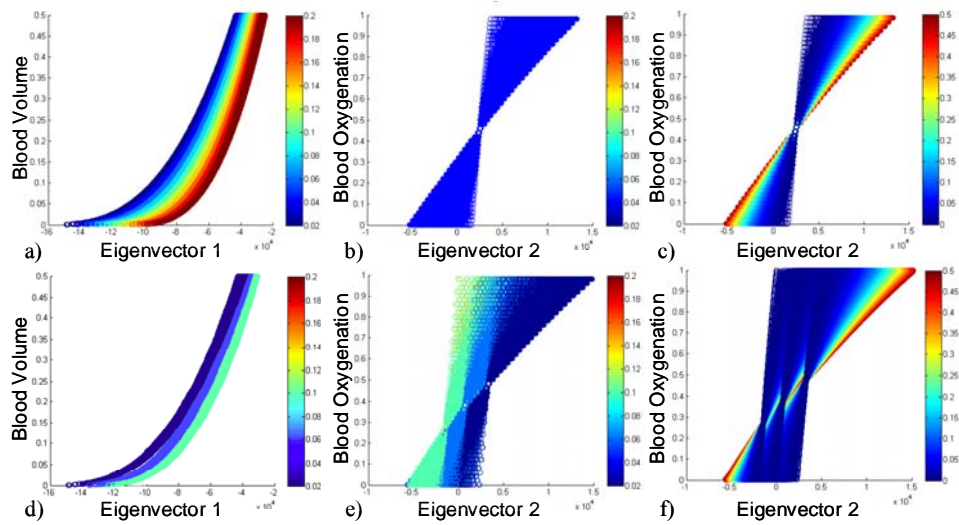


Fig. 8.2. Eigenvector 1 and 2 vs. blood volume and blood oxygenation, respectively. 8.2a-8.2c show results for a uniform thickness; 8.2d-f for spatially varying thickness. 8.2a-b and 8.2d-e show results color-coded with thickness  $d$ ; 8.2c and 8.2f are color-coded with blood volume, showing the dependence of eigenvector 2 on blood volume.

#### 8.4.2 PCA based reconstruction

In order to obtain quantitative results for blood volume and blood oxygenation from PCA results, the epidermal thickness as well as the blood volume dependence in eigenvector 2 need to be taken into account. Eigenvector 3 (not shown) showed a dependence on the epidermal thickness as well. This dependence was not unique, which made it impossible to assess the epidermal thickness directly. Since the epidermal thickness can not be assessed by the PCA results, prior information has to be obtained.

### 8.4.2.1 PCA based reconstruction of blood volume based on eigenvector 1

By assuming the epidermal thickness to be known, we could find a thickness dependent analytical expression, which converts eigenvector 1 into blood volume. The spatially varying thickness image sets were used for fitting. We applied curve fitting (Curve Fitting Toolbox, Matlab, Math Works, Natick, MA) to all eigenvector 1 pixels for a given thickness within the image and found the following dependence:

$$VDB^* = C_1 \cdot Y_1^3 + C_2 \cdot Y_1^2 + C_3 \cdot Y_1 + C_4, \quad (8.6)$$

where  $VDB^*=(vdb_1, \dots, vdb_n)$ , which is blood volume at each pixel based on PCA,  $Y_1=(y_{1,1}, \dots, y_{1,n})$ , which is the projection onto eigenvector 1 at each pixel. The coefficients of the cubic polynomial ( $C_1 - C_4$ ) were found to be thickness dependent and are given by cubic polynomials as well, with coefficients seen in table 2. The magnitude of the coefficients, which is as low as  $10^{-14}$ , can be explained by the magnitude of the data itself ( $\sim 10^5$ ), since the final values are laying between 0 and 1 (fractional percentage).

**Table 2. Coefficients for cubic polynomial for  $C_1-C_4$**

	$a_0$	$a_1$	$a_2$	$a_3$
<b>C<sub>1</sub></b>	$4.40 \times 10^{-14}$	$-4.13 \times 10^{-15}$	$1.63 \times 10^{-15}$	$1.04 \times 10^{-16}$
<b>C<sub>2</sub></b>	$9.19 \times 10^{-9}$	$-8.74 \times 10^{-10}$	$5.95 \times 10^{-10}$	$7.95 \times 10^{-11}$
<b>C<sub>3</sub></b>	$5.47 \times 10^{-4}$	$-9.05 \times 10^{-5}$	$5.50 \times 10^{-5}$	$1.65 \times 10^{-5}$
<b>C<sub>4</sub></b>	5.21	-1.67	0.27	1.05

The result of this PCA based reconstruction of blood volume can be seen in figure 8.3. Figure 8.3a shows the PCA based reconstruction of blood volume applied to all 10 images sets with uniform thickness; figure 8.3b applied to all spatially varying thicknesses. Data in figure 8.3 are color-coded with the corresponding thickness values and show all ten sets overlapping each other. The correlation between this calculated blood volume and real blood volume is linear, shows no longer a dependence on the thickness and makes predictions of blood volume possible with an error of less than 8% for blood volume values of 0.5.

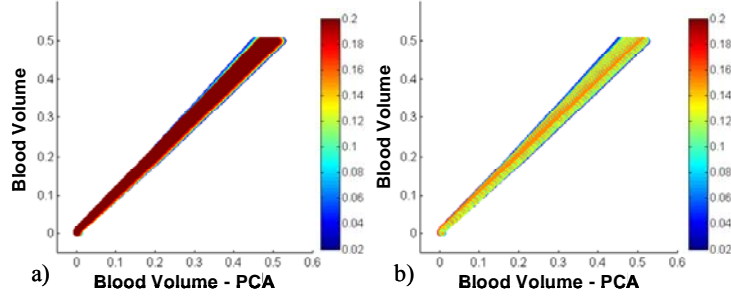


Fig. 8.3. PCA based reconstruction of blood volume vs. blood volume for all uniform d (a) and spatially varying d (b), with image sets overlapping each other. After correction, blood volume can be assessed within a maximum error of 8%, using eigenvector 1.

#### 8.4.2.2 PCA based reconstruction of blood oxygenation based on eigenvector 2

PCA based reconstruction for blood oxygenation based on eigenvector 2 was also based on the image sets with spatially varying thickness and then applied for the image sets with uniform distribution. The first step for converting eigenvector 2 into blood oxygenation values was division by eigenvector 1. This division was performed in order to align the ‘double cones’ seen in figure 8.2e and 8.2f along the y-axis direction. A linear relationship was found between  $Y_2/Y_1$  and blood oxygenation for a given blood volume and thickness value. This linear relationship can be written as:

$$VBOXY^* = A \cdot \frac{Y_2}{Y_1} + B \quad (8.6)$$

where  $VBOXY^* = (vboxy_1, \dots, vboxy_n)$ , which is blood oxygenation at each pixel based on PCA,  $Y_2 = (y_{2,1}, \dots, y_{2,n})$ , which is the projection along eigenvector 2 at each pixel,  $A = (a_1, \dots, a_n)$  and  $B = (b_1, \dots, b_n)$  are the slope and shift, respectively. By dividing eigenvector 2 by eigenvector 1, it was possible to remove the blood volume dependence in the data and extract blood oxygenation. The slope  $A$  was found to be blood volume dependent and thickness independent and can be seen in figure 8.4a for the image sets with spatially varying thickness vs. blood volume. After fitting against blood volume, the slope was found to be:

$$A = -6.27 \cdot VDB^{-0.35} + 5.99 \quad (8.7)$$

Since blood volume can be calculated based on eigenvector 1 with less than 8% error, the slope can be calculated based on eigenvector 1. The shift  $B$  was found to be dependent on blood volume as well as the thickness. Figure 8.4b shows the shift  $B$  vs. blood volume, where blue corresponds to the minimum, green to the middle, and red to the maximum thickness within one image set. The shift for the minimum thickness,  $B_{min}$ , in the image could therefore be fitted (shown in figure 8.4b – red) and written as:

$$B_{\min} = -S_1 \cdot VDB^{-S_2} + S_3 \quad (8.8)$$

where the coefficients  $S_1$ ,  $S_2$ ,  $S_3$  can be modeled by a linear dependence on thickness. This epidermal thickness dependence explains the remaining ‘widening’ of the shift of the minimum thickness (see inset in figure 8.4b - blue). These coefficients were found to be:

$$\begin{aligned} S_1 &= -0.22 \cdot d_{\min} - 0.13 \\ S_2 &= -0.04 \cdot d_{\min} - 0.34 \\ S_3 &= 0.14 \cdot d_{\min} + 0.47 \end{aligned} \quad (8.9)$$

where  $d_{\min}$  is the minimum thickness, which corresponds to  $d_1$  ( $d_4$ ) in table 1.

The relationship between the shift for the minimum thickness,  $B_{\min}$ , and the shift for the remaining thicknesses  $D=(d_1, \dots, d_n)$  was found to be linear and dependent on the difference between the minimum and remaining thickness. The shift  $B$  can thus be calculated by a linear equation with  $B_{\min}$ , given as:

$$B = S_4 \cdot B_{\min} + S_5 \quad (8.10)$$

where the coefficients  $S_4$  and  $S_5$  can be written as:

$$S_4 = -18.44 \cdot (D - d_{\min}) + 1.04; \quad S_5 = 6.25 \cdot (D - d_{\min}) - 0.01 \quad (8.11)$$

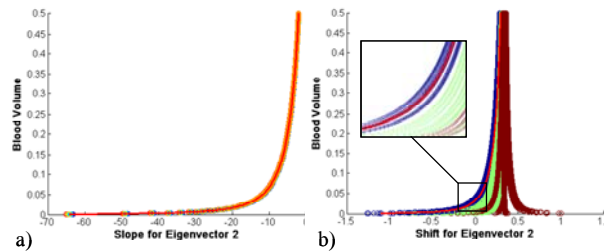


Fig. 8.4. Slope and shift of eigenvector 2. 8.4a. shows the slope A vs. blood volume, 8.4b. the shift B vs. blood volume.

The resulting blood oxygenation calculation based on equation 6 (PCA based reconstruction) vs. blood oxygenation can be seen in figure 8.5. Figure 8.5a shows PCA based reconstruction of blood oxygenation vs. real blood oxygenation for the spatially uniform thickness distribution, figure 8.5b for the spatially varying case. Again, all image sets within figure 8.5a and b are overlapping each other. Since the minimum thickness value turned out to be of importance for blood oxygenation calculation, the correction factors were evaluated on the third type of image sets as well, which have one pixel in the center of the image, which is smaller than the rest. Figure 8.5c shows the results for this set of images, showing a larger error compared to 8.5b. Figure 8.5d

shows the same data as in figure 8.5c, but split into subgroups, based on the difference between the smallest thickness and the next larger one. If the difference is small, the error is small as well. All graphs in figures 8.5 show data for pixels with blood volume  $> 0.04$ . If taking into account pixels of blood volume  $< 0.04$ , the error becomes twelve times as large.

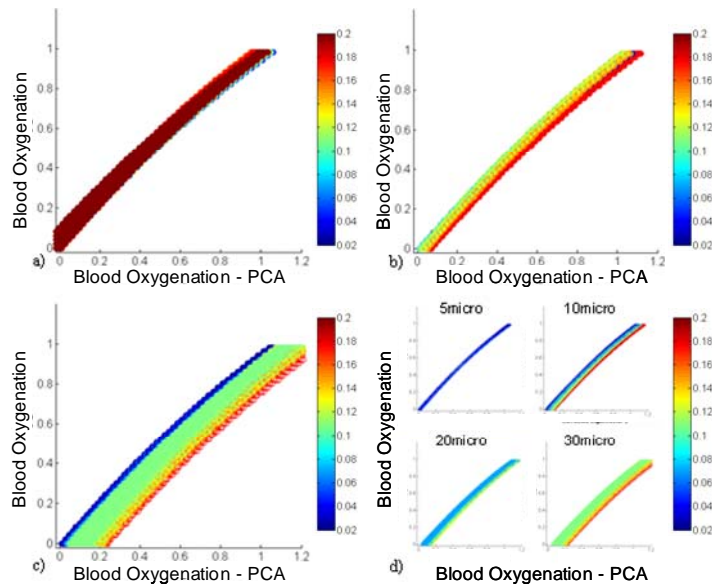


Fig. 8.5. PCA based reconstruction of blood oxygenation vs. blood oxygenation for uniform  $d$  (a), spatially varying  $d$  (b). If one pixel has a smaller thickness than the rest (c), there also is a dependence on the difference between the smallest thickness and the next bigger one (d). After correction, blood oxygenation can be assessed within  $< 10\%$  error, using eigenvector 2, if the difference between  $d_{min}$  and the next bigger thickness is  $< 20\mu\text{m}$ .

### 8.4.3 Thickness dependent error analysis

#### 8.4.3.1 Epidermal thickness dependent error in reconstruction

Error analysis for reconstruction of blood volume and oxygenation, if an epidermal thickness of  $d=0.06\text{mm}$  is assumed, which does not correspond to the actual thickness, can be seen in figure 8.6. The relative error is defined as the difference between real values minus reconstructed ones in fractional percentage. The error in blood volume (a) is color-coded with blood volume values and increases linearly with epidermal thickness. As expected, it is zero for the image set, which has actual thickness  $d=0.06\text{mm}$ , and as large as 15% for  $d=0.20\text{mm}$ .

The error in blood oxygenation (b) is color-coded with blood oxygenation. It was found to be blood oxygenation as well as blood volume dependent and to be as

large as 60% (for  $vdb=4\%$  and blood oxygenation 95%) for  $d=0.20\text{mm}$ . The error decreases with increasing blood volume values.

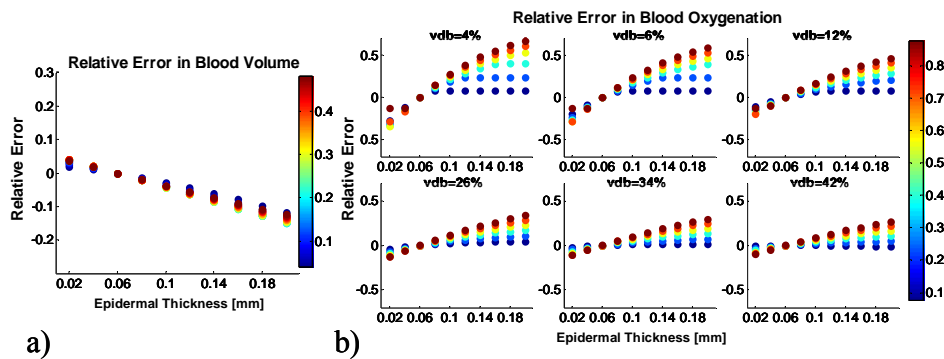


Fig. 8.6. Relative error in reconstruction. A constant epidermal thickness of  $d=0.06\text{mm}$  is assumed for calculations. The error in blood volume values is shown in (a), color-coded with blood volume. The error in blood oxygenation in dependence on blood volume is shown in (b), color-coded with blood oxygenation.

#### 8.4.3.2 Epidermal thickness dependent error in PCA based reconstruction

The errors in PCA based reconstruction of blood volume and blood oxygenation can be seen in figures 8.7 and 8.8. The procedure was the same as for the reconstruction analysis, which was assuming  $d = 0.06\text{mm}$  at each pixel. The error analysis in PCA based reconstruction was performed separately on image sets with a uniform thickness distribution within the image and spatially varying one. Figure 8.7 shows the relative error in PCA based reconstruction of blood volume and oxygenation for uniform epidermal thicknesses image sets. Figure 8.7a shows the results for blood volume, where the error linearly increases with thickness. The error ranges from 3% ( $d=0.02\text{mm}$ ) to 15% ( $d=0.2\text{mm}$ ) blood volume. Figure 8.7b shows the error in blood oxygenation as a function of blood volume. For a given blood volume value, the error also depends on oxygenation. For larger blood volume values, this dependency decreases and thus the error in oxygenation decreases. It shall be noted that the error at  $d=0.06\text{mm}$  is not zero, since the PCA based reconstruction has an uncertainty, as shown in figures 8.3 and 8.5.

Figure 8.8 shows the relative error for spatially varying epidermal thicknesses. Blood volume does not show a significant difference in error compared to the uniform case. Blood oxygenation errors show the same trend as for uniform thicknesses, but increased values in error. It is important to note that the error in PCA based reconstruction is symmetric around zero, whereas the error in reconstruction is not. The

values for the reconstruction error in oxygenation (figure 8.6) are therefore larger than the PCA based reconstruction error. This important finding indicates that the PCA based reconstruction is less sensitive to epidermal thickness variations.

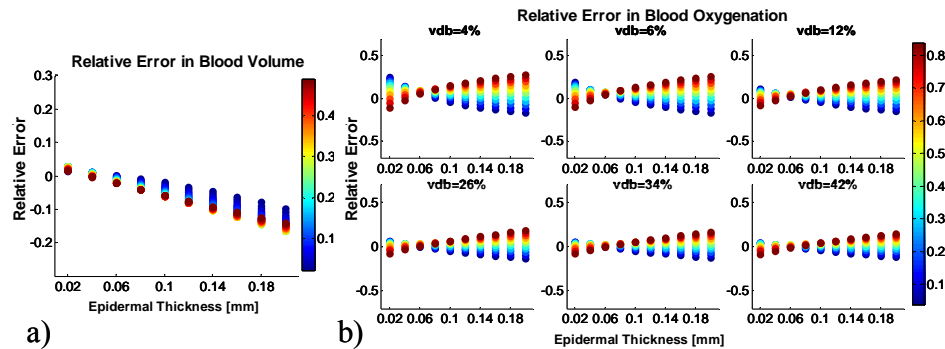


Fig. 8.7. Relative error in PCA based reconstruction for the uniform epidermal thickness set. A constant epidermal thickness of  $d=0.06\text{mm}$  is assumed for calculations. The error in blood volume values is shown in (a), color-coded with blood volume. The error in blood oxygenation in dependence on blood volume is shown in (b), color-coded with blood oxygenation.

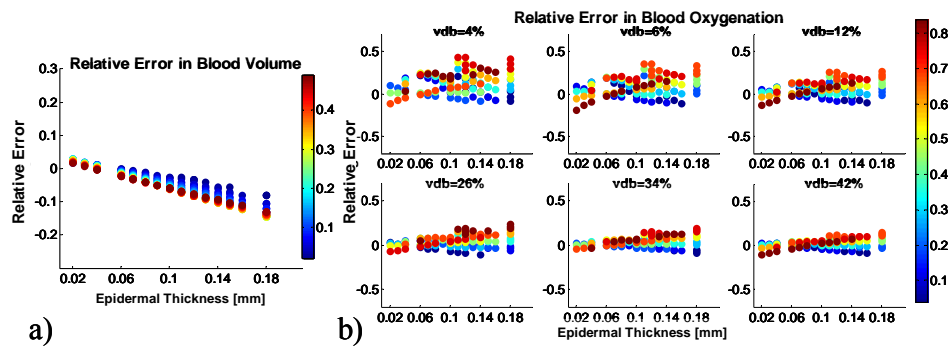


Fig. 8.8. Relative error in PCA based reconstruction for spatially varying epidermal thickness. For description see figure 8.7.

## 8.5 Discussion

Diffuse multi-spectral imaging in the near-infrared wavelength range has previously been used to assess blood volume and oxygenation in healthy and diseased skin [Asai et al., 2006; Attas et al., 2001; Cuccia et al., 2009; Jacques et al., 2002; Kainerstorfer et al., 2009c; Kainerstorfer et al., 2010c; Kainerstorfer J. M. et al., 2010; Mantis & Zonios, 2009; Tseng et al., 2009; Vogel et al., 2007]. Those parameters are of particular interest for assessing the metabolic state of skin-lesions for treatment follow-up, since they function as a measure for angiogenic processes and metabolic state of a tumor. Generally those parameters are being assessed by fitting the intensity data to an

analytical or numerical model of photon migration, with prior assumptions being made. If a two layered analytical skin model is being used, the epidermal thickness is being assumed to be known, and thus is susceptible to errors. Quantitative reconstruction thus depends on the assumptions made and in general is computationally expensive, therefore time consuming.

Principal Component Analysis (PCA) has been proposed as an alternative tool for extracting information from reflectance imaging data from the skin [Cheng et al., 2008; Du & Fowler, 2008; Fadzil et al., 2009; Hance et al., 1996; Kainerstorfer et al., 2010c; Kainerstorfer J. M. et al., 2010; Umbaugh et al., 1993]. The biggest advantage of PCA lies in the speed of computation, which provides information in real-time, as well as in its model independence. Tsumura et al. [Tsumura et al., 1999; Umbaugh et al., 1993] extracted blood and melanin when applying PCA to RGB imaging data. Those results were qualitative though and no attempt was done to convert the results into quantitative parameters. We have shown previously [Kainerstorfer et al., 2010c; Kainerstorfer J. M. et al., 2010] that PCA applied to multi-spectral imaging data from the skin in the wavelength range between 750nm and 850nm can be used for blood volume and oxygenation extraction and mapping. We showed that the data projected onto the first eigenvector follows the spatial and temporal behavior of blood volume and the projection onto the second eigenvector the one of oxygenation. Those findings though were also qualitative.

We created multiple numerical phantoms with given blood volume and blood oxygenation distributions and varying epidermal thickness. Since PCA is performed on 2D images and thus takes spatial variations into account, the epidermal thickness was chosen to be uniform in one set and spatially varying in the others. PCA was applied to each image set of those simulations and the relationship between eigenvector 1 and blood volume as well as eigenvector 2 and blood oxygenation was being investigated (figure 8.2). We found that PCA can decouple the dependence of blood volume and oxygenation, making eigenvector 1 only blood volume and thickness dependent. Eigenvector 2 was found to be blood volume, oxygenation, and thickness dependent. Having found those dependencies and assuming prior knowledge about the underlying structure (epidermal thickness), PCA results could be converted into actual blood volume and oxygenation values (figure 8.3 and 8.5), resulting in a PCA based reconstruction.

For blood oxygenation calculation with this PCA based reconstruction, we found that the smallest thickness within the image becomes an important parameter. If one single pixel in the image has a thickness, which is more than  $20\mu\text{m}$  smaller than the next bigger one, the error becomes significantly larger. It shall be noted that this is a scenario, which is not to be expected for in vivo imaging, since it is highly unlikely to find an outlier in the epidermal thickness. Such a case could potentially only be found based on experimental errors of extracting the thickness from structural images. We further found that blood oxygenation could not reliably be extracted for blood volume values smaller than 4%. This is to be expected though, since the sensitivity is decreased for small blood volume values. For Blood volume values larger than 4%, blood oxygenation could be extracted within 10% error.

We further evaluated the error in reconstruction, using the analytical two layered model, if the epidermal thickness is not known. The error in reconstruction of blood volume and oxygenation, using a two-layered model as well as PCA based, was evaluated assuming an epidermal thickness of  $d=0.06$ , which is a representative literature value for the lower arm [Mogensen et al., 2008; Whitton & Everall, 1973]. For the two layered reconstruction, we found that the error in blood volume increases linearly with error in epidermal thickness assumption (figure 8.6a). If the difference between assumed and true value is  $<0.06\text{mm}$ , the error is moderately low ( $<6\%$  blood volume). Blood volume can thus still be reconstructed within 6% error, is therefore not very sensitive to epidermal thickness variations. In comparison, the error in oxygenation (figure 8.6b), which is not linear with thickness, can be as large as 40% if the assumed epidermal thickness varies from the real value by  $0.06\text{mm}$ .

Using PCA based reconstruction, the error in calculations, if an epidermal thickness of  $d=0.06\text{mm}$  is assumed, was evaluated using image sets with uniform and spatially varying epidermal thickness distribution, since PCA is being performed on the 2D images, in comparison to the two layered reconstruction, which is performed pixel wise. PCA based reconstruction showed the same trend and magnitude of errors in blood volume (figure 8.7a and 8.8a) as the error using reconstruction with a two layered model. The error in oxygenation was found to be smaller than for the reconstruction results, thus making PCA based reconstruction less sensitive to epidermal thickness variations. It is important to point out that the error behavior with epidermal thickness is not the same between PCA based reconstruction and two layered reconstruction. The error in oxygenation, using PCA based reconstruction, was found to be symmetric on

zero, whereas the error for two layered reconstruction was increasing for all oxygenation values. Since knowledge about the epidermal thickness is of importance, we propose multi-spectral imaging on the skin in combination with Optical Coherence Tomography (OCT) on the same area for obtaining spatial priors.

## 8.6 Conclusion

We introduced a novel approach of obtaining blood volume and oxygenation values using multi-spectral imaging data from skin by applying PCA. We have shown previously that qualitative results can be obtained and here we are showing that those results can be converted into quantitative ones, using a PCA based reconstruction algorithm. We created numerical phantoms based on an analytical two layered skin model with varying blood volume and oxygenation, and applied PCA. We also investigated structural changes, namely changes in the epidermal thickness, and its influence on PCA results. We were able to find analytical expressions for converting the unitless data from PCA into actual blood volume and blood oxygenation values, if the epidermal thickness is known. With this PCA based reconstruction, blood volume and blood oxygenation could be extracted within 8% error, if the epidermal thickness is known. The error for reconstruction and PCA based reconstruction if the epidermal thickness is not known was also calculated, assuming  $d=0.06\text{mm}$  for all image sets. This error analysis revealed that the underlying thickness has to be known, otherwise the error in blood oxygenation can be as large as 60%, for a difference of 0.14mm between actual thickness and assumed one. If the epidermal thickness is known, this PCA based reconstruction becomes a promising tool for clinical applications if quantitative assessment of blood volume and oxygenation is desired, providing results in real time.

**Acknowledgements:** The research was funded by the Intramural Research Program of the Eunice Kennedy Shriver National Institute of Child Health and Human Development. The Graduate Partnership Program at the National Institutes of Health and the Department of Physics at the University of Vienna in Austria are also acknowledged.

## Chapter 9

# Original paper 4 – In vivo validation of principal component models with spatial priors for quantification of multi spectral images

### 9.1 Abstract

We are evaluating a Principal Component Analysis (PCA) based reconstruction algorithm for extracting blood volume and oxygenation values from multi-spectral images. The method is applied to *in vivo* multi-spectral images from a healthy volunteer's lower forearm. The imaging data are complemented by images of the same area using Optical Coherence Tomography (OCT) in order to measure the epidermal thickness, which was used as prior information for the PCA based reconstruction. Reconstruction of the imaging results using a two layered analytical skin model was compared to PCA based reconstruction results. A point wise correlation was found, showing the proof of principle of using PCA based reconstruction for blood volume and oxygenation extraction.

### 9.2 Introduction

It is well recognized that since the primary absorbing component of near infrared light in tissues is hemoglobin, diffuse multi-spectral imaging can be used for mapping of blood volume and blood oxygenation values. This method has already found its application in the clinic, successfully assessing parameters for healthy and diseased skin [Attas et al., 2001; Jacques et al., 2002; Mantis & Zonios, 2009; Miyamae et al., 2008; Tseng et al., 2009; Vogel et al., 2007; Zakian et al., 2008]. If quantitative assessment of those is desired, a mathematical model has to be used, which describes light tissue interaction. Based on such a model, which can be either an analytical, numerical, or

stochastic model, conventional reconstruction is usually performed in a pixel by pixel fashion.

Skin models are usually based on multiple layers, which, dependent on the complexity of the model used, can vary from two to six layers [Kirillin et al., 2007; Mantis & Zonios, 2009; Vogel et al., 2007; Zagaynova et al., 2008]. For a two layered case, the first layer describes the epidermis and the second one the dermis. In the near infrared spectrum (below 900nm), absorption and scattering properties in the epidermis are based on melanin and in the dermis on hemoglobin. Knowing the underlying structures, in particular the epidermal thickness, becomes inherently important.

All currently available pixel wise reconstruction algorithms are time consuming, if the image size is large, thus hindering the clinical translation. Principal Component Analysis (PCA) has previously been described as an alternative to model based reconstruction [Cheng et al., 2008; Fadzil et al., 2009; Hance et al., 1996; Kainerstorfer et al., 2010c; Kainerstorfer J. M. et al., 2010; Nugroho et al., 2007; Tsumura et al., 1999; Umbaugh et al., 1993], since PCA is computationally inexpensive, thus providing results in real time. Using PCA for extracting blood and melanin values has been proposed by Tsumura et al. [Tsumura et al., 1999], showing that skin color in digital RGB images can be described by attributing melanin and blood to the first two principal components. Fadzil et al. [Fadzil et al., 2009; Nugroho et al., 2007] applied PCA and Independent Component Analysis (ICA) to RGB images for extraction of blood and melanin values in vitiligo lesions to qualitatively evaluate the skin re-pigmentation progression. Our group has shown previously [Kainerstorfer et al., 2010c] that PCA applied to multi-spectral images from the skin in the wavelength range between 750nm and 850nm can be used for mapping blood volume and blood oxygenation. The results obtained from PCA are qualitative though and do not provide actual blood volume and oxygenation values. We have recently employed [Kainerstorfer et al.] numerical phantoms to test the ability of PCA applied to multi-spectral images to provide concentrations, thus making a PCA based reconstruction possible, if the epidermal thickness is known.

The aim of this is to validate the PCA based reconstruction on *in vivo* data, correlating the reconstruction algorithm and PCA based reconstruction, using the epidermal thickness, obtained by Optical Coherence Tomography (OCT), as spatial priors. OCT is a powerful imaging technique [Huang et al., 1991b], which provides structural information of the sample imaged with a resolution of a few micrometers. The

basics and an overview of this technique can be found in references [Drexler & Fujimoto, 2008; Fercher et al., 2003b]. OCT has been applied to the skin previously and it has been shown that extraction of the epidermal thickness was possible [Crowther et al., 2008; Mogensen et al., 2008; Zakharov et al., 2010].

We describe *in vivo* results from a healthy volunteer's lower forearm, which was imaged with multi-spectral imaging as well as OCT. Experiments with OCT allowed us to image the epidermis and thus extracting the thickness point by point. We then applied the reconstruction algorithm as well as PCA based reconstruction, taking the epidermal thickness for each pixel into account. Finally we show the quantitative match between reconstructed and PCA based reconstructed blood volume, as well as blood oxygenation. We demonstrate that knowing the underlying structures of the sample imaged is important for both reconstruction and PCA based reconstruction. We also demonstrate that PCA based reconstruction can indeed be used as a quantitative tool for blood volume and oxygenation extraction, with the major benefit of obtaining results in real time.

## **9.3 Materials and Methods**

### **9.3.1 Instrumentation**

Diffuse multi-spectral images as well as OCT images were acquired from the lower forearm. The diffuse multi-spectral imaging system used in this work has been described in detail in [Vogel et al., 2007] and shall not be described here. OCT provides structural information of the sample imaged with a resolution of a few micrometers. The setup of the spectral domain OCT [Fercher et al., 1995b] system is fiber based with a superluminescence diode light source (DenseLight, Singapore) emitting at  $\lambda_0=1300$  nm with  $\Delta\lambda = 130$  nm and output power 24mW. The interferometer is based on a Michelson interferometer with a 50/50 fiber coupler. The beam is scanned across the sample via an x-y galvo-scanner, where the beam is focused onto the sample surface by an achromatic lens with focal length of 35 mm. Optical power on the sample was  $\sim 5$ mW. A variable neutral density filter was used in the reference arm in order to operate the spectrometer camera close to the saturation limit. After light is being backscattered from the skin, it is recombined with the reference arm light at the interferometer exit and detected by the

spectrometer. At the spectrometer light is being collimated and directed onto a diffraction grating (Wasatch, USA) with 1100 lines/mm. The dispersed spectrum is focused by an achromatic lens of 100 mm focal length and recorded with a 1024 element InGaAs line scan camera (Goodrich, Princeton, NJ).

For in vivo measurements, the A-scan rate was set to 10 kHz (exposure time 55 $\mu$ s) and B-scans were acquired with 15 f/s. A paper mask, seen in figure 9.1, was placed on the forearm, which was composed of an outer square of 6x6 cm<sup>2</sup> (pink in figure 9.1b and c) and 16 inner squares of 1x1 cm<sup>2</sup>, aligned in a grid pattern. Twelve of those squares within the mask were imaged, resulting in 12 3D data sets of 500x500x512 pixels (x-y-z direction), which correspond to 14x14x2.5mm<sup>3</sup>. The area in x and y direction was chosen to contain part of the mask as well, in order to align the measured OCT images with multi-spectral images. Refractive index matching gel was not used, since it would have biased the multi-spectral images obtained from the same area.

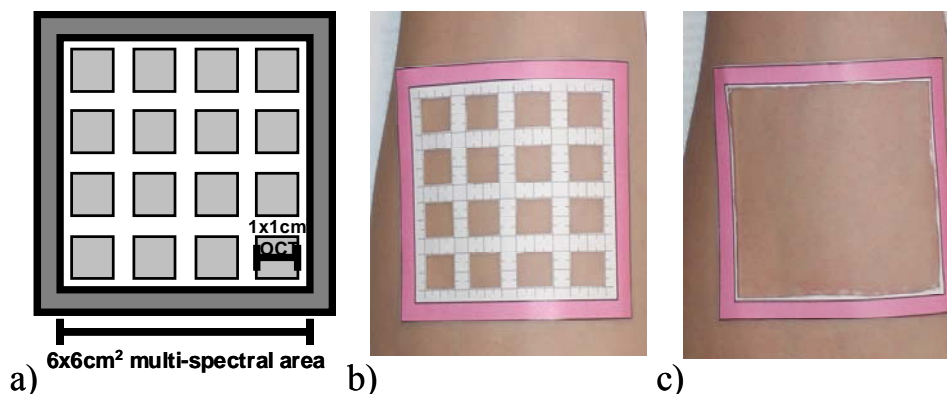


Fig. 9.1. Paper mask placed on the forearm. The small squares were imaged with OCT first and the outer square was imaged with the multi-spectral imaging system. A cartoon of the mask is seen in (a), the mask on the forearm for OCT imaging in (b), and for multi-spectral imaging in (c).

After acquiring the OCT images, the inner part of the grid was removed, leaving only the outer square (figure 9.1c), which was imaged by the multi-spectral imaging system. For multi-spectral images, the upper arm was occluded by a pressure cuff with 180mmHg pressure. This amount of pressure was chosen to achieve arterial occlusion and the pressure lasted for 5min. Multi-spectral images were taken every 30 seconds before occlusion, during occlusion and for 5 minutes afterwards, resulting in 26 time points in total. Occlusion experiments were chosen as the behavior of blood volume and blood oxygenation over time is well known, which is ischemia during, and reactive

hyperemia after occlusion [Cuccia et al., 2009; Kainerstorfer et al., 2009c; Kainerstorfer et al., 2010c; Merschbrock et al., 1994; Tseng et al., 2009].

All volunteers signed a consent form approved by the Institutional Review Board of the Eunice Kennedy Shriver National Institute of Child Health and Human Development under the protocol number 08-CH-0001.

### **9.3.2 Skin model based and PCA based reconstruction**

The skin model used for reconstruction of blood volume and oxygenation was described previously [Kainerstorfer et al., 2009c; Kainerstorfer et al., 2010b; Kainerstorfer et al., 2010c; Vogel et al., 2007] and will from now on be referred to as conventional reconstruction, in comparison to PCA based reconstruction. The first layer is the melanin containing epidermis, which can be described based on Lambert's Law. The second layer is the blood containing dermis, which can be described based on an analytical solution of photon migration in turbid media [Gandjbakhche & Weiss, 1995a], based on random walk theory.

PCA based reconstruction has been presented previously in [Kainerstorfer et al.] and only the major points are repeated here. As a first step, PCA is being applied to the image set of three wavelength images. PCA [Pearson, 1901] linearly transforms the imaging data into an orthogonal coordinate system whose axes correspond to the eigenvectors in the data. This transformed data, which is unitless, is then used for blood volume and oxygenation calculation. PCA based reconstruction is based on analytical expressions for converting eigenvector 1 into blood volume and eigenvector 2 into blood oxygenation, both as a function of the epidermal thickness.

For in vivo calculation of blood volume and oxygenation, multi-spectral images from the occlusion experiment were used. Preprocessing of the data included spectral and spatial illumination artifact removal [Vogel et al., 2007], rigid body registration for motion artifact removal, as well as curvature correction [Kainerstorfer et al., 2010b]. Conventional reconstruction as well as PCA based reconstruction was performed, using the epidermal thickness, measured by OCT, as spatial priors.

Epidermal thickness segmentation of the OCT images was performed on B-scans on linear scale. Before segmentation was performed, a moving mean-filter of 5x5 pixels was applied. The skin surface was found by moving along the z-direction, finding the first pixel larger than a user defined threshold. In order to remove outliers, pixel

positions which were further away than 3 pixels from the standard deviation over the two neighboring ones on either side, were removed. For smoothing the surface, the missing points were then interpolated based on nearest neighbor interpolation. For finding the epidermis-dermis boundary, the maximum intensity value below the skin surface in z-direction was found. Again, in order to avoid outliers, pixels which were further away than 5 pixels from the standard deviation over the two neighboring ones were removed and smoothing was performed with interpolation. A refractive index of  $n=1.42$  was used to convert optical thickness into geometric one, thus obtaining the actual epidermal thickness values in millimeters.

## 9.4 Results

The epidermal thickness was extracted based on 3D OCT image sets of the lower forearm. Figure 9.2a shows a representative B-scan through part of the arm in logarithmic scale with image area of  $14 \times 1.3 \text{ mm}^2$ . The area of the arm is surrounded by the paper mask, which is seen at the left and right outer part of the image. The red lines indicate the surface of the skin as well as the boundary to the dermal layer. The OCT system is not artifact free and a ghost image can also be seen on top of the skin surface. A representative A-scan can be seen in figure 9.2b, plotted in linear scale. The skin surface and the epidermal-dermal boundary are indicated with the red dots lines. Figure 9.2c shows extracted epidermal thickness for the image area of  $14 \times 14 \text{ mm}^2$ , where the blue area is the paper mask.

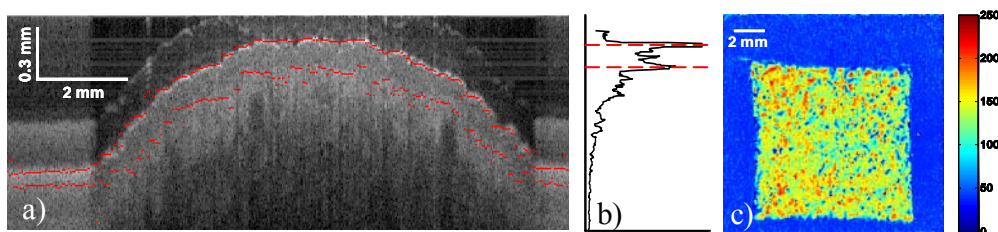


Fig. 9.2. B-scan (a), A-scan (b), and extracted epidermal thickness (c). A typical section of the forearm is shown in a, where the red lines indicate the surface of the skin as well as the boundary to the dermal layer. A representative A-scan in linear scale is seen in b. The extracted epidermal thickness over an area of  $14 \text{ mm} \times 14 \text{ mm}$  is shown in c. The values of the color scale are given in  $\mu\text{m}$ .

The average thickness of each  $1 \times 1 \text{ cm}^2$  area can be seen in figure 9.3, with errorbars given by the standard deviation over each area. The overall thickness does not

vary significantly over the 12 areas measured, with a mean thickness of  $115.2\mu\text{m} \pm 32\mu\text{m}$ . Taking pixel wise measures of epidermal thickness into account, we performed conventional reconstruction of blood volume and oxygenation as well as PCA based reconstruction. After downsampling the OCT images to match the pixel size of multi-spectral ( $400 \times 400 \mu\text{m}^2$ ), registration was performed. Since only a subset of the data was used, which was based on the four center  $1 \times 1 \text{ cm}^2$  squares, the number of pixels was reduced significantly.

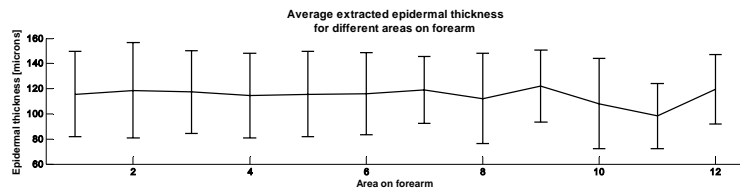


Fig. 9.3. Average and standard deviation of extracted epidermal thickness over twelve  $1 \times 1 \text{ cm}^2$  areas on the forearm of a healthy volunteer.

Conventional reconstruction of blood volume and oxygenation was performed first, which includes calculation of the scaling factor  $S$ . The found scaling factor was  $S = 1.24 \cdot 10^5$ , which is larger than the assumed one for PCA based reconstruction. For PCA based reconstruction, the scaling factor was set to  $S = 9.26 \cdot 10^4$  [Kainerstorfer et al.], which corresponds to the average value of several subjects with 300ms exposure time. Therefore, the intensity images had to be scaled to  $S = 9.26 \cdot 10^4$  before PCA was performed. Since we have shown previously [Kainerstorfer et al., 2010c] that the number of pixels is important for reliable performance of PCA, data transformation with PCA was done with eigenvectors found previously on a different data set from the same subject. After PCA was performed, the PCA based reconstruction was applied.

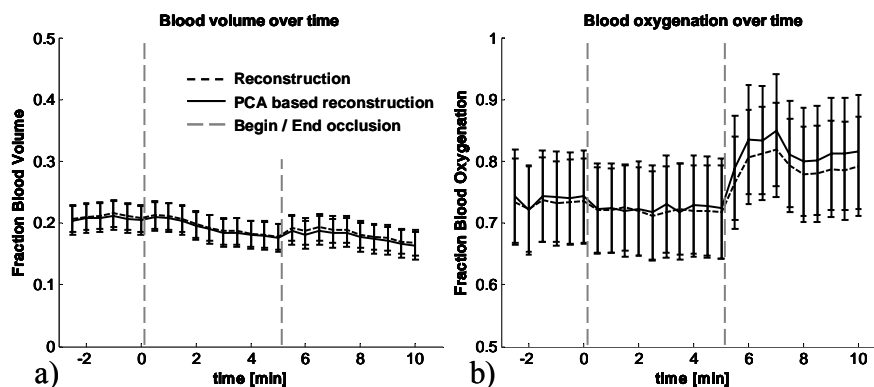


Fig. 9.4. Blood volume (a) and oxygenation (b) over time, extracted with conventional reconstruction and PCA based reconstruction. Begin and end of occlusion is indicated by the vertical lines at time  $t=0\text{min}$  and  $t=5\text{min}$ .

Blood volume and oxygenation was extracted with both methods and the comparison over time can be seen in figure 9.4. For each time point, the average value over the entire image area was taken and data is shown with standard deviation over all pixels. Blood volume (figure 9.4a) and oxygenation (figure 9.4b) follow the expected temporal course for occlusion, which is constant for blood volume, drop in oxygen during occlusion (ischemia) and overshoot after (hyperemia).

The point wise correlation between conventional reconstruction results and PCA based reconstruction results can be seen in figure 9.5. Data was taken from all time points, before, during, and after occlusion. The correlation between reconstructed blood volume and PCA based reconstructed blood volume, seen in figure 9.5a, shows a pixel wise correspondence. The correlation between reconstructed blood oxygenation and PCA based reconstruction results can be seen in figure 9.5b. The remaining error in correlation can be explained by uncertainty in extraction of the epidermal thickness.

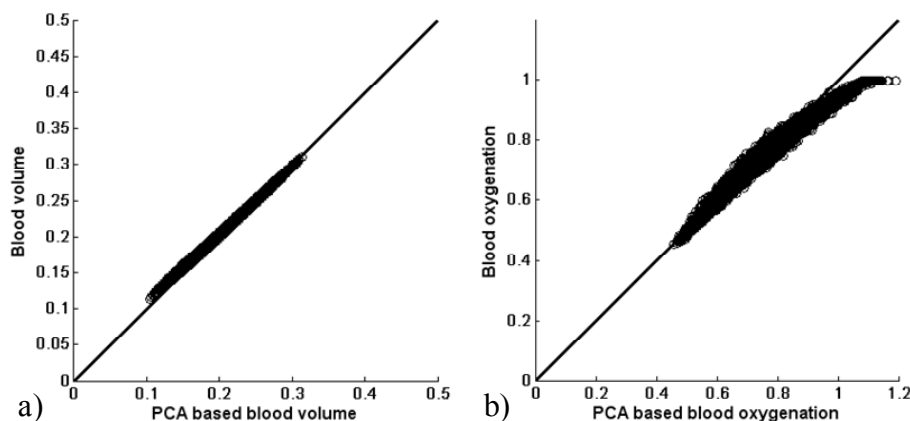


Fig. 9.5. In vivo results for blood volume (a) and blood oxygenation (b), showing a pixel wise correspondence between conventional reconstruction and PCA based reconstruction.

## 9.5 Discussion

The PCA based reconstruction model [Kainerstorfer et al.] uses PCA as a first step and conversion into actual blood volume and oxygenation values as a second step. Results using numerical phantoms indicated that, assuming the epidermal thickness to be known, blood volume and oxygenation can be extracted with 8% error. The focus of this work was to validate this PCA based reconstruction using *in vivo* data involving OCT measurements on the lower forearm of a healthy volunteer accompanied by multi-

spectral images from the same area. The multi-spectral images were acquired before, during, and after arterial occlusion of the upper arm.

The temporal comparison between conventional reconstruction results and PCA based reconstruction results (figure 9.4) was performed by averaging over all pixels per time point. Blood volume and oxygenation were found to follow the expected temporal course for arterial occlusion. No significant difference was found between conventional reconstruction and PCA based reconstruction, confirming the validity of PCA based reconstruction. The average blood oxygenation values were found to not significantly decrease during occlusion. This can be explained by averaging over all pixels, which include blood vessels as well as surrounding tissue. We were not able to isolate the blood vessels in the image, but found that the temporal behavior varies considerably between pixels and several of them showing the expected ischemic behavior.

We also showed a pixel wise correlation between blood volume and converted PCA results, as well as a good correlation, but blurrier, for blood oxygenation (figure 9.5). The remaining uncertainty in oxygenation values might be attributed to the epidermal thickness extraction. The algorithm used is based on thresholding of intensity values, rather than more sophisticated methods, leading to uncertainties in extraction. This uncertainty leads to two effects, which are shifting of oxygenation values and blurring of the correlation between conventional reconstruction and PCA based reconstruction. This effect can also explain blood oxygenation values larger than 100%, which clearly is erroneous. It shall further be noted that the scaling factor had to be calculated first by the reconstruction algorithm in order to scale the data for PCA. Since the scaling factor is related to the light illuminating the sample, this calculation is not needed if the incident light intensity is measured. Future work will include this additional step in order to avoid reconstruction at all. Additionally it shall be mentioned that the melanin content has been assumed 8% for PCA conversion. In order to further generalize the PCA results, melanin will have to be taken into account.

Having demonstrated the proof of principle of using PCA based reconstruction in combination with OCT to obtain quantitative blood volume and blood oxygenation values, future work will include changes in the multi-spectral setup to measure the incident light, acquiring data from a greater number of healthy volunteers, as well as imaging patients with skin surface tumors. Especially for imaging skin tumors, prior knowledge of the underlying structure is important since the structural conformation

often differs from healthy skin. Having a near real-time imaging tool, multiple skin lesions could be imaged and results interpreted instantly.

## 9.6 Conclusion

We introduced a novel approach of obtaining blood volume and oxygenation values using multi-spectral images from the skin by applying a PCA based reconstruction algorithm. In order to validate the PCA based reconstruction on in vivo data, OCT and multi-spectral measurements on the lower forearm of a healthy volunteer undergoing arterial occlusion have been performed. OCT was used to extract the epidermal thickness, which was used as prior information for conventional reconstruction and PCA based reconstruction. We showed the correspondence between reconstruction and PCA based reconstruction for temporal behavior of blood volume and oxygenation as well as pixel wise. We were able to find a linear correlation between conventional reconstruction and PCA based reconstruction, making it possible to use PCA for quantitative assessment of blood volume and oxygenation. Since PCA can be performed in real time, it is a promising tool for clinical evaluation of skin malignancies.

**Acknowledgements:** The research was funded by the Intramural Research Program of the Eunice Kennedy Shriver National Institute of Child Health and Human Development. The Graduate Partnership Program at the National Institutes of Health and the Department of Physics at the University of Vienna in Austria are also acknowledged.

## Conclusion

The objectives of this dissertation were to devise novel methodologies and design instruments for quantitative functional characterization of skin. The imaging modalities used in this work were diffuse multi-spectral imaging for blood volume and blood oxygenation assessment in the skin as well as Optical Coherence Tomography (OCT) for structural imaging. In order to advance those techniques into clinical routines for skin imaging, challenges in design development and data analysis have to be overcome. The challenges concentrated on in this thesis were the transition from qualitative to quantitative extraction of blood volume and blood oxygenation values, as well as their real time reconstruction.

The first task in overcoming those challenges was to take the shape of the object imaged into account. Calculation of blood volume and blood oxygenation from multi-spectral data is based on the assumption that the object is flat, which usually is not the case for in vivo imaging, since the human body is not flat. The curvature correction algorithm developed in this work extracts the influence of the shape on reflected intensity distributions, without the necessity of knowing the shape and without acquiring additional images. The algorithm is based on fitting the intensity distribution caused by the shape and removing this information from the data, leaving only physiologically relevant information in the images. The biggest advantages of pursuing this curve fitting method are that no additional data has to be obtained, thus not adding time to the measurement, and that the spectral features are retained, allowing extraction of blood volume and blood oxygenation values. This method was applied to data from healthy and diseased skin, and it was shown that chromophore distributions can be reconstructed reliably and also making it possible to gain spatial information of those.

Obtaining results of blood volume and oxygenation distributions in real time was the next step. Principal Component Analysis (PCA) was introduced as an analysis tool applied to multi-spectral data. The reason for this was that PCA can be performed in real time, compared to model based reconstruction algorithms. It was shown that the first principal component corresponds to blood volume, the second to blood oxygenation, both of them at least qualitatively. Without removing the curvature artifact, the first component corresponded to curvature biased intensity. PCA was

applied to data from healthy and diseased skin and the results compared to reconstructed blood volume and oxygenation values. The spatial and temporal behavior of PCA results qualitatively matched the reconstructed ones, but a subject dependent shift was also observed.

In order to develop a real time quantitative analysis tool using PCA, simulations of multi-spectral reflectance data were performed and PCA was applied to those numerical phantoms. The numerical phantoms were based on an analytical two layered skin model, where the spatial distributions of blood volume and oxygenation, as well as the first layer, which is the epidermis thickness, were varied. When applying PCA to this data, it was found that the first eigenvector corresponds to blood volume, but is dependent on the epidermal thickness. The second eigenvector was found to be oxygenation and thickness dependent. It also showed a dependence on blood volume. The thickness dependence found may explain the subject specific shift in the data described above. Assuming the thickness to be known, analytical expressions could be found, which convert eigenvector 1 and 2 into quantitative blood volume and oxygenation values.

Since the epidermal thickness was found to be an important parameter in PCA based reconstruction of blood volume and oxygenation, in vivo validation of this tool was performed by measuring the epidermal thickness by OCT. Having gained structural information by OCT, quantitative blood volume and oxygenation could be extracted in real time.

Having developed an algorithm for curvature artifact removal as well as a real time analysis tool, multi-spectral imaging has great potential to find its place permanently in clinical routines. Since relevant information, such as blood volume and oxygenation can be assessed in a non-invasive fashion, accurately, and in real time, improvement of this technology represents an important advance towards several clinical applications, such as skin tumor diagnosis and treatment follow up.

Remaining challenges and tasks for future work include the actual transition of real time imaging into clinical settings. The PCA based reconstruction introduced here has proven to have great potential, but has yet to be implemented in a real time imaging tool. Additionally, in this work OCT has been used for measuring structural changes in order to improve multi-spectral results, but has not been utilized as a diagnostic tool by itself. Multi-modality imaging was thus not fully explored. Combining functional characteristics with structural conformation could potentially have great impact on

clinical usage. One example is skin tumors, where information about the metabolic state as well size of the tumor could lead to enhanced treatment follow up and potentially diagnostics. Combining those two modalities in an advanced matter, hence gaining greater insight in disease progression, can have great potential on defining and altering the chosen treatment course for malignancies.



## Bibliography

- Andersen, P. H. & Bjerring, P. (1990a) Noninvasive computerized analysis of skin chromophores in vivo by reflectance spectroscopy. *Photodermatol.Photoimmunol.Photomed.*, **7**, 249-257.
- Andersen, P. H. & Bjerring, P. (1990b) Spectral reflectance of human skin in vivo. *Photodermatol.Photoimmunol.Photomed.*, **7**, 5-12.
- Anderson, R. R. & Parrish, J. A. (1981) The optics of human skin. *J Invest Dermatol.*, **77**, 13-19.
- Archambeau JO, P. R., Wasserman T. (1995) Pathophysiology of irradiated skin and breast. *Int J Radiat Oncol Biol Phys.* , **31**, 1171-85.
- Arimoto, H. (2006) Multispectral polarization imaging for observing blood oxygen saturation in skin tissue. *Appl Spectrosc*, **60**, 459-64.
- Arimoto, H. (2007) Estimation of water content distribution in the skin using dualband polarization imaging. *Skin Res Technol*, **13**, 49-54.
- Arridge, S. R. & Hebden, J. C. (1997) Optical imaging in medicine: II. Modelling and reconstruction. *Phys. Med. Biol.*, **42**, 841.
- Asai, K., Sumiyama, Y., Watanabe, M. & Aizawa, K. (2006) Tumor viability using real-time spectral images. *Surg Today*, **36**, 1075-84.
- Attas, M., Hewko, M., Payette, J., Posthumus, T., Sowa, M. & Mantsch, H. (2001) Visualization of cutaneous hemoglobin oxygenation and skin hydration using near-infrared spectroscopic imaging. *Skin Res Technol*, **7**, 238-45.
- Bae, Y., Nelson, J. S. & Jung, B. (2008) Multimodal facial color imaging modality for objective analysis of skin lesions. *J Biomed Opt*, **13**, 064007.
- Bais, C. & Santomaso, B. (1998) G-protein-coupled receptor of Kaposi's sarcoma-associated herpesvirus is a viral oncogene and angiogenesis activator. *Nature* **391**, 86-89.
- Begelman, G., Zibulevsky, M., Rivlin, E. & Kolatt, T. (2009) Blind decomposition of transmission light microscopic hyperspectral cube using sparse representation. *IEEE Transactions on Medical Imaging*, **28**, 1317-1324.
- Bonner, R. F., Nossal, R., Havlin, S. & Weiss, G. H. (1987) Model for photon migration in turbid biological media. *J. Opt. Soc. Am. A*, **4**, 423.

- Born, M. & Wolf, E. (1999) *Principles of Optics, 7th ed.*, Cambridge University Press, Cambridge.
- Boshoff, C. & Endo, Y. (1997) Angiogenic and HIV-inhibitory functions of KSHV-encoded chemokines. *Science* **278**, 290-4.
- Bracewell, R. N. (2000) *The Fourier transform and its applications, 3rd ed.*, McGraw-Hill, New York.
- Case, K. M. & Zweifel, P. F. (1967) *Linear Transport Theory*, Addison Wesley, Reading.
- Cheng, Y., Swamisai, R., Umbaugh, S. E., Moss, R. H., Stoecker, W. V., Teegala, S. & Srinivasan, S. K. (2008) Skin lesion classification using relative color features. *Skin Res Technol*, **14**, 53-64.
- Chernomordik, V., Nossal, R. & Gandjbakhche, A. H. (1996) Point spread functions of photons in time-resolved transillumination experiments using simple scaling arguments. *Med. Phys.*, **23**, 1857.
- Crowther, J. M., Sieg, A., Blenkiron, P., Marcott, C., Matts, P. J., Kaczvinsky, J. R. & Rawlings, A. V. (2008) Measuring the effects of topical moisturizers on changes in stratum corneum thickness, water gradients and hydration in vivo. *Br J Dermatol*, **159**, 567-77.
- Cuccia, D. J., Bevilacqua, F., Durkin, A. J., Ayers, F. R. & Tromberg, B. J. (2009) Quantitation and mapping of tissue optical properties using modulated imaging. *J Biomed Opt*, **14**, 024012.
- Cuccia, D. J., Bevilacqua, F., Durkin, A. J. & Tromberg, B. J. (2005) Modulated imaging: quantitative analysis and tomography of turbid media in the spatial-frequency domain. *Opt Lett*, **30**, 1354-6.
- Dawson, J., Barker, D. (1980) A theoretical and experimental study of light absorption and scattering by in vivo skin. *Phys. Med. Biol.*, **25**, 695-709.
- de Haan, J. R., Wehrens, R., Bauerschmidt, S., Piek, E., van Schaik, R. C. & Buydens, L. M. C. (2007) Interpretation of ANOVA models for microarray data using PCA. *Bioinformatics*, **23**, 184-190.
- Demos, S., Radousky, H. & Alfano, R. (2000) Deep subsurface imaging in tissues using spectral and polarization filtering. *Opt Express*, **7**, 23-8.
- Demos, S. G. & Alfano, R. R. (1996) Temporal gating in highly scattering media by the degree of optical polarizatio. *Optics Letters*, **21**, 161-163.

- Demos, S. G. & Alfano, R. R. (1997a) Optical polarization imaging. *Applied Optics*, **36**, 150-155.
- Demos, S. G. & Alfano, R. R. (1997b) Optical polarization imaging. *Appl Opt*, **36**, 150-5.
- Douven, L. F. A. & Lucassen, G. W. (2000) Retrieval of optical properties of skin from measurement and modeling the diffuse reflectance. *Proc. SPIE* **3914**, 312–323.
- Drexler, W. & Fujimoto, J. G. (2008) Optical Coherence Tomography: Technology and Applications. *Springer*
- Du, Q. & Fowler, J. E. (2008) Low-complexity principal component analysis for hyperspectral image compression. *International Journal of High Performance Computing Applications* **22**, 438.
- Duderstadt, J. J. & Hamilton, L. J. (1976) *Nuclear Reactor Analysis*, Wiley, New York.
- Ensoli, B. & Barillari, G. (1992) Cytokines and growth factors in the pathogenesis of AIDS-associated Kaposi's sarcoma. *Immunol Rev*, **127**, 147-55.
- Fadzil, M. H., Norashikin, S., Suraiya, H. H. & Nugroho, H. (2009) Independent component analysis for assessing therapeutic response in vitiligo skin disorder. *J Med Eng Technol*, **33**, 101-9.
- Fantini, S., Walker, S. A., Franceschini, M. A., Kaschke, M., Schlag, P. M. & Moesta, K. T. (1998) Assessment of the size, position, and optical properties of breast tumors in vivo by noninvasive optical methods. *Applied Optics*, **37**, 1982.
- Fercher, A. F., Drexler, W., Hitzenberger, C. K. & Lasser, T. (2003a) Optical coherence tomography-principles and applications. *Rep. Prog. Phys.* , **66** 239-303.
- Fercher, A. F., Drexler, W., Hitzenberger, C. K. & Lasser, T. (2003b) Optical coherence tomography - Principles and applications. *Reports on Progress in Physics*, **66**, 239-303.
- Fercher, A. F., Hitzenberger, C. K., Drexler, W., Kamp, G. & Sattmann, H. (1993) In-vivo optical coherence tomography. *Am. J. Ophthalmol.* , **116**, 113-115
- Fercher, A. F., Hitzenberger, C. K., Kamp, G. & El-Zaiat, S. Y. (1995a) Measurement of intraocular distances by backscattering spectral interferometry. *Opt. Commun.* , **117**, 43-48.
- Fercher, A. F., Hitzenberger, C. K., Kamp, G. & El-Zaiat, S. Y. (1995b) Measurement of intraocular distances by backscattering spectral interferometry *Optics Communications*, **117**, 43-48.

- Ferraz, A., Esposito, E., Bruns, R. E. & DurÃ¡n, N. (1998) The use of principal component analysis (PCA) for pattern recognition in Eucalyptus grandis wood biodegradation experiments. *World Journal of Microbiology and Biotechnology*, **14**, 487-490.
- Gandjbakhche, A. H., Nossal, R. & Bonner, R. F. (1993a) Scaling relationships for theories of anisotropic random walks applied to tissue optics. *Applied Optics*, **32**, 504.
- Gandjbakhche, A. H. & Weiss, G. H. (1995a) Random walk and diffusion-like models of photon migration in turbid media. *Progress in Optics*, **XXXIV**, 335-402.
- Gandjbakhche, A. H. & Weiss, G. H. (1995b) Random walk and diffusion-like models of photon migration in turbid media. *Progress in Optics, ed. Wolf, E. Elsevier Science B.V.*, **XXXIV**, 333.
- Gandjbakhche, A. H., Weiss, G. H., Bonner, R. F. & Nossal, R. (1993b) Photon path-length distributions for transmission through optically turbid slabs. *Phys. Rev. E*, **48**, 810.
- Gioux, S., Mazhar, A., Cuccia, D. J., Durkin, A. J., Tromberg, B. J. & Frangioni, J. V. (2009) Three-dimensional surface profile intensity correction for spatially modulated imaging. *J Biomed Opt*, **14**, 034045.
- Goldman, L. (2007) Principles of CT and CT Technology. *Journal of Nuclear Medicine Technology*, **35**, 115-128.
- Gotzinger, E., Pircher, M., Leitgeb, R. & Hitzenberger, C. (2005) High speed full range complex spectral domain optical coherence tomography. *Opt.Express*, **13**, 583-594.
- Hance, G., Umbaugh, S. E., Moss, R. H. & Stoecker, W. V. (1996) Unsupervised Color Image Segmentation. *IEEE Eng in Medicine and Biology*, **96**.
- Häusler, G. & Lindner, M. W. (1998) Coherence radar and spectral radar - new tools for dermatological diagnosis, . *J. Biomed. Opt.* , **3**, 21-31.
- Horecker, B. L. (1943 ) The absorption spectra of hemoglobin and its derivatives in the visible and near infra-red regions. *J Biol Chem* **148**, 183.
- Huang, D., Swanson, E. A., Lin, C. P., Schuman, J. S., Stinson, W. G., Chang, W., Hee, M. R., Flotte, T., Gregory, K. & Puliafito, C. A. (1991a) Optical coherence tomography. *Science*, **254**, 1178-1181.

- Huang, D., Swanson, E. A., Lin, C. P., Schuman, J. S., Stinson, W. G., Chang, W., Hee, M. R., Flotte, T., Gregory, K., Puliafito, C. A. & et al. (1991b) Optical coherence tomography. *Science*, **254**, 1178-81.
- Ishimaru, A. (1978) *Wave propagation and scattering in random media*, Academic Press, New York.
- Jacques, S. L. (1998) Skin Optics. *Oregon Medical Laser Center News*, <<http://omlc.ogi.edu/news/jan98/skinoptics.html>>.
- Jacques, S. L. (2001) Optical Properties Spectra. *Oregon Medical Laser Center News*, <<http://omlc.ogi.edu/spectra/>>.
- Jacques, S. L., Ramella-Roman, J. C. & Lee, K. (2002) Imaging skin pathology with polarized light. *J Biomed Opt*, **7**, 329-40.
- Jacques, S. L., Roman, J. R. & Lee, K. (2000) Imaging superficial tissues with polarized light. *Lasers Surg Med*, **26**, 119-29.
- Jobsis, F. F. (1977a) Non-invasive, infra-red monitoring of cerebral O<sub>2</sub> sufficiency, bloodvolume, HbO<sub>2</sub>-Hb shifts and bloodflow. *Acta Neurol.Scand.Suppl*, **64**, 452-453.
- Jobsis, F. F. (1977b) Noninvasive, infrared monitoring of cerebral and myocardial oxygen sufficiency and circulatory parameters. *Science*, **198**, 1264-1267.
- Kainerstorfer, J., Amyot, F., Demos, S. G., Hassan, M., Chernomordik, V., Hitzenberger, C. K., Gandjbakhche, A. H. & Riley, J. D. (2009a) Quantitative assessment of ischemia and reactive hyperemia of the dermal layers using multi - Spectral imaging on the human arm. *Progress in Biomedical Optics and Imaging - Proceedings of SPIE*, **7369**.
- Kainerstorfer, J., Amyot, F., M. Ehler, M. Hassan, S. G. Demos, V. Chernomordik, C. K. Hitzenberger, Gandjbakhche, A. H. & J. D. Riley (2010a) Direct Curvature Correction for Non-Contact Imaging Modalities – Applied to Multi-Spectral Imaging. *J Biomed Opt*, **15**.
- Kainerstorfer J. M., F. Amyot, M. Hassan, M. Ehler, R. Yarchoan, K. M. Wyvill, T. Uldrick, V. Chernomordik, C. K. Hitzenberger, A. H. Gandjbakhche & Riley, J. D. (2010) Reconstruction-Free Imaging of Kaposi's Sarcoma Using Multi-Spectral Data. *Biomedical Optics, OSA Technical Digest*, BME6.
- Kainerstorfer, J. M., Amyot, F., Demos, S. G., Hassan, M., Chernomordik, V., Hitzenberger, C. K., Gandjbakhche, A. H. & Riley, J. D. (2009b) In *Progress in Biomedical Optics and Imaging - Proceedings of SPIE*, Vol. 7369.

- Kainerstorfer, J. M., Amyot, F., Demos, S. G., Hassan, M., Chernomordik, V., Hitzenberger, C. K., Gandjbakhche, A. H. & Riley, J. D. (2009c) Quantitative assessment of ischemia and reactive hyperemia of the dermal layers using multi - Spectral imaging on the human arm. *Progress in Biomedical Optics and Imaging - Proceedings of SPIE*, **7369**.
- Kainerstorfer, J. M., Amyot, F., Ehler, M., Hassan, M., Demos, S. G., Chernomordik, V., Hitzenberger, C. K., Gandjbakhche, A. H. & Riley, J. D. (2010b) Direct Curvature Correction for Non-Contact Imaging Modalities – Applied to Multi-Spectral Imaging. *Journal of Biomedical Optics*, **15**, 046013.
- Kainerstorfer, J. M., Ehler, M., Amyot, F., Hassan, M., Demos, S. G., Chernomordik, V., Hitzenberger, C. K., Gandjbakhche, A. H. & Riley, J. D. (2010c) Principal Component Model of Multi Spectral Data for Near Real Time Skin Chromophore Mapping. *Journal of Biomedical Optics*, **15**, 046007.
- Kainerstorfer, J. M., Riley, J. D., Ehler, M., Najafizadeh, L., Amyot, F., Hassan, M., Pursley, R., Demos, S. G., Chernomordik, V., Pircher, M., Hitzenberger, C. K. & Gandjbakhche, A. H. *submitted a manuscript called "Quantitative principal component model of multi spectral data for skin chromophore mapping using spatial priors"*.
- Kirillin, M. Y., Priezzhev, A. V. & Myllyla, R. (2007) In *Progress in Biomedical Optics and Imaging - Proceedings of SPIE*, Vol. 6627.
- Kovar, J. L., Simpson, M. A., Schutz-Geschwender, A. & Olive, D. M. (2007) A systematic approach to the development of fluorescent contrast agents for optical imaging of mouse cancer models. *Anal Biochem*, **367**, 1-12.
- Leitgeb, R. A., Hitzenberger, C. K. & Fercher, A. F. (2003) Performance of Fourier domain vs. time domain optical coherence tomography. *Opt. Express* **11**, 889-894
- Mandelkow, H., Brandeis, D. & Boesiger, P. (2010) Good practices in EEG-MRI: The utility of retrospective synchronization and PCA for the removal of MRI gradient artefacts. *NeuroImage*, **49**, 2287-2303.
- Mantis, G. & Zonios, G. (2009) Simple two-layer reflectance model for biological tissue applications. *Appl Opt*, **48**, 3490-6.
- Maris, M., Gratton, E., Maier, J., Mantulin, W. & Chance, B. (1994) Functional near-infrared imaging of deoxygenated haemoglobin during exercise of the finger extensor muscles using the frequency-domain techniques. *Bioimaging*, **2**, 174.

- Meglinski, I., Kirillin, M., Kuzmin, V. & Myllyla, R. (2008) Simulation of polarization-sensitive optical coherence tomography images by a Monte Carlo method. *Opt.Lett.*, **33**, 1581-1583.
- Meglinski, I. V. & Matcher, S. J. (2002) Quantitative assessment of skin layers absorption and skin reflectance spectra simulation in the visible and near-infrared spectral regions. *Physiol Meas*, **23**, 741-53.
- Merla A, D. D. L., Di Luzio S, Farina G, Pisarri S, Proietti M, Salsano F, Romani GL. (2002 ) Infrared functional imaging applied to Raynaud's phenomenon. *IEEE Eng Med Biol Mag.*, **21**, 73-9.
- Merschbrock, U., Hoffmann, J., Caspary, L., Huber, J., Schmickaly, U. & Lubbers, D. W. (1994) Fast wavelength scanning reflectance spectrophotometer for noninvasive determination of hemoglobin oxygenation in human skin. *Int J Microcirc Clin Exp*, **14**, 274-81.
- Miyamae, Y., Yamakawa, Y., Kawabata, M. & Ozaki, Y. (2008) A noninvasive method for assessing interior skin damage caused by chronological aging and photoaging based on near-infrared diffuse reflection spectroscopy. *Appl Spectrosc*, **62**, 677-81.
- Miyamoto, K., Takiwaki, H., Hillebrand, G. G. & Arase, S. (2002) Development of a digital imaging system for objective measurement of hyperpigmented spots on the face. *Skin Res Technol*, **8**, 227-35.
- Mogensen, M., Morsy, H. A., Thrane, L. & Jemec, G. B. (2008) Morphology and epidermal thickness of normal skin imaged by optical coherence tomography. *Dermatology*, **217**, 14-20.
- Moon, H. & Phillips, P. J. (2001) Computational and performance aspects of PCA-based face-recognition algorithms. *Perception*, **30**, 303-320.
- Nioka, S. R., Miwa, M., Orel, S., Schnall, M., Haida, M., Zhao, S. & Chance, B. (1994) Optical imaging of human breast cancer. *Adv. Exp. Med. Biol.*, **361**, 171.
- Nishimura, K., Abe, K., Ishikawa, S., Tsutsumi, S., Hirota, K., Aburatani, H. & Hirose, M. (2003) A PCA Based Method of Gene Expression Visual Analysis. *Genome Informatics* **14**, 346.
- Nuffer, L. L., Medvick, P. A., Foote, H. P. & Solinsky, J. C. (2006) Multispectral/hyperspectral image enhancement for biological cell analysis. *Cytometry A*, **69**, 897-903.

- Nugroho, H., Fadzil, M. H., Yap, V. V., Norashikin, S. & Suraiya, H. H. (2007) Determination of skin repigmentation progression. *Conf Proc IEEE Eng Med Biol Soc*, **2007**, 3442-5.
- Paquit, V., Price, J. R., Meïriaudeau, F., Tobin, K. W. & Ferrell, T. L. (2007) In *Progress in Biomedical Optics and Imaging - Proceedings of SPIE*, Vol. 6509.
- Paquit, V., Price, J. R., Seulin, R., Meïriaudeau, F., Farahi, R. H., Tobin, K. W. & Ferrell, T. L. (2006) In *Progress in Biomedical Optics and Imaging - Proceedings of SPIE*, Vol. 6141.
- Park, B. H., Pierce, M. C., Cense, B., Yun, S. H., Mujat, M., Tearney, G. J., Bouma, B. E. & de Boer, J. F. (2005) Real-time fiber-based multi-functional spectral-domain optical coherence tomography at 1.3 um. *Opt. Express*, **13**, 3931-3944.
- Pearson, K. (1901) On lines and planes of closest fit to systems of points in space. *Philosophical Magazine*, **2**.
- Pladellorens, J., Pinto, A., Segura, J., Cadevall, C., Anto, J., Pujol, J., Vilaseca, M. & Coll, J. (2008) A device for the color measurement and detection of spots on the skin. *Skin Res Technol*, **14**, 65-70.
- Prahl, S. (1998) Skin Optics. *Oregon Medical Laser Center News*, <http://omlc.ogi.edu/spectra/hemoglobin/index.html>.
- Reider, G. A. (1997) *Photonik - Eine Einführung in die Grundlagen, 1st ed.*, Springer, Wien, Wien.
- Riordan, B., Sprigle, S. & Linden, M. (2001) Testing the validity of erythema detection algorithms. *J Rehabil Res Dev*, **38**, 13-22.
- Roberts, W. E. (2009) Skin type classification systems old and new. *Dermatol Clin.*, **27(4)**, 529-33.
- Schmitt, J. M., Gandjbakhche, A. H. & Bonner, R. F. (1992) Use of polarized light to discriminate short-path photons in a multiply scattering medium *Applied Optics*, **31**.
- Sghaier-Hammami, B., Valledor, L., Drira, N. & Jorrin-Novo, J. V. (2009) Proteomic analysis of the development and germination of date palm [Phoenix dactylifera L.) zygotic embryos. *Proteomics*, **9**, 2543-2554.
- She, Z., Liu, Y. & Damatoa, A. (2007) Combination of features from skin pattern and ABCD analysis for lesion classification. *Skin Res Technol*, **13**, 25-33.
- Sinichkin, Y. P. & Uts, S. P. (1996) Spectroscopy of Human Skin in vivo: 1. Reflection Spectra. *Optics and Spectroscopy* **80(2)**, 228-234.

- Sodhi, A. & Montaner, S. (2000) The Kaposi's sarcoma-associated herpes virus G protein-coupled receptor up-regulates vascular endothelial growth factor expression and secretion through mitogen-activated protein kinase and p38 pathways acting on hypoxia-inducible factor 1alpha. *Cancer Res*, **60**, 4873-80.
- Sviridov, A., Chernomordik, V., Hassan, M., Russo, A., Eidsath, A., Smith, P. & Gandjbakhche, A. H. (2005a) Intensity profiles of linearly polarized light backscattered from skin and tissue-like phantoms. *J Biomed Opt*, **10**, 14012.
- Sviridov, A. P., Chernomordik, V., Hassan, M., Boccara, A. C., Russo, A., Smith, P. & Gandjbakhche, A. (2005b) Enhancement of hidden structures of early skin fibrosis using polarization degree patterns and Pearson correlation analysis. *J Biomed Opt*, **10**, 051706.
- Sviridov, A. P., Ulissi, Z., Chernomordik, V., Hassan, M. & Gandjbakhche, A. H. (2006) Visualization of biological texture using correlation coefficient images. *J Biomed Opt*, **11**, 060504.
- Swanson, E. A., Huang, D., Hee, M. R., Fujimoto, J. G., Lin, C. P. & Puliavito, C. A. (1992) High-speed optical coherence domain reflectometry. *Opt. Lett.* , **17**, 151-153.
- Targowski, P., Wojtkowski, M., Kowalczyk, A., Bajraszewski, T., Szkulmowski, M. & Gorczynska, I. (2004) Complex spectral OCT in human eye imaging in vivo. *Opt. Commun.*, **229**, 79-84.
- Tseng, S. H., Bargo, P., Durkin, A. & Kollias, N. (2009) Chromophore concentrations, absorption and scattering properties of human skin in-vivo. *Opt Express*, **17**, 14599-617.
- Tsumura, N., Haneishi, H. & Miyake, Y. (1999) Independent-component analysis of skin color image. *J Opt Soc Am A Opt Image Sci Vis*, **16**, 2169-76.
- Turk, M. & Pentland, A. (1991) Eigenfaces for recognition. *Journal of Cognitive Neuroscience*, **3**, 71-86.
- Umbaugh, S. E., Moss, R. H., Stoecker, W. V. & Hance, G. (1993) Automatic Color Segmentation Algorithms. *IEEE Eng in Med Bio*, **93**.
- van Veen, R. L. P., Sterenborg, H. J. C. M., Pifferi, A., Torricelli, A. & Cubeddu, R. (2004) Determination of VIS- NIR absorption coefficients of mammalian fat, with time- and spatially resolved diffuse reflectance and transmission spectroscopy *OSA Annual BIOMED Topical Meeting*.

- Vogel, A., Chernomordik, V. V., Riley, J. D., Hassan, M., Amyot, F., Dasgeb, B., Demos, S. G., Pursley, R., Little, R. F., Yarchoan, R., Tao, Y. & Gandjbakhche, A. H. (2007) Using noninvasive multispectral imaging to quantitatively assess tissue vasculature. *J Biomed Opt*, **12**, 051604.
- Vogel, A., Dasgeb, B., Hassan, M., Amyot, F., Chernomordik, V., Tao, Y., Demos, S. G., Wyvill, K., Aleman, K., Little, R., Yarchoan, R. & Gandjbakhche, A. H. (2006) Using quantitative imaging techniques to assess vascularity in AIDS-related Kaposi's sarcoma. *Conf Proc IEEE Eng Med Biol Soc*, **1**, 232-5.
- Wan, S., Anderson, R. R. & Parrish, J. A. (1981) Analytical modeling for the optical properties of the skin with in vitro and in vivo applications. *Photochem.Photobiol.*, **34**, 493-499.
- Westhauser, M., Bischoff, G., Borocz, Z., Kleinheinz, J., von Bally, G. & Dirksen, D. (2008) Optimizing color reproduction of a topometric measurement system for medical applications. *Med Eng Phys*, **30**, 1065-70.
- Whitton, J. T. & Everall, J. D. (1973) The thickness of the epidermis. *Br J Dermatol*, **89**, 467-76.
- Wojtkowski, M., Leitgeb, R., Kowalczyk, A., Bajraszewski, T. & Fercher, A. F. (2002) In vivo human retinal imaging by Fourier domain optical coherence tomography. *J Biomed.Opt.*, **7**, 457-463.
- Zagaynova, E. V., Shirmanova, M. V., Kirillin, M. Y., Khlebtsov, B. N., Orlova, A. G., Balalaeva, I. V., Sirotkina, M. A., Bugrova, M. L., Agrba, P. D. & Kamensky, V. A. (2008) Contrasting properties of gold nanoparticles for optical coherence tomography: phantom, in vivo studies and Monte Carlo simulation. *Phys Med Biol*, **53**, 4995-5009.
- Zakharov, P., Talary, M. S., Kolm, I. & Caduff, A. (2010) Full-field optical coherence tomography for the rapid estimation of epidermal thickness: study of patients with diabetes mellitus type 1. *Physiol Meas*, **31**, 193-205.
- Zakian, C., Pretty, I., Ellwood, R. & Hamlin, D. (2008) In vivo quantification of gingival inflammation using spectral imaging. *J Biomed Opt*, **13**, 054045.
- Zeman, H. D., Lovhoiden, G., Vrancken, C. & Danish, R. K. (2005) Prototype vein contrast enhancer. *Optical Engineering*, **44**.
- Zerbino (1994) Biopsy: its history, current and future outlook. *Lik Sprava.*, **3-4**.
- Zhang, R., Verkruysse, W., Choi, B., Viator, J. A., Jung, B., Svaasand, L. O., Aguilar, G. & Nelson, J. S. (2005) Determination of human skin optical properties from

spectrophotometric measurements based on optimization by genetic algorithms.  
*J Biomed.Opt.*, **10**, 024030.



# Acknowledgements

This thesis would not exist without the help and support of many people. I would like to express my deepest gratitude towards

- Amir Gandjbakhche for supervising this thesis and mentoring me throughout those years. Without him, this work would have not been possible. His know-how, open-mindedness, and motivation made this thesis possible. Also I would like to thank him for all the opportunities presented to me, the trust in my abilities, the pushiness, and support in general.
- Christoph Hitzenberger for his support throughout those years. None of this work would have been possible, without his support, even if it had to be from overseas. I am deeply grateful for his visits to NIH and his efforts and successes to make it possible to have a PhD advisor on a different continent.
- My colleagues at NIH: Moinuddin Hassan for treating me as a grown up scientist from day one on, for sharing the office with me and creating a comfortable atmosphere, for always smiling and thus calming me down even on the most difficult days, and for coffee invitations, never allowing me to pay. Victor Chernomordik for alternating the coffee invitations with Hassan, for his clear-mindedness and open door policy. I don't remember a single time when he would not have time for my questions and when I wouldn't get a clear and thorough answer in return. Franck Amyot for proof reading many first drafts, for his calmness in an at times hectic environment. Jason Riley for teaching me data analysis tools and first introducing me to rock climbing. Laleh Najafizadeh for her help and thoroughness on the polarization imaging project and her appreciation. Raci Say for dealing with all the administrative tasks, making everybody's life so much easier, and for never complaining about last minute tasks, but rather handling them with a smile.
- My collaborators: Jay Knutson and Alex Smirnov at NHLBI for their support and help in building the OCT system and for their open door policy. A day spent in Jay's lab meant lots of great conversations, learning about new tools and toys, and lots of chocolate. Robert Yarchoan at NCI for clinical

collaboration on Kaposi's Sarcoma imaging. Kathy Wyvill for scheduling the patients and help in general.

- My family. Without everybody's support, tolerance, and understanding I would have not been able to stay in the US for so long and still feel at home when visiting Vienna. My mother, for not only tolerating but appreciating long hours spent on Skype, and for her endless support and advice. My father, for all his support and for being proud of my brother and me.
- My friends. Living in the US means seeing people come and go from this country and from my life. I was very fortunate to meet many great people, who in one way or the other, had impact on my life, which I am very grateful for. From all those people, two have to be acknowledged here by name: Steffi, for long evenings spent working or talking, for endless support, for listening, and for so much more. Luis, for mate, tolerance, proof reading, teaching, listening and for so many more things, way too many to be written down here and most importantly for understanding.
- All the volunteers and patients. Without their willingness to participate in the research studies, no clinical work could have been conducted. I hope that my work will be beneficial for the well being of future patients.
- The research for this thesis was funded by the Intramural Research Program of the *Eunice Kennedy Shriver* National Institute of Child Health and Human Development at the National Institutes of Health.

# Curriculum vitae

## Personal Data:

Name Jana M. Kainerstorfer  
Date of Birth October 30<sup>th</sup>, 1983  
Place of Birth Vienna, Austria  
Address Section on Analytical and Functional Biophotonics  
Program on Pediatric Imaging and Tissue Sciences  
*Eunice Kennedy Shriver* National Institute of Child Health and  
Human Development  
National Institutes of Health  
Bldg. 9, Rm. B1E11  
Bethesda, MD, 20892  
Phone +1 301 594 0352  
Email [kainersj@mail.nih.gov](mailto:kainersj@mail.nih.gov)

## Education:

11/2007 – present Predoctoral Visiting Fellow – National Institutes of Health,  
Bethesda, MD, USA  
PhD advisor at NIH:  
Amir Gandjbakhche, PhD (NIH/NICHD/PPITS/SAFB)  
08/2007 – present Doctoral program in Physics – University of Vienna, Austria  
PhD advisor in Vienna:  
Christoph Hitzenberger, PhD (Medical University of Vienna)  
07/2007 M.S. in Physics – University of Vienna, Austria  
Title: “Probing the “fast signal” in Near Infrared Spectroscopy  
(NIRS)”  
07/2006 – 05/2007 Master’s thesis research – Center for Functional and Molecular  
Imaging (CFMI), Georgetown University, Washington DC,  
USA  
07/2006 2<sup>nd</sup> diploma exam  
08/2005 – 12/2005 Exchange student at Georgetown University, Washington DC,  
USA  
10/2002 – 07/2007 Master’s program in Physics at the University of Vienna,  
Austria

## **Work Experience:**

11/2007 – present	Predocctoral Visiting Fellow at NIH/NICHD/PPITS/SAFB
07/2006 – 05/2007	Research Assistant. Center for Functional and Molecular Imaging (CFMI) at Georgetown University, Washington, DC.
05/2003 – 06/2006	Librarian assistant. Austrian Central Library of Physics.
01/2003 – 12/2005	Research Assistant. General Hospital of Vienna / Austria.
10/2004	Tutor, University of Vienna / Department of Physics
10/2003	Tutor, University of Vienna / Department of Physics
12/2002 – 12/2003	Research Assistant. Hospital “Goldenes Kreuz”, Vienna, Austria.

## **Scholarships / Fellowships / Awards:**

07/2010	FARE 2011 competition, NIH
04/2010	Image Competition – 6 <sup>th</sup> NICHD Fellow Retreat
08/2009	FARE 2010 competition, NIH
11/2006	Research fellowship for the Master’s thesis research in the US through the University of Vienna
07/2006	“Kurzfristiges Wissenschaftliches Arbeiten im Ausland” (KWA) – Research fellowship / University of Vienna
08/2005	Scholarship through the Joint Study Program of the University of Vienna (exchange program with Georgetown University)

## **Presentations and Invited Talks:**

- 7<sup>th</sup> ICMRM, 2003 (co-author)
- OHBM (Organization for Human Brain Mapping), 2007 (2 x co-author), 2009 (co-author), 2010 (co-author)
- CNS (Cognitive Neuroscience Society) Annual Meeting, 2007 (2 x co-author)
- SfN (Society for Neuroscience) Annual Meeting, 2007 (co-author), 2008 (co-author), 2009 (co-author), 2010 (author – oral)
- SPIE – Photonics West, 2008 (author – poster), 2010 (author – oral)
- Metropolitan Biophotonics Symposium, 2009 (author – oral), 2010 (author – oral)

- ECBO (European Conferences on Biomedical Optics), 2009 (author – oral)
- Program in Physical Biology, NICHD (Program Seminar), 2009 (author – oral)
- OSA (Optical Society of America) BIOMED, 2010 (author – oral)
- 6<sup>th</sup> NICHD Fellow Retreat, 2010 (author – oral and poster)
- Gordon Research Conference, Lasers in Medicine and Biology, 2010 (author – poster)
- Optics Within Life Sciences, Quebec City, 2010 (author – oral)

### **Society Memberships:**

- SFN (Society for Neuroscience) – Student Member

### **Scientific Responsibilities and Activities:**

- Part-time reviewer: Journal of Biomedical Optics
- Part-time reviewer: Journal of Biophotonics
- Workshop Technical Coordinator – The Inter-Institute Workshop on Optical Diagnostic and Biophotonic Methods from Bench to Bedside, NIH (2009)

### **Book chapters:**

- Hassan M, **Kainerstorfer J.**, Chernomordik V., Vogel A., Gannot I., Yarchoan R. and Gandjbakhche A. “Non-invasive Infrared imaging for functional monitoring of disease processes”, Medical Devices and System, the Biomedical Engineering Handbook, fourth edition, Edited by Nicholas Diakides and Joseph Bronzino. 2011. CRC press, Florida, USA.

### **Publications:**

- Master’s thesis, “Probing the “fast signal” in Near Infrared Spectroscopy (NIRS)”. **Jana M. Kainerstorfer**, (2007). Vienna, Austria
- Andrei V. Medvedev, **Jana M. Kainerstorfer**, Sergey V. Borisov, Randall L. Barbour, John VanMeter, “Event-related fast optical signal in a rapid object recognition task: improving detection by the Independent Component Analysis”, Brain Research, 1236:145-58, (2008)
- **Jana M. Kainerstorfer**, Franck Amyot, Stavros G. Demos, Moinuddin Hassan, Victor Chernomordik, Christoph K. Hitzenberger, Amir H. Gandjbakhche, Jason D. Riley, ‘Quantitative assessment of ischemia and reactive hyperemia of the dermal layers using multi - spectral imaging on the human arm’, Proceedings of the SPIE, Volume 7369, pp. 73690P-73690P-10 (2009).
- Andrei.V. Medvedev, **Jana M. Kainerstorfer**, Sergey V. Borisov and John VanMeter, ”Fast optical signal in the prefrontal cortex correlates with EEG”, Proceedings IFMBE, (2010)

- Andrei V. Medvedev, **Jana M. Kainerstorfer**, Sergey V. Borisov, Amir H. Gandjbakhche, John VanMeter, ““Seeing” EEG through the skull: imaging prefrontal cortex with fast optical signal”, *Journal of Biomedical Optics*, in press (2010)
- Andrei V. Medvedev, **Jana M. Kainerstorfer**, Sergey V. Borisov, John VanMeter, ”Functional connectivity in the prefrontal cortex measured by near-infrared spectroscopy during ultra-rapid object recognition”, *Journal of Biomedical Optics*, under review, (2010)
- **Jana M. Kainerstorfer**, Franck Amyot, Moinuddin Hassan, Martin Ehler, Robert Yarchoan, Kathleen M. Wyvill, Thomas Uldrick, Victor Chernomordik, Christoph K. Hitzenberger, Amir H. Gandjbakhche, and Jason D. Riley, “Reconstruction-Free Imaging of Kaposi’s Sarcoma Using Multi-Spectral Data”, *Proceedings of OSA*, (2010)
- **Jana M. Kainerstorfer**, Franck Amyot, Martin Ehler, Moinuddin Hassan, Stavros G. Demos, Victor Chernomordik, Christoph K. Hitzenberger, Amir H. Gandjbakhche and Jason D. Riley, “Direct Curvature Correction for Non-Contact Imaging Modalities – Applied to Multi-Spectral Imaging”, *Journal of Biomedical Optics*, 15(4), 046013 (2010)
- **Jana M. Kainerstorfer**, Martin Ehler, Franck Amyot, Moinuddin Hassan, Stavros G. Demos, Victor Chernomordik, Christoph K. Hitzenberger, Amir H. Gandjbakhche and Jason D. Riley, “Principal Component Model of Multi Spectral Data for Near Real Time Skin Chromophore Mapping”, *Journal of Biomedical Optics*, 15(4), 046007 (2010)
- **Jana M. Kainerstorfer**, Jason D. Riley, Martin Ehler, Laleh Najafizadeh, Franck Amyot, Moinuddin Hassan, Randall Pursley, Stavros G. Demos, Victor Chernomordik, Michael Pircher, Christoph K. Hitzenberger, and Amir H. Gandjbakhche, “Quantitative principal component model for skin chromophore mapping using multi spectral images and spatial priors”, *Biomedical Optics Express*, (under review)
- **Jana M. Kainerstorfer**, Jason D. Riley, Martin Ehler, Laleh Najafizadeh, Franck Amyot, Moinuddin Hassan, Randall Pursley, Stavros G. Demos, Victor Chernomordik, Michael Pircher, Christoph K. Hitzenberger, and Amir H. Gandjbakhche, “In vivo validation of principal component models with spatial priors for quantification of multi spectral images”, *Biomedical Optics Express*, (under review)